RODRIGO ALCARAZ DE LA OSA

NANOSTRUCTURED SYSTEMS WITH ARBITRARY ELECTRIC AND MAGNETIC PROPERTIES: DEVELOPMENT AND APPLICATION OF AN EXTENSION OF THE DISCRETE DIPOLE APPROXIMATION (E-DDA)

NANOSTRUCTURED SYSTEMS WITH ARBITRARY ELECTRIC AND MAGNETIC PROPERTIES: DEVELOPMENT AND APPLICATION OF AN EXTENSION OF THE DISCRETE DIPOLE APPROXIMATION (E-DDA)

RODRIGO ALCARAZ DE LA OSA

Departamento de Física Aplicada
Facultad de Ciencias
Universidad de Cantabria

Santander, Abril 2013

Rodrigo Alcaraz de la Osa: *Nanostructured systems with arbitrary electric and magnetic properties: Development and Application of an Extension of the Discrete Dipole Approximation (E-DDA)* © April 2013

SUPERVISORS:
Dr. José María Saiz Vega
Prof. Fernando Moreno Gracia

LOCATION:
Santander

Nothing ventured, nothing gained!
— Ancient proverb

Dedicated to my wonderful, loving wife, Jésica.

ABSTRACT

The discrete dipole approximation (DDA) has been successfully applied to many light scattering problems. Simply stated, the DDA is an approximation of the continuum target by a finite array of polarizable points. The points acquire dipole moments in response to the local fields. The dipoles of course interact with one another via their electric and magnetic fields, so the DDA is also sometimes referred to as the coupled dipole approximation. As of today, the method has established itself as one of the best solutions to calculate the scattering of radiation by particles of arbitrary shape. Hitherto, however, the main existing implementations include materials with relative magnetic permeability equal to 1 only, which is correct for all materials in the optical frequency range.

Nonetheless, materials with unusual optical properties have arisen recently. This includes the possibility of having both electric and magnetic anisotropic properties (bianisotropic materials) in the most general case. The situation where both the real part of the electric permittivity and the magnetic permeability are negative corresponds to what is known as "left-handed materials", or negative index materials (NIM), with unconventional properties such as negative refraction. The treatment of these materials with a method as contrasted as the DDA provides several advantages, apart from possibly being the only method available in many cases.

This PhD Thesis has explored nanostructured systems with arbitrary anisotropic optical properties (both electric and magnetic) by means of an Extension of the Discrete Dipole Approximation (E-DDA). During the development of this dissertation, a computational code (E-DDA code) has been implemented, able to produce comparative results with existing DDA codes, obtaining an excellent agreement. After validation, the method was then applied to a wide range of materials and situations, making a special reference to its application to magneto-optical materials (with an antisymmetric electric permittivity tensor) and composite materials.

As a summary, the status of the E-DDA code is mature enough to be applied to very different configurations, making it a very useful, flexible and stable computational tool for calculating scattering and absorption of light by irregular particles, including anisotropic materials both electrically and magnetically at the same time in the most general case.

RESUMEN

La aproximación de dipolo discreto (o DDA por sus iniciales en inglés) ha sido empleada con éxito en multitud de aplicaciones dentro del ámbito de la difusión de luz. Básicamente consiste en discretizar el blanco difusor en elementos polarizables. Los elementos adquieren momentos dipolares en respuesta a los campos locales. Los dipolos por supuesto interaccionan entre ellos por medio de sus campos eléctricos y magnéticos, por eso a la DDA también se la conoce como aproximación de dipolo acoplado.

A día de hoy, el método se afianza como una de las mejores soluciones para calcular la radiación difundida por partículas de forma arbitraria. Hasta ahora, sin embargo, las principales implementaciones existentes sólo incluyen materiales en los que la permeabilidad magnética relativa puede aproximarse por la unidad, lo cual es acertado para todos los materiales en el dominio de las frecuencias del rango óptico.

No obstante, últimamente están apareciendo materiales con propiedades ópticas inusuales, como por ejemplo el caso de que algunas de sus constantes ópticas efectivas sean negativas (sus partes reales), o bien que presenten anisotropía tanto para el campo eléctrico como para el magnético (materiales bianisótropos). El caso doble negativo correspondería a lo que se ha venido en llamar “materiales zurdos”, o materiales con índice negativo, con propiedades sorprendentes como la refracción negativa. El tratamiento de estos materiales con un método tan bien contrastado como es el DDA presenta bastantes ventajas, aparte de que en muchos casos puede ser el único método disponible.

Esta Tesis Doctoral ha explorado sistemas nanoestructurados con propiedades eléctricas y magnéticas anisótropas por medio de una Extensión de la Aproximación de Dipolo Discreto (E-DDA). Durante el desarrollo de esta tesis, se ha implementado un código computacional (código E-DDA), capaz de producir resultados comparativos con otros códigos DDA existentes, obteniendo un acuerdo excelente. Después de validarse, el método se ha aplicado a un amplio rango de materiales y situaciones, haciendo mención especial a su aplicación a materiales magneto-ópticos (con un tensor de permisividad eléctrica antisimétrico) y materiales compuestos.

En resumen, el estado del código desarrollado es suficientemente maduro como para poder aplicarse a muchas configuraciones diferentes, haciendo de él una herramienta computacional útil, flexible y estable para calcular la difusión y absorción de luz por partículas irregulares, incluyendo materiales anisótropos tanto eléctricos como magnéticos en el caso más general.

PUBLICATIONS

Some ideas and figures have appeared previously in the following publications:

ARTICLES

- R. Alcaraz de la Osa, P. Albella, J. M. Saiz, F. González, and F. Moreno, "Extended discrete dipole approximation and its application to bianisotropic media," *Opt. Express* **18**, 23, 23865-23871 (2010).
- B. García-Cámara, R. Alcaraz de la Osa, J. M. Saiz, F. González, and F. Moreno, "Directionality in scattering by nanoparticles: Kerker's null-scattering conditions revisited," *Opt. Lett.* **36**, 5, 728-730 (2011).
- R. Alcaraz de la Osa, J. M. Saiz, F. Moreno, P. Vavassori, and A. Berger, "Transverse magneto-optical effects in nanoscale disks," *Phys. Rev. B* **85**, 064414 (2012).
- R. Alcaraz de la Osa, J. M. Sanz, J. M. Saiz, F. González, and F. Moreno, "Quantum optical response of metallic nanoparticles and dimers," *Opt. Lett.* **37**, 23, 5015-5017 (2012).
- R. Alcaraz de la Osa, F. Moreno, and J. M. Saiz, "A new approach for modeling composite materials," *Opt. Comm.* **291**, 405-411 (2013).

CONTRIBUTIONS TO CONFERENCES

- P. Albella, R. Alcaraz de la Osa, B. Setién, J. M. Saiz, F. González, and F. Moreno, "Inspección Nanométrica de Superficies: Influencia de la forma de la nanopartícula-sensor," Poster at IX RNO, Ourense (Spain), September 2009.
- R. Alcaraz de la Osa, J. M. Saiz, F. González, P. Albella, and F. Moreno, "An analysis of magnetic materials through an extension of the discrete dipole approximation," Awarded Poster at CEN2010, Segovia (Spain), June 2010.
- J. M. Sanz, P. Albella, J. M. Saiz, R. Alcaraz de la Osa, F. Moreno, and F. González, "Polar Decomposition of the Mueller Matrix applied to nanoparticle sizing," Poster at PIERS 2011, Marrakech (Morocco), March 2011.

- P. Albella, R. Alcaraz de la Osa F. González, J. M. Saiz, and F. Moreno, "Metal nanoshells characterization by means of the linear polarization degree at right angle scattering configuration," Talk at PIERS 2011, Marrakech (Morocco), March 2011.

- R. Alcaraz de la Osa, J. M. Saiz, F. Moreno, P. Vavassori, and A. Berger, "Optical and magneto-optical response of magnetic nano-scale disks: size effects," Poster at PPM 2011, Bilbao (Spain), April 2011.

- B. García-Cámara, R. Alcaraz de la Osa, J. M. Saiz, F. González, and F. Moreno, "Las condiciones de scattering nulo y el Teorema Óptico: revisión de las condiciones de Kerker," Talk at XXXIII Bienal de la RSEF, Santander (Spain), September 2011.

- R. Alcaraz de la Osa, J. M. Saiz, F. Moreno, P. Vavassori, and A. Berger, "Magneto-optical effects in nano-disks as a perturbation of the optical response," Talk at NanoSpain Conf. 2012, Santander (Spain), February 2012.

- R. Alcaraz de la Osa, J. M. Saiz, F. González, and F. Moreno, "On the optical properties of random composite materials," Poster at Nanolight 2012, Benasque (Spain), March 2012.

- J. M. Sanz, D. Ortiz, J. M. Saiz, P. Albella, R. Alcaraz de la Osa, F. González, F. Moreno, H. O. Everitt, A. S. Brown, T.- H. Kim, and Y. Yang, "Ellipsometry for Nanoplasmonics in the UV Range," Poster at NFO 2012, San Sebastián (Spain), September 2012.

- R. Alcaraz de la Osa, J. M. Saiz, F. González, and F. Moreno, "Modeling of nanostructured inhomogeneous materials," Poster at NFO 2012, San Sebastián (Spain), September 2012.

- R. Alcaraz de la Osa, J. M. Saiz, F. González, and F. Moreno, "Modelado de materiales heterogéneos nanoestructurados," Talk at X RNO, Zaragoza (Spain), September 2012.

- D. Ortiz, J. M. Sanz, R. Alcaraz de la Osa, J. M. Saiz, F. González, and F. Moreno, "A study of the Near-Field of metallic materials for Plasmonics in the UV," Talk at CEN2012, Carmona-Sevilla (Spain), October 2012.

- R. Alcaraz De La Osa, J. M. Sanz, J. M. Saiz, F. González, and F. Moreno, "Quantum effects in small plasmonic particles," Invited Talk at META'13, Sharjah (UAE), March 2013.

Knowledge is in the end based on acknowledgement.

— Ludwig Wittgenstein

ACKNOWLEDGMENTS/AGRADECIMIENTOS

El viaje que ha supuesto esta tesis doctoral está llegando a su fin. A lo largo del camino he tenido la suerte de contar con muchas personas que me han apoyado y ayudado en tantos momentos difíciles. Es imposible plasmar aquí mi gratitud hacia todos los que han compartido conmigo este viaje, colaborando y participando en su éxito.

Existe una persona que ha sabido animarme en todos y cada uno de los duros momentos que inevitablemente han surgido durante estos 4 años. Ella ha sabido alentarme y evitar que tirara la toalla ("you are the wind at my back"). Me siento afortunado por tenerte junto a mí. Es por eso que mi primer agradecimiento es hacia ti, Jésica, gracias de todo corazón por estar siempre ahí, a mi lado.

Quisiera agradecer a Chema y Fernando, mis supervisores y padres científicos, toda su labor de formación y apoyo durante estos años. Desde el principio me acogieron con una sonrisa y no dudaron en compartir todo su conocimiento y experiencia conmigo. Gracias Chema y Fernando por abrirme las puertas de la investigación y guiarme por este camino a menudo espinoso. Nunca os olvidaré. Una mención especial para Paco, quien ha estado siempre ahí, dispuesto a darme un empujón cada vez que lo necesitaba. Gracias Paco por ser como eres, y darme la oportunidad de acercarme a ti y aprender a tu lado.

Mi agradecimiento también a todo el Grupo de Óptica, especialmente a Pablo y Juanma, por todos los momentos que hemos pasado juntos y las fructíferas discusiones que hemos tenido.

Quisiera dar las gracias a todas las personas con las que he colaborado en este tiempo, especialmente a Juanjo, Paolo y Andreas, por abrirme las puertas de sus grupos de investigación y acogerme como a uno más. Gracias por darme esa oportunidad.

Una mención especial para José Manuel, quien ha estado siempre dispuesto a ayudarme con cualquier problema no científico con el que me encontrara. Gracias José Manuel.

No quisiera marcharme sin dejar constancia de mi agradecimiento a toda mi familia, especialmente a mis padres, José y Lourdes, y a mi hermana, Ángela. Forman parte de mi vida y sin ellos no estaría escribiendo esto. Gracias familia. Cora, sé que nunca leerás esto ni serás consciente de lo mucho que me has apoyado, pero quisiera darte las gracias por todos los momentos que hemos pasado juntos. Nunca te olvidaré.

CONTENTS

LIST OF FIGURES

LIST OF TABLES

1

INTRODUCTION

1.1 HISTORICAL RECORD

Scientists have tried to elucidate the nature of light and its interaction with matter since the beginning of time. From the Greek philosophers as Euclides (300 BC) with its geometrical optics treatises to the modern theories of quantum optics, with the explanation of the photoelectric effect proposed by Einstein [1], many aspects of light have been progressively explained. It is not until the 16th and 17th centuries when systematic studies about what is called today classical optics phenomena were made by Galileo Galilei (1564-1642), Johanness Kepler (1571-1630) or René Descartes (1596-1650). Willebrord Snel van Royen (1580-1626), also known as Snellius, proposed the refraction law, later derived by Descartes. In the 17th century, while Isaac Newton (1642-1727) proposed a corpuscular theory of light, Christian Huygens (1629-1695) was the first who wrote of light as a wave, and it was not until the 19th century, with the experiments by Thomas Young (1773-1829), when the wave theory of light was widely accepted. James Clerk Maxwell (1831-1879) worked deeply in a theory that explained several electric and magnetic phenomena, that concluded in the Maxwell equations [2, 3] and the wave equation obtained from them, used since then to describe electromagnetic radiations of any frequency. These equations are the basis of the electromagnetism and merge the works done by Faraday (1791-1867), Gauss (1777-1855) and Ampère (1775-1863).

Maxwell's works seemed enough to explain light phenomena. However, the debate was reopened in the 20th century. A new quantum theory of light was derived from the works done by Max Planck (1858-1947) and Albert Einstein (1879-1955) and the concept of the photon started to appear. Every progress made in the study of light has brought about a group of new applications and developments. This happened with light scattering, the field in which the present work must be framed. This physical phenomenon, which affects not only light, but also sound waves and moving particles for example, leads to a deviation of the incoming energy due to the presence of a localized inhomogeneity in the medium through which it propagates. Light scattering is quite common and it is responsible of, for instance, the blue color of the sky, explained by Rayleigh [4] in 1899.

1.2 MOTIVATION

In his 1959 lecture at Caltech, Feynman [5] envisaged the potential of the ability to manipulate matter at the atomic scale. It is generally accepted that Feynman's visionary discussion of the problems and promise of miniaturization constituted the starting point for the new field that today is called *nanotechnology*. Generally speaking, nanotechnology works with materials, devices, and other structures with at least one dimension sized from 1 to 100 nanometres. Quantum mechanical effects are often important at this quantum-realm scale. In Feynman's words, "Atoms on a small scale behave like *nothing* on a large scale, for they satisfy the laws of quantum mechanics" [5]. Nanotechnology has made it possible to realize some of Feynman's dreams, such as building motors on a molecular scale, realized in 2003 [6].

Nanophotonics or Nano-optics is the study of the behavior of light on the nanometer scale. The interaction between light and metal nanoparticles (NPs), in particular, is dominated by localized surface plasmon resonances (LSPRs), or charge-density oscillations on the closed surfaces of the particles [7, 8]. LSPRs have the ability to strongly scatter and absorb light and to squeeze light into nanometer dimensions, producing large local enhancements of electromagnetic fields [9]. The science and technology that deals with the generation, control, manipulation, and transmission of these excitations in metal nanostructures has recently grown into an independent research field known as "nanoplasmonics". The field of nanoplasmonics is young but rich in phenomena that have inspired practical uses in physics, biomedicine, environmental monitoring, and national security [10].

Nanoparticles are unique tools as sensors. First, they are larger than typical molecules yet smaller than viruses. They are similar in size to many proteins. This is part of the reason they can operate well inside cells. Second, nanosensors possess unique physical characteristics. They deliver sensitivity orders of magnitude better than conventional devices and provide such performance advantages as fast response and portability. For example, nanoshells [11] and nanorice [12] are made of a non-conducting core that is covered by a metallic shell. Nanoshells are about 10,000 times more effective at Surface-Enhanced Raman Scattering (SERS) than traditional systems. Nanoshells provide an opportunity to design all-optical nanoscale sensors - essentially new molecular-level diagnostic instruments - that could detect as little as a few molecules of a target substance [13].

Third, nanosensors allow for building integrated devices, providing an elemental base for intelligent sensors, characterized as having significant data storing-, processing-, and analyzing power. All this adds to the above mentioned LSPR and its related properties, which do not exist in the bulk materials. The concept of intelligent sensors, which is being presently developed, is an implementation of another of Feynman's visions. Among the most central and fundamental problems of biology in 1959, Feynman mentioned the question: "What is the sequence of bases in the DNA?" It took more than 40 years to find an answer to this question on the basis of many technological innovations: a draft human genome sequence was presented [14] as recently as in 2001. This sequence is an instance of "the biological example of writing information on a small scale" which inspired Feynman "to think of something that should be possible for technical applications. Biology is not simply writing information; it is *doing something* about it" [5].

Another example of how visionary Feynman's 1959 lecture was can be found in the following words, directly related with the metamaterials field: "What would the properties of materials be if we could really arrange the atoms the way we want them? ... I can't see exactly what would happen, but I can hardly doubt that when we have some *control* of the arrangement of things on a small scale we will get an enormously greater range of possible properties that substances can have, and of different things that we can do" [5].

1.3 OBJECTIVES AND THESIS OVERVIEW

The objective of the current dissertation is to explore nanostructured systems with arbitrary optical properties (both electric and magnetic) by means of an Extension of the Discrete Dipole Approximation (E-DDA code). The method has been applied to a wide range of materials including anisotropic materials both electrically and magnetically, at the same time in the most general case. In order to accomplish such an ambitious task, four objectives needed to be fulfilled:

1. Develop and implement a working preliminary code capable of treating dielectric materials based on the Discrete Dipole Approximation (DDA).
2. Extend the early version of the code to allow for a wider range of materials, including metals and absorbents.
3. Perform the definitive extension, enabling tensorial optical properties (considering both electric and magnetic point dipoles).
4. Develop studies and sufficient case-based reasoning so to allow validation of the results.

Throughout this dissertation we have adhered to the following outline:

- A part dedicated to the theoretical foundations on which this dissertation is based, divided in several chapters:

  - A theoretical introduction about the interaction of light with matter, emphasizing the importance of the interaction of electric and magnetic dipoles.
  - A short account of the optical properties of materials, including the well-known Clausius-Mossotti relation and effective medium theories.
  - A review of the available numerical methods in electromagnetics, including a thorough description of the code implementing the Extended Discrete Dipole Approximation (E-DDA).
- A part dedicated to the main results obtained within this doctoral dissertation, including.
  - An opening chapter devoted to the initial validation of the results obtained with the E-DDA code.
  - A chapter dedicated to the application of the E-DDA code to magneto-optical materials.
  - A study of composite materials, including metamaterials, emphasizing the versatility of the E-DDA implementation.
  - A placeholder chapter where some additional aspects are studied in detail, including a quantum model for the optical properties of very small plasmonic particles.
- In the final section, a summary of the main conclusions as well as some future perspectives are presented.

Part I

FOUNDATIONS

A description of the theoretical basis on which most of this Thesis is founded as well as a review of the available numerical methods in electromagnetics, including a thorough description of the code implementing the Extended Discrete Dipole Approximation (E-DDA).

2

LIGHT AND MATTER

The vision of the world around us is inevitably governed by a phenomenon known as *scattering*. Either quantitative or qualitative, by means of physical-mathematical models or with the help of our sensory impressions, to describe the light and its interaction with the matter around us needs the concept of scattering. Such a concept involves an spatial redistribution of the energy and the appearance of light in directions different from the emission of the light source, which are typically radial for area emitters, or lineal for directional emitters. This mechanism, we are so used to, together with the absorption, is the responsible of processes as varied as the different irisation of the clouds, the generation of the rainbow, the blue color of the sky, the orangish sunsets or the green of forest foliage.

Before analyzing the problem of scattering of light, it is necessary to describe the nature of light from an appropriate formalism, namely *electromagnetism*. This discipline provides a suitable physical and mathematical apparatus. That is why, in this chapter, we present a summary of the basic concepts and the equations connected to the resolution of the phenomenon of scattering of light.

Hereinafter, we adopt a macroscopic approach to the problem of determining absoprtion and scattering of electromagnetic waves by particles. Therefore, the logical point of departure is the Maxwell equations for the macroscopic electromagnetic field at interior points in matter, which in SI units may be written [8] (see also Appendix A):

$$\nabla \cdot \mathbf{D} = \rho \tag{2.1}$$

$$\nabla \times \mathbf{E} + \frac{\partial \mathbf{B}}{\partial t} = 0 \tag{2.2}$$

$$\nabla \cdot \mathbf{B} = 0 \tag{2.3}$$

$$\nabla \times \mathbf{H} - \frac{\partial \mathbf{D}}{\partial t} = \mathbf{J} \tag{2.4}$$

, where **E** is the electric field and **B** the magnetic induction. The charge density ρ and the current density **J** are associated with so-called "free" charges.

The electric displacement field **D** represents how the electric charge distribution of a given medium, including charge transport and/or dipole reorientation, is influenced by an electric field **E**. Both magnitudes are related through the expression:

$$\mathbf{D} = \bar{\bar{\varepsilon}}\mathbf{E} = \varepsilon_0 \mathbf{E} + \mathbf{P} \tag{2.5}$$

, where, in general, $\bar{\bar{\varepsilon}}$ will be a 2^{nd} order (or rank) complex tensor (therefore depending on the direction of the electric field), function of a variety of parameters such as the frequency, position, humidity, temperature, etc. **P** is the electric polarization (average electric dipole moment per unit volume) and ε_0 is the permittivity of free space. When an electric field is applied to a medium, an electric current may appear. The total current flowing through a real material is composed, in general, of two parts: a conduction current and a displacement current. The displacement current may be thought as the elastic response of the material to the applied electric field. As we increase the magnitude of the electric field, the displacement current is stored within the material, and when the electric field is reduced, the material releases the current. The displacement current therefore does not reflect the change in electrostatic energy stored within the material.

In analogy, the magnetic field **H** represents how the magnetic dipole distribution of a given medium, including transport and reorientation, is influenced by a magnetic induction **B**. Both magnitudes are related through the expression:

$$\mathbf{H} = \bar{\bar{\mu}}^{-1}\mathbf{B} = \frac{\mathbf{B}}{\mu_0} - \mathbf{M} \tag{2.6}$$

, where, in general, $\bar{\bar{\mu}}$ will be also a 2^{nd} order (or rank) complex tensor, function as well of a variety of parameters such as the frequency, position, humidity, temperature, etc. (please notice that the symbol $^{-1}$ must be considered as a matrix inverse in the most general case). **M** is the magnetization (average magnetic dipole moment per unit volume) and μ_0 is the permeability of free space.

The electromagnetic field is required to satisfy the Maxwell equations at points where the permittivity and the permeability are continous. However, as one crosses the boundary between a particle and a medium for example, there is, in general, a sudden change in these properties. This change occurs over a transition region with thickness of the order of atomic dimenions. From a macroscopic point of view, therefore, there is a discontinuity at the boundary. At such boundary points we impose the following conditions on the fields:

$$\left.\begin{aligned} [\mathbf{E}_2(\mathbf{x}) - \mathbf{E}_1(\mathbf{x})] \times \hat{\mathbf{n}} = 0 \\ [\mathbf{H}_2(\mathbf{x}) - \mathbf{H}_1(\mathbf{x})] \times \hat{\mathbf{n}} = 0 \end{aligned}\right. \quad , \mathbf{x} \text{ on } S \tag{2.7}$$

, where the subscripts 2 and 1 represent the regions around and inside the particle, respectively, and $\hat{\mathbf{n}}$ is the outward directed normal to the surface S of the particle. The boundary conditions (2.7) are the requirement that the *tangential components* of **E** and **H** are continuous across a boundary separating media with different properties.

Along this dissertation, we will consider the light as a transversal electromagnetic wave, so that it has both an electric and a magnetic field associated that, when propagating in a homogeneous and isotropic medium, are perpendicular to each other and to the direction of propagation, as shown in Figure 2.1. For convenience, we will use the magnetic field **H** instead of the magnetic induction **B**, so that if the electric and magnetic fields are taken as plane waves oscillating in time, we may write:

$$\mathbf{E} = \mathbf{E}_0 \exp\left(i\mathbf{k} \cdot \mathbf{r} - i\omega t\right) \tag{2.8}$$

$$\mathbf{H} = \mathbf{H}_0 \exp\left(i\mathbf{k} \cdot \mathbf{r} - i\omega t\right) \tag{2.9}$$

, with $\mathbf{H}_0 = \sqrt{\varepsilon_m \varepsilon_0 / \mu_m \mu_0}\, \hat{\mathbf{k}} \times \mathbf{E}_0$ [8], being ε_m and μ_m the relative electric permittivity and magnetic permeability of the surrounding (ambient) medium, and $\hat{\mathbf{k}}$ the unit wave vector, whose magnitude k is related with the wavelength λ (measured in the medium in which the wave propagates) through the expression:

$$k = \frac{2\pi}{\lambda} \tag{2.10}$$

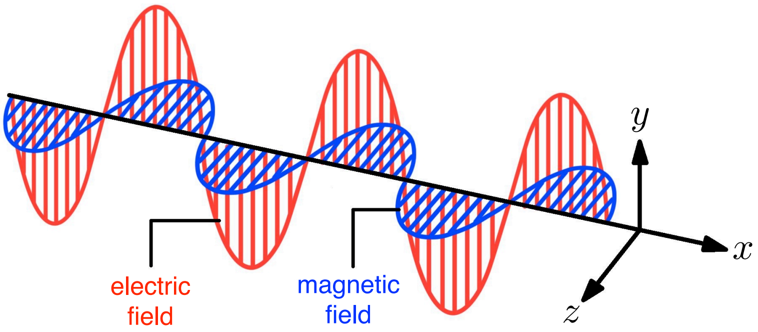

Figure 2.1: An electromagnetic wave, with its electric and magnetic fields oscillating in directions perpendicular to each other and to the direction of propagation.

The interaction of light with matter can be modeled assuming the latter to be composed of dipoles, both electric and magnetic. It is well-known that an electric dipole will acquire an electric dipole moment **p** in the presence of an external electric field **E**, according to:

$$\mathbf{p} = \varepsilon_m \varepsilon_0 \bar{\bar{\alpha}} \mathbf{E} \tag{2.11}$$

, where $\bar{\bar{\alpha}}$ is the electric polarizability tensor.

A magnetic dipole will also acquire a magnetic dipole moment $\mathbf{m}$ in the presence of an external magnetic field $\mathbf{H}$, according to the expression:

$$\mathbf{m} = \bar{\bar{\chi}}\mathbf{H} \tag{2.12}$$

, where $\bar{\bar{\chi}}$ is the magnetic polarizability tensor. Both $\bar{\bar{\alpha}}$ and $\bar{\bar{\chi}}$ may be related with the electric permittivity and the magnetic permeability of the medium, respectively. Depending on the density of the medium, the dipoles will interact between them to a greater or lesser extent, and we will be able to obtain different relations between these magnitudes (see Section 3.1). We will consider that two dipoles interact with each other when the presence of one is able to alter the oscillation of the other in a substantial way.

2.1 FIELDS FROM ELECTRIC AND MAGNETIC DIPOLES

The fields $\mathbf{E}_p$ and $\mathbf{H}_p$ produced by an electric dipole, $\mathbf{p}$, at distance r and direction $\mathbf{n}$ from the dipole can be expressed in the following form in SI units [15]:

$$\begin{aligned} \mathbf{E}_p = \frac{1}{4\pi\varepsilon_m\varepsilon_0}\Bigg[\mathbf{p}\frac{e^{ikr}}{r}\left(k^2 - \frac{1}{r^2} + \frac{ik}{r}\right) + \\ \mathbf{n}\left(\mathbf{n}\cdot\mathbf{p}\right)\frac{e^{ikr}}{r^3}\left(-k^2 + \frac{3}{r^2} - \frac{3ik}{r}\right)\Bigg] \end{aligned} \tag{2.13}$$

$$\mathbf{H}_p = \frac{1}{4\pi\sqrt{\mu_m\mu_0\varepsilon_m\varepsilon_0}}\left[\left(\mathbf{n}\times\mathbf{p}\right)\frac{e^{ikr}}{r^2}\left(k^2 + \frac{ik}{r}\right)\right] \tag{2.14}$$

Equations (2.13) and (2.14) describe both the near fields (nf) and the radiated fields (rf). The limit $\lambda \to \infty$ (or $k \to 0$) gives rise to the well known expression of the (near) electric field produced by an electric dipole $\mathbf{p}$ at distance r and direction $\mathbf{n}$ from the electric dipole, in the electrostatic limit:

$$\mathbf{E}_p^{nf} \approx \frac{1}{4\pi\varepsilon_m\varepsilon_0 r^3}\left[3\mathbf{n}\left(\mathbf{n}\cdot\mathbf{p}\right) - \mathbf{p}\right] \tag{2.15}$$

The oscillation of the magnetic field leads the oscillation of the electric field by a phase of $\pi/2$ rad:

$$\mathbf{H}_p^{nf} \approx ik\frac{1}{4\pi r^2\sqrt{\mu_m\mu_0\varepsilon_m\varepsilon_0}}\left(\mathbf{n}\times\mathbf{p}\right) \tag{2.16}$$

The radiated fields correspond to the terms decreasing like $1/r$. These are:

$$\mathbf{E}_p^{rf} \approx k^2 \frac{e^{ikr}}{4\pi\varepsilon_m\varepsilon_0 r}\left[\mathbf{p}-\mathbf{n}\left(\mathbf{n}\cdot\mathbf{p}\right)\right] \tag{2.17}$$

$$\mathbf{H}_p^{rf} \approx k^2 \frac{e^{ikr}}{4\pi r\sqrt{\mu_m\mu_0\varepsilon_m\varepsilon_0}}\left(\mathbf{n}\times\mathbf{p}\right) \tag{2.18}$$

They are related by $\mathbf{H}_p^{rf} = \sqrt{\varepsilon_m\varepsilon_0/\mu_m\mu_0}\;\mathbf{n}\times\mathbf{E}_p^{rf}$, which is a general relationship for radiation fields (plane waves).

Figure 2.2 shows the field lines of the real-valued electric $\mathbf{E}_p$ and magnetic $\mathbf{H}_p$ fields from an oscillating electric point dipole in vacuum. The color represents the magnitude of each field, normalized to 1 in both cases. As can be seen, the maximum value of the electric field $|\mathbf{E}_p|^{max} \approx 1200\,|\mathbf{H}_p|^{max} \gg \sqrt{\mu_0/\varepsilon_0}\,|\mathbf{H}_p|^{max} \approx 120\pi\,|\mathbf{H}_p|^{max}$, which would correspond to the far field (plane waves) case. Further details about the obtention of these field lines can be found in Appendix B.

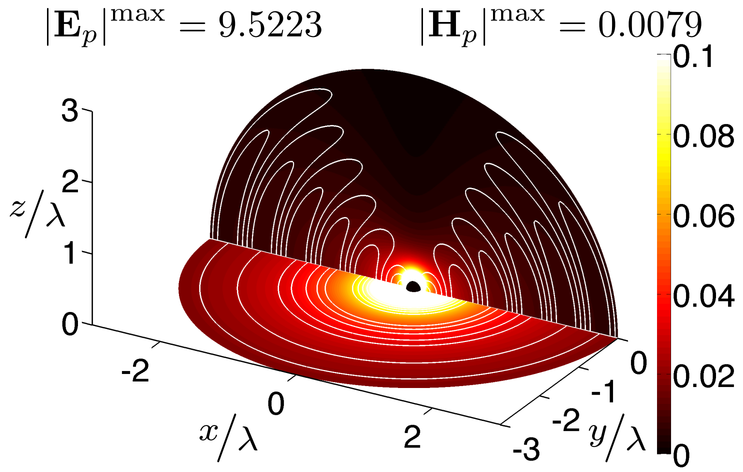

Figure 2.2: Field lines of the real-valued electric $\mathbf{E}_p$ (x-z plane) and magnetic $\mathbf{H}_p$ (x-y plane) fields from an oscillating z-directed electric point dipole in vacuum at $t = 0$, calculated from $r = \lambda/10$ to $r = 3\lambda$. The color shows the normalized magnitude of both $\mathbf{E}_p$ and $\mathbf{H}_p$ (both normalized to 1, please notice their respective maximum values).

The fields $\mathbf{E}_m$ and $\mathbf{H}_m$ produced by a magnetic dipole, $\mathbf{m}$, at distance r and direction $\mathbf{n}$ from the dipole are given by Jackson [16]:

$$\mathbf{E}_m = -\frac{1}{4\pi}\sqrt{\frac{\mu_m\mu_0}{\varepsilon_m\varepsilon_0}}\left(\mathbf{n}\times\mathbf{m}\right)\frac{e^{ikr}}{r^2}\left(k^2+\frac{ik}{r}\right) \tag{2.19}$$

$$\mathbf{H}_m = \frac{1}{4\pi}\left[\mathbf{m}\frac{e^{ikr}}{r}\left(k^2-\frac{1}{r^2}+\frac{ik}{r}\right)+\right.$$
$$\left.\mathbf{n}\left(\mathbf{n}\cdot\mathbf{m}\right)\frac{e^{ikr}}{r^3}\left(-k^2+\frac{3}{r^2}-\frac{3ik}{r}\right)\right] \tag{2.20}$$

We note that the fields of the magnetic dipole are obtained from those of the electric dipole by the *duality* transformations $\mathbf{E} \to \mathbf{H}$, $\mathbf{H} \to -\mathbf{E}$, $\varepsilon_m\varepsilon_0 \to \mu_m\mu_0$, $\mu_m\mu_0 \to \varepsilon_m\varepsilon_0$ and $\mathbf{p} \to \mu_m\mu_0\mathbf{m}$.

In analogy with the electric dipole, the corresponding near fields from a magnetic dipole $\mathbf{m}$ are given by:

$$\mathbf{E}_m^{nf} \approx -ik\sqrt{\frac{\mu_m\mu_0}{\varepsilon_m\varepsilon_0}}\frac{1}{4\pi r^2}\left(\mathbf{n}\times\mathbf{m}\right) \tag{2.21}$$

$$\mathbf{H}_m^{nf} \approx \frac{1}{4\pi r^3}\left[3\mathbf{n}\left(\mathbf{n}\cdot\mathbf{m}\right)-\mathbf{m}\right] \tag{2.22}$$

, where this time the oscillation of the electric field leads the oscillation of the magnetic field by a phase of $-\pi/2$ rad. The radiated fields, decreasing like $1/r$, are:

$$\mathbf{E}_m^{rf} \approx -k^2\sqrt{\frac{\mu_m\mu_0}{\varepsilon_m\varepsilon_0}}\frac{e^{ikr}}{4\pi r}\left(\mathbf{n}\times\mathbf{m}\right) \tag{2.23}$$

$$\mathbf{H}_m^{rf} \approx k^2\frac{e^{ikr}}{4\pi r}\left[\mathbf{m}-\mathbf{n}\left(\mathbf{n}\cdot\mathbf{m}\right)\right] \tag{2.24}$$

2.2 INTERACTION OF ELECTRIC AND MAGNETIC DIPOLES

We now consider the particularly simple case of only two electric dipoles interacting in the near field zone. Based on Equation (2.15), we can see that two aligned electric dipoles (longitudinal configuration) will produce on each other identical electric fields, as shown in Figure 2.3a. For zero or negligible phase shift, these fields are oriented in the same direction as the induced dipole moment, thus supporting each other.

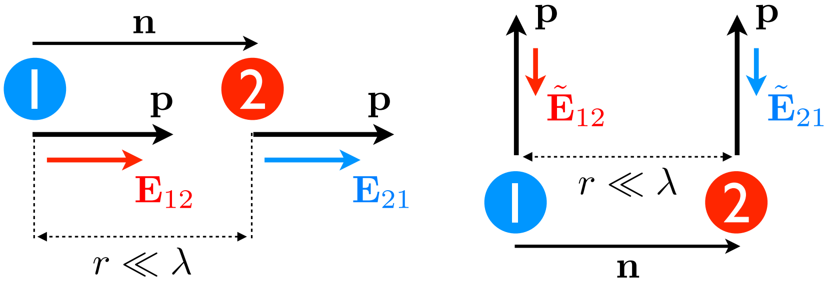

(a) Longitudinal configuration. (b) Transversal configuration.

Figure 2.3: Two interacting electric dipoles in the electrostatic limit.

$$\mathbf{E}_{12} = \mathbf{E}_{21} \approx \frac{1}{4\pi\varepsilon_m\varepsilon_0 r^3}\left(3\mathbf{p}-\mathbf{p}\right) = \frac{\mathbf{p}}{2\pi\varepsilon_m\varepsilon_0 r^3} \tag{2.25}$$

On the contrary, two parallel electric dipoles (transversal configuration) that are oriented perpendicular to their connecting vector, as shown in Figure 2.3b, will produce identical electric fields that are anti-parallel to the direction of the induced dipole moment, thus counteracting each other.

$$\tilde{\mathbf{E}}_{12} = \tilde{\mathbf{E}}_{21} \approx -\frac{\mathbf{p}}{4\pi\varepsilon_m\varepsilon_0 r^3} \tag{2.26}$$

Moreover, for a given interacting distance in the near field range, the longitudinal configuration is more efficient than the transversal one, in the sense that the electric field produced by the electric dipoles in the first case is twice that produced by the transversal configuration, as stated by Equations (2.25) and (2.26).

We now consider a finite array of both electric and magnetic dipoles. The electric and magnetic fields at the jth dipole resulting from the electric and magnetic dipole moments at kth ($\mathbf{p}_k$ and $\mathbf{m}_k$) are obtained from Equations (2.13), (2.14), (2.19) and (2.20). Working with the same formalism used by Mulholland et al. [15], we can express the total electric and magnetic fields at the jth dipole ($\mathbf{E}_j$ and $\mathbf{H}_j$) as:

$$\mathbf{E}_j = \frac{1}{\varepsilon_m\varepsilon_0}\sum_{k\neq j}^{N} \bar{\bar{\mathbf{C}}}_{jk}\mathbf{p}_k - \sqrt{\frac{\mu_m\mu_0}{\varepsilon_m\varepsilon_0}}\sum_{k\neq j}^{N} \bar{\bar{\mathbf{f}}}_{jk}\mathbf{m}_k \tag{2.27}$$

$$\mathbf{H}_j = \sum_{k\neq j}^{N} \bar{\bar{\mathbf{C}}}_{jk}\mathbf{m}_k + \sqrt{\frac{\varepsilon_m\varepsilon_0}{\mu_m\mu_0}}\sum_{k\neq j}^{N} \bar{\bar{\mathbf{f}}}_{jk}\mathbf{p}_k \tag{2.28}$$

, where:

$$\bar{\bar{\mathbf{C}}}_{jk} = \begin{pmatrix} a_{jk} + b_{jk}\left(r_{jk}^x\right)^2 & b_{jk}r_{jk}^x r_{jk}^y & b_{jk}r_{jk}^x r_{jk}^z \\ b_{jk}r_{jk}^y r_{jk}^x & a_{jk} + b_{jk}\left(r_{jk}^y\right)^2 & b_{jk}r_{jk}^y r_{jk}^z \\ b_{jk}r_{jk}^z r_{jk}^x & b_{jk}r_{jk}^z r_{jk}^y & a_{jk} + b_{jk}\left(r_{jk}^z\right)^2 \end{pmatrix} \tag{2.29}$$

$$\bar{\bar{\mathbf{f}}}_{jk} = \begin{pmatrix} 0 & -d_{jk}r_{jk}^z & d_{jk}r_{jk}^y \\ d_{jk}r_{jk}^z & 0 & -d_{jk}r_{jk}^x \\ -d_{jk}r_{jk}^y & d_{jk}r_{jk}^x & 0 \end{pmatrix} \tag{2.30}$$

The coefficients a_{jk}, b_{jk} and d_{jk} are shorthand expressions for the r-dependent functions in Equations (2.13), (2.14), (2.19) and (2.20):

$$a_{jk} = \frac{1}{4\pi}\frac{e^{ikr_{jk}}}{r_{jk}}\left(k^2 - \frac{1}{r_{jk}^2} + \frac{ik}{r_{jk}}\right) \tag{2.31}$$

$$b_{jk} = \frac{1}{4\pi}\frac{e^{ikr_{jk}}}{r_{jk}^3}\left(-k^2 + \frac{3}{r_{jk}^2} - \frac{3ik}{r_{jk}}\right) \tag{2.32}$$

$$d_{jk} = \frac{1}{4\pi}\frac{e^{ikr_{jk}}}{r_{jk}^2}\left(k^2 + \frac{ik}{r_{jk}}\right) \tag{2.33}$$

, where r_{jk} is the distance between the jth and the kth dipoles.

2.3 SCATTERING, ABSORPTION AND EXTINCTION

A parallel monochromatic beam of light propagates without any change in its intensity or polarization state. Suppose now that one or more particles are placed into the beam of electromagnetic radiation, as illustrated in Figure 2.4. The rate at which electromagnetic energy is received by a detector D aligned with the incident radiation from the particles is denoted by U. If the particles are removed, the power received by the detector is U_0, where $U_0 > U$. We say that the presence of the particles has resulted in extinction of the incident beam. If the medium in which the particles are embedded is non-absorbing, the difference $U_0 - U$ is accounted for by absorption in the particles (i.e. transformation of electromagnetic energy into other forms of energy) and scattering by the particles. This extinction (absorption plus scattering) depends on the chemical composition of the particles, their shape, size, orientation, the surrounding medium, the number of particles, and the polarization state and frequency of the incident light.

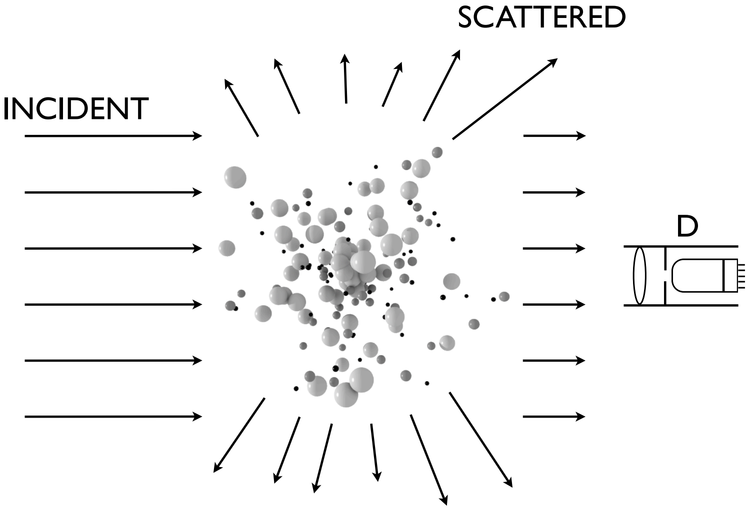

Figure 2.4: Extinction from a collection of particles. Adapted from Bohren and Huffman [8].

2.3.1 *Cross-sections and efficiency factors*

Cross-sections and efficiency factors are coefficients that determine the scattering characteristics of a particle or a particulate medium. Cross-section is a concept that is very useful in scattering theory. Consider a light beam incident on a particle. A portion of the radiant power would be scattered in all directions while the rest would flow through it. The scattering of the incident light beam is analogous to a virtual cross-section that scatters electromagnetic fields that are incident on it. The area of this virtual cross-section is proportional to the amount of radiant power that is scattered. This virtual cross-section (which is not equal to the physical cross-section of the particle) is called the scattering cross-section, denoted by C_{sca}, and defined as the ratio of the total radiant power scattered by a particle in all directions, W_{sca}, to the radiant power incident on the particle, I_i:

$$C_{sca} = \frac{W_{sca}}{I_i} \tag{2.34}$$

The absorption cross-section can be defined as the ratio of the total radiant power absorbed by a particle W_{abs}, to the radiant power incident on the particle, I_i:

$$C_{abs} = \frac{W_{abs}}{I_i} \tag{2.35}$$

Similarly, the extinction cross-section can be defined as the ratio of the radiant power removed by a particle from the incident beam, to the radiant power incident on the particle. In terms of the intensity distribution functions, the extinction cross-section is given by:

$$C_{ext} = \frac{W_{sca} + W_{abs}}{I_i} = C_{sca} + C_{abs} \tag{2.36}$$

, where W_{sca} and W_{abs} are the rates at which energy is scattered and absorbed by the particle respectively, and I_i is the incident irradiance.

As mentioned earlier, the virtual cross-section is not equal to the physical cross-section of the particle. When there is a need to relate both magnitudes, the efficiency factors are used. The scattering, absorption and extinction efficiencies are the ratios of their respective cross-sections to the physical cross-section of the particle (πr^2 in the case of a sphere, with r being its radius). The scattering, absorption and extinction efficiencies are denoted by the symbols Q_{sca}, Q_{abs} and Q_{ext} respectively.

3

OPTICAL PROPERTIES OF MATERIALS

The following chapter is intended to give a short account of the optical properties of materials, including the well-known Clausius-Mossotti relation and a overview of the main effective medium theories. We shall not forget our central goal with this dissertation, namely to develop a computational tool, based on the Discrete Dipole Approximation, able to solve the scattering problem by structures in the nanometer range. In order to properly model the optical response of such nanostructures, we need to appropriately describe their optical properties, for which, in Section 3.1, we shall derive the well-known Clausius-Mossotti relation for both the electric and the magnetic cases.

As a kind of example, Section 3.2 is dedicated to introduce and bring a fresh perspective to Kerker's null-scattering conditions, which allows us to shed new light on the radiative correction also introduced in Section 3.1.3. Finally, in Section 3.3, we present an overview of the principal effective medium theories suitable for modeling composite materials. In particular, we propose a new approach that considers the composite material to be made of discrete elements whose optical properties have been renormalized so that each constituent perceives the presence of the other according to its actual proportion in the composite. Results corresponding to this section are shown in Chapter 7.

3.1 CLAUSIUS-MOSSOTTI RELATION

We now proceed to obtain an expression that allows us to relate the microscopic properties of matter (such as the electric or magnetic polarizabilities) with macroscopically observable and measurable quantities such as the electric permittivity or the magnetic permeability. This is a non-trivial question and, as we will see, it is still under research. For simplicity, we will just concentrate on the particular case of an anisotropic medium embedded in vacuum (so that $\varepsilon_m = \mu_m = 1$).

3.1.1 *Electric polarizabilty*

The electric polarizability $\bar{\bar{\alpha}}$ represents the relative tendency of a charge distribution, such as the electron cloud of an atom or molecule, to be distorted from its normal shape by an external electric field **E**, which can come in the form of radiation or be caused by the presence of a near ion or dipole.

Diluted media

When dealing with a diluted medium, where the dipoles do not interact with each other, the electric field "felt" by each electric dipole is simply the incident electric field, so that the displacement field **D** can be separated in a contribution of the external field acting on the vacuum and another contribution due to the presence of the material:

$$\mathbf{D} = \bar{\bar{\varepsilon}}\mathbf{E} = \varepsilon_0 \bar{\bar{\varepsilon}}_r \mathbf{E} = \varepsilon_0 \mathbf{E} + n\mathbf{p} \Rightarrow n\mathbf{p} = \varepsilon_0 \left(\bar{\bar{\varepsilon}}_r - \bar{\bar{\mathbf{I}}}\right) \mathbf{E} \tag{3.1}$$

, where $n = {}^{N}/_{V}$ is the number density of electric dipoles and **p** is the electric dipole moment.

$$n\mathbf{p} = \varepsilon_0 \left(\bar{\bar{\varepsilon}}_r - \bar{\bar{\mathbf{I}}}\right) \mathbf{E} = n\varepsilon_0 \bar{\bar{\alpha}} \mathbf{E} \Rightarrow \boxed{\bar{\bar{\alpha}} = \frac{1}{n}\left(\bar{\bar{\varepsilon}}_r - \bar{\bar{\mathbf{I}}}\right)} \tag{3.2}$$

Dense media

On the contrary, in a dense medium, the interaction between the dipoles adds a new contribution that makes the electric field "felt" by each electric dipole somewhat larger. Indeed, the net field $\mathbf{E}_t$, also called *Lorentz local field*, may be written as [16]:

$$\mathbf{E}_t = \mathbf{E} + \frac{n\mathbf{p}}{3\varepsilon_0} \tag{3.3}$$

Making use of Equations (2.11) (with $\varepsilon_m = 1$), (3.1) and (3.3):

$$\mathbf{p} = \varepsilon_0 \bar{\bar{\alpha}} \mathbf{E}_t = \varepsilon_0 \bar{\bar{\alpha}} \left(\mathbf{E} + \frac{n\mathbf{p}}{3\varepsilon_0}\right) = \varepsilon_0 \bar{\bar{\alpha}} \left(\bar{\bar{\mathbf{I}}} + \frac{\bar{\bar{\varepsilon}}_r - \bar{\bar{\mathbf{I}}}}{3}\right) \mathbf{E}$$

$$n\mathbf{p} = \varepsilon_0 \left(\bar{\bar{\varepsilon}}_r - \bar{\bar{\mathbf{I}}}\right) \mathbf{E} = n\varepsilon_0 \bar{\bar{\alpha}} \left(\bar{\bar{\mathbf{I}}} + \frac{\bar{\bar{\varepsilon}}_r - \bar{\bar{\mathbf{I}}}}{3}\right) \mathbf{E}$$

$$\bar{\bar{\varepsilon}}_r - \bar{\bar{\mathbf{I}}} = \frac{n\bar{\bar{\alpha}}}{3}\left(\bar{\bar{\varepsilon}}_r + 2\bar{\bar{\mathbf{I}}}\right) \Rightarrow \bar{\bar{\alpha}} = \frac{3}{n}\left(\bar{\bar{\varepsilon}}_r - \bar{\bar{\mathbf{I}}}\right)\left(\bar{\bar{\varepsilon}}_r + 2\bar{\bar{\mathbf{I}}}\right)^{-1} \tag{3.4}$$

, which constitutes the so-called Clausius-Mossotti relation.

This expression relates the microscopic electric polarizability $\bar{\bar{\alpha}}$ of each electric dipole and the local, macroscopic, relative electric permittivity $\bar{\bar{\varepsilon}}_r$, in the limit of zero frequency $k \to 0$, $\lambda \to \infty$ (static fields), where k is the wavenumber of the incident radiation.

The volume of each dipole is given by $\nu = {}^{V}/_{N} = {}^{1}/_{n}$, so that the Clausius-Mossotti relation becomes:

$$\boxed{\bar{\bar{\alpha}}_{CM} = 3\nu\left(\bar{\bar{\varepsilon}}_r - \bar{\bar{\mathbf{I}}}\right)\left(\bar{\bar{\varepsilon}}_r + 2\bar{\bar{\mathbf{I}}}\right)^{-1}} \tag{3.5}$$

It is well known that for an isotropic spherical particle in the quasi-static limit (size $\rightarrow 0$), the electric plasmon resonance, also called "Fröhlich resonance", appears at $\varepsilon_r = -2$, as confirmed by Equation (3.5).

3.1.2 *Magnetic polarizabilty*

The magnetic polarizability $\bar{\bar{\chi}}$ is the degree of magnetization of a material in response to a magnetic field. Broadly speaking, it measures the ability of the microscopic magnetic dipole moments to align with the external field.

Diluted media

Again, if the magnetic field "felt" by each magnetic dipole is simply the incident magnetic field, the influence of an external magnetic induction **B** on the material may be separated in a contribution from the vacuum and another one from the response of the material [8] (assuming $\mu_m = 1$):

$$\mathbf{H} = \bar{\bar{\mu}}^{-1}\mathbf{B} = \frac{1}{\mu_0}\bar{\bar{\mu}}_r^{-1}\mathbf{B} = \frac{1}{\mu_0}\mathbf{B} - n\mathbf{m} \Rightarrow n\mathbf{m} = \frac{1}{\mu_0}\left(\bar{\bar{\mathbf{I}}} - \bar{\bar{\mu}}_r^{-1}\right)\mathbf{B} \quad (3.6)$$

, where $n = {}^{N}/_{V}$ is the number density of magnetic dipoles and **m** is the magnetic dipole moment.

$$n\mathbf{m} = \frac{1}{\mu_0}\left(\bar{\bar{\mathbf{I}}} - \bar{\bar{\mu}}_r^{-1}\right)\mathbf{B} = n\bar{\bar{\chi}}\mathbf{H} = n\bar{\bar{\chi}}\frac{1}{\mu_0}\bar{\bar{\mu}}_r^{-1}\mathbf{B} \Rightarrow \boxed{\bar{\bar{\chi}} = \frac{1}{n}\left(\bar{\bar{\mu}}_r - \bar{\bar{\mathbf{I}}}\right)} \quad (3.7)$$

Dense media

Similar to the Clausius-Mossotti relation, an equation for paramagnetic media may be found [17], that relates the microscopic magnetic polarizability $\bar{\bar{\chi}}$ of each magnetic dipole and the local, macroscopic, relative magnetic permeability $\bar{\bar{\mu}}_r$, in the limit of zero frequency $k \rightarrow 0$, $\lambda \rightarrow \infty$:

$$\boxed{\bar{\bar{\chi}}_{CM} = 3v\left(\bar{\bar{\mu}}_r - \bar{\bar{\mathbf{I}}}\right)\left(\bar{\bar{\mu}}_r + 2\bar{\bar{\mathbf{I}}}\right)^{-1}} \quad (3.8)$$

, where v is the volume of the dipole. Much the same as the electric plasmon resonance, the magnetic plasmon resonance appears at $\mu_r = -2$, as confirmed by Equation (3.8).

3.1.3 *Radiative correction (RC)*

Usually in electrodynamics, problems have been divided into two classes: one in which the sources of charge and current are specified and the resulting electromagnetic fields are calculated, and the other, known as "inverse problem", in which the external electromagnetic fields are specified and the motions of charged particles or currents are calculated (see Figure 3.1).

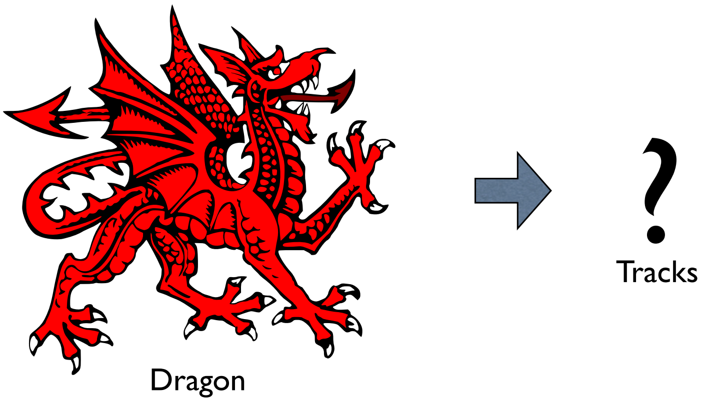

(a) The direct problem: Given a particle of specified shape, size, and composition, which is illuminated by a beam of specified irradiance, polarization, and frequency, determine the field everywhere. This is the "easy" problem; it consists of describing the tracks of a given dragon.

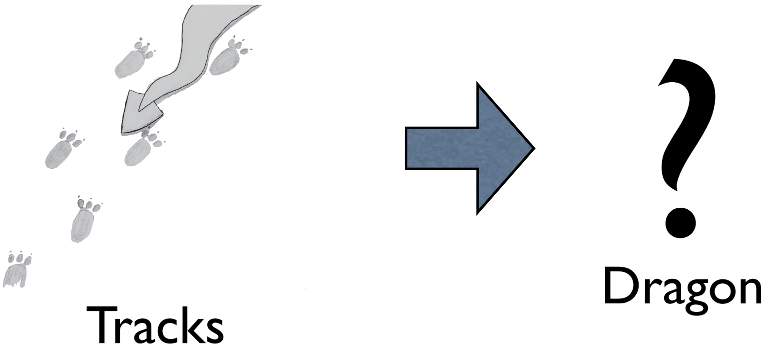

(b) The inverse problem: By a suitable analysis of the scattered field, describe the particle or particles that are responsible for the scattering. This is the "hard" problem; it consists of describing a dragon from an examination of its tracks.

Figure 3.1: The direct and the inverse problem. Adapted from Bohren and Huffman [8].

It is evident that this manner of handling problems in electrodynamics can be of only approximate validity. The motion of charged particles in external force fields necessarily involves the emission of radiation whenever the charges are accelerated. The emitted radiation carries off energy, momentum, and angular momentum and so must influence the subsequent motion of the charged particles. Consequently the motion of the sources of radiation is determined, in part, by the manner of emission of the radiation.

Equation (3.5) is exact in the zero frequency limit (see, e.g., Purcell [18], pp. 333-338; Jackson [16]; Kittel [19]), but not at finite frequencies. To see why it fails, consider a nonabsorptive material with real permittivity, in which case Equation (3.5) would imply real polarizability; however, a single dipole irradiated by a plane wave would scatter, and therefore attenuate, the plane wave, and this attenuation requieres that the polarizability has an imaginary part component in order that the oscillating dipole not be exactly in phase with the incident plane wave. As the considered electric fields are always periodic, we can add a "radiative reaction" assuming that, apart from the electric fields due to all other sources, each electric dipole is exposed to an electric field that takes account of this "radiative reaction", given by [20] (assuming again, for simplicity, an anisotropic medium embedded in vacuum):

$$\mathbf{E}_{\text{rad}} = \frac{ik^3}{6\pi\varepsilon_0}\mathbf{p} \tag{3.9}$$

The dipole moment is then given by the expression:

$$\mathbf{p} = \varepsilon_0 \bar{\bar{\alpha}}_{\text{CM}} \left(\mathbf{E} + \mathbf{E}_{\text{rad}}\right) \tag{3.10}$$

, which we may write in terms of the electric field **E** only, assuming an effective electric polarizability tensor that we shall simply refer to as $\bar{\bar{\alpha}}$:

$$\mathbf{p} = \varepsilon_0 \bar{\bar{\alpha}} \mathbf{E} \tag{3.11}$$

Using Equations (3.10) and (3.11):

$$\mathbf{p} = \varepsilon_0 \bar{\bar{\alpha}}_{\text{CM}} \left(\frac{1}{\varepsilon_0} \bar{\bar{\alpha}}^{-1} \mathbf{p} + \frac{ik^3}{6\pi\varepsilon_0} \mathbf{p} \right)$$

$$\bar{\bar{\mathbf{I}}} = \bar{\bar{\alpha}}_{\text{CM}} \bar{\bar{\alpha}}^{-1} + \frac{ik^3}{6\pi} \bar{\bar{\alpha}}_{\text{CM}}$$

, which implies an effective electric polarizability tensor $\bar{\bar{\alpha}}$:

$$\boxed{\bar{\bar{\alpha}} = \left(\bar{\bar{\mathbf{I}}} - \frac{ik^3}{6\pi} \bar{\bar{\alpha}}_{\text{CM}} \right)^{-1} \bar{\bar{\alpha}}_{\text{CM}}} \tag{3.12}$$

, which exactly coincides with Equation (3.5) in the limit of static fields ($k \to 0$). Please notice that this matrix multiplication is commutative, being Equation (3.12) completely equivalent to Eq. (27) from [21].

In the limit of long wavelength, $k \ll 1$, the radiative correction also holds for $\bar{\bar{\chi}}$, providing a finite frequency magnetic polarizability:

$$\boxed{\bar{\bar{\chi}} = \left(\bar{\bar{\mathbf{I}}} - \frac{ik^3}{6\pi}\bar{\bar{\chi}}_{CM}\right)^{-1} \bar{\bar{\chi}}_{CM}} \tag{3.13}$$

Please notice that we only took into account the radiative reaction correction coming from the electric field, which is an acceptable approximation [22].

3.2 KERKER'S NULL-SCATTERING CONDITIONS

In recent years, the response of nanosystems to both the electric and the magnetic part of an incident electromagnetic field in the visible part of the spectrum has become an important topic. Systems with relative electric permittivity and relative magnetic permeability different from 1 have been analyzed from either a theoretical or an experimental point of view [23–25]. Although these optical properties cannot be observed in natural materials, new engineered nano-structured materials, or *metamaterials*, have effective properties within such unusual intervals [26, 27]. Scatterers with these optical properties may show nonconventional scattering behaviors such as, for instance, negative refraction [28], which, for the case of bulk materials, could be useful for many applications: high-sensitivity biosensors, improved medical treatments, cloaked tools, or perfect lenses [29, 30].

In 1983, Kerker et al. [31] analyzed light scattering of a small isotropic spherical particle with arbitrary values for the relative electric permittivity (ε_r) and magnetic permeability (μ_r). They showed that, under certain conditions, the scattered intensity can be suppressed at given directions. In particular, they stated that if $\varepsilon_r = \mu_r$, light scattering in the backward direction is zero. As for forward scattering, it is inhibited when $\varepsilon_r = {}^{(4-\mu_r)}/_{(2\mu_r+1)}$. These results have gained new interest because the control of the directionality of light scattering by tuning the optical constants is the key for several applications in optical communications [32]. However, these conditions, which we shall refer to as Kerker's conditions, have been controversial due to the violation of the optical theorem when the second condition is satisfied [33].

In 2010, Alù and Engheta [33] proposed a correction in the expression of the extinction cross section. By means of this correction, they showed that under the zero-forward condition, although the scattered intensity is not zero in the forward direction, it is minimum with respect to the other scattering angles and the optical theorem is fulfilled. Here we go one step further by including the radiative correction in the conditions stated by Kerker et al. [31], obtaining newly revised Kerker's conditions. Thus we can show that a small (dipole-like) isotropic particle with relative optical constants (ε_r, μ_r) that satisfies these new conditions not only does not scatter either in the backward or the forward direction, but also with no violation of the optical theorem.

For a dipole-like particle, the backscattering or the forward scattering equals zero when both the electric and magnetic polarizabilities are equal, that is $\alpha = \chi$, or they have an opposite sign, $\alpha = -\chi$. Expanding Equations (3.12) and (3.13) for the case of an isotropic particle, we obtain:

$$\alpha = \frac{6\pi v(\varepsilon_r - 1)}{2\pi(\varepsilon_r + 2) - ivk^3(\varepsilon_r - 1)} \tag{3.14}$$

$$\chi = \frac{6\pi v(\mu_r - 1)}{2\pi(\mu_r + 2) - ivk^3(\mu_r - 1)} \tag{3.15}$$

, where v is the volume of the particle and k is the wavenumber of the incident electromagnetic radiation. Applying the previous equalities to these formulas, we can derive revised expressions for Kerker's conditions:

$$\begin{array}{c} \text{zero-backward} \\ (\alpha = \chi) \end{array} \Rightarrow \varepsilon_r = \mu_r \tag{3.16}$$

$$\begin{array}{c} \text{zero-forward} \\ (\alpha = -\chi) \end{array} \Rightarrow \varepsilon_r = \frac{\pi(4 - \mu_r) - ivk^3(\mu_r - 1)}{\pi(2\mu_r + 1) - ivk^3(\mu_r - 1)} \tag{3.17}$$

The zero-backward condition is equal to that proposed by Kerker et al. [31], but the revised zero-forward condition presents a correction in the imaginary part with respect to the Kerker's condition such that at least one of the optical constants should be complex. While the zero-backward condition can be satisfied for real values and no absorption, the zero-forward condition requires some degree of absorption in the scatterer. Because the imaginary part depends on v, it is directly related to the size and shape of the particle.

Figure 3.2 contains scattering diagrams corresponding to a spherical scatterer ($R = 4.96\,\text{nm}$) whose optical constants satisfy either Equations (3.16) or (3.17), illuminated by a plane wave with $\lambda = 500\,\text{nm}$ ($R/\lambda \sim 0.01$). The diagrams correspond to an incident electromagnetic field linearly polarized with the electric field parallel to the scattering plane (parallel polarization). We do not include the perpendicular polarization as it produces similar angular distributions. As can be seen, when the optical constants satisfy one of the previous relations (Equations (3.16) and (3.17)), light scattering patterns show a clear zero at the backward and forward directions, respectively.

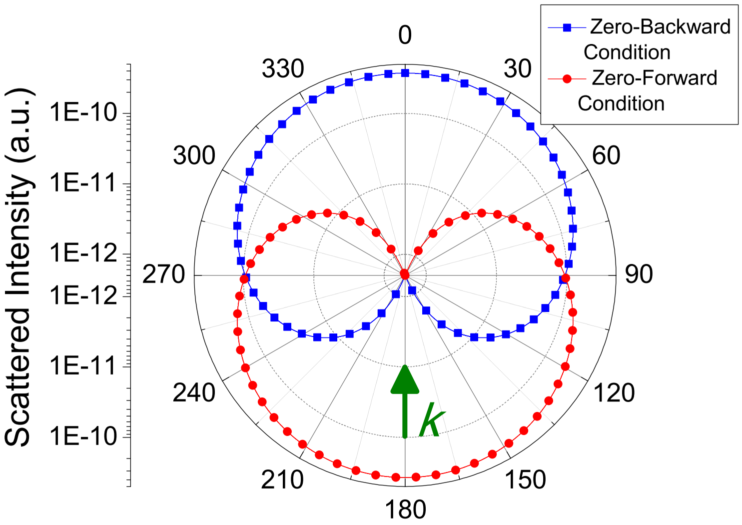

Figure 3.2: Scattering patterns of a spherical scatterer with $R = 4.96\,\text{nm}$ such that its optical constants satisfy either the new zero-forward (Equation (3.17)), $(\varepsilon_r, \mu_r) = \left(2, 0.4 - 3.88 \times 10^{-5} i\right)$, or the zero-backward (Equation (3.16)), $(\varepsilon_r, \mu_r) = (2, 2)$, conditions. The arrow represents the direction of the incident radiation.

García-Cámara et al. [34] showed that the second of Kerker's conditions, or the zero-forward condition, has an important exception when $\varepsilon_r = \mu_r = -2$, due to the excitation of two dipolar resonances, one electric and one magnetic. Although both conditions are satisfied simultaneously, only zero-backward scattering is actually observed. In their new form, the condition curves cross at the point:

$$\varepsilon_r = \mu_r = \frac{4\pi + i\nu k^3}{-2\pi + i\nu k^3} \tag{3.18}$$

This is a new form for the zero-forward exception. The correction we introduce is a size correction in the sense that when $\nu \to 0$, the conditions tend to that of Kerker's original form. In Figure 3.3, we show the evolution of μ_r (real and imaginary parts) as a function of ε_r, when they fulfill Equation (3.17), for several particle sizes. As can be seen, while the real part of μ_r does not change as R changes and it is similar to that obtained with the original Kerker's condition, the imaginary part becomes more negative as R increases. Although the variation of the imaginary part is quite small, it has important implications because it ensures that the optical theorem is satisfied, as will be shown.

The optical theorem establishes that the extinction cross section (C_{ext}) is proportional to the scattering amplitude in the forward direction, $S(0°)$, in the following way [35]:

$$C_{ext} = \frac{4\pi}{k^2} \Re\{S(0°)\} \tag{3.19}$$

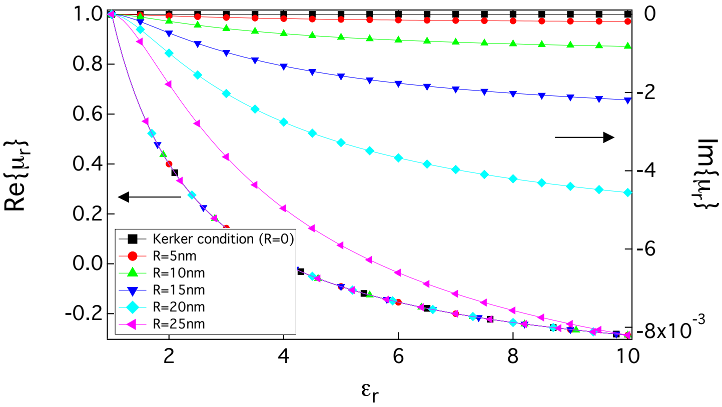

Figure 3.3: Real (continuos line, scale on the left) and imaginary (curves with symbols, scale on the right) part of the relative magnetic permeability as a function of the electric permittivity, following Equation (3.17), for several particle sizes. For comparison, the values of μ_r following the original Kerker's zero-forward condition are included.

, where $\Re$ stands for the real part. When the original zero-forward condition is satisfied, $S(0°) = 0$ and the extinction cross section is zero. The absorption cross section (C_{abs}) may also be zero because the optical constants may be both real, but the scattering cross section (C_{sca}) is not zero because the scattered intensity has important values at other directions (see Figure 3.2). These results are clearly inconsistent with $C_{ext} = C_{abs} + C_{sca}$. However, when the revised zero-forward condition proposed in Equation (3.17) is fulfilled, $(\varepsilon_r, \mu_r) = (2, 0.4 - 3.88 \times 10^{-5}i)$, the extinction is again zero, as stated by the optical theorem, but at the same time, this is consistent with the relation $C_{ext} = C_{abs} + C_{sca}$ because, at this point, $C_{sca} = -C_{abs}$.

In order to satisfy the zero-forward condition that we propose in Equation (3.17), either ε_r or μ_r must be complex if the other parameter is real and with negative values for the imaginary part, which gives rise to negative values of the absorption cross section or amplification cross section (see [36–38]). Scatterers with negative absorption are known as active objects, and they are the base of laser designs [39]. In Figure 3.4 we plot the evolution of C_{ext}, C_{abs} and C_{sca} for a spherical particle ($R = 4.96\,\text{nm}$) illuminated by a plane wave ($\lambda = 500\,\text{nm}$) as a function of the relative electric permittivity ε_r with a fixed value of the relative magnetic permeability ($\mu_r = 0.4 - 3.88 \times 10^{-5}i$).

To sum up Section 3.2, we have analyzed the inconsistency created by the zero-forward scattering condition proposed by Kerker et al. [31] and the optical theorem [35]. The introduction of the radiative correction in the generating expressions of the zero-forward condition produces a new form for such a condition, which complies with the optical theorem. In the limit $\nu \to 0$, the new expression tends to Kerker's. In addition, new conditions have size limitations similar

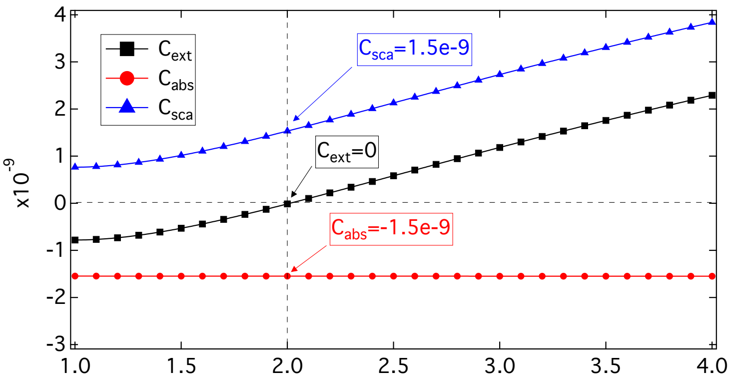

Figure 3.4: Evolution of the scattering, absorption (amplification) and extinction cross sections of a spherical particle ($R \simeq 5\,\mathrm{nm}$) as a function of ε_r when the relative magnetic permeability is fixed ($\mu_r = 0.4 - 3.88 \times 10^{-5}i$). The pair $(\varepsilon_r, \mu_r) = \left(2, 0.4 - 3.88 \times 10^{-5}i\right)$ satisfies the "new" zero-forward condition (Equation (3.17)).

to those of Kerker's [40]. We have also analyzed the zero-backward condition, obtaining that the expression stated by Kerker et al. [31] for zero-backward scattering is consistent and the radiative correction does not modify it. The proposed conditions cannot be seen as a minor revision of the original ones, because the effect is influenced by the size of the scatterer. The significance of these results is also reinforced by considering systems of particles designed to achieve light directionality in the nanoscale. Finally, these results highlight again the importance of considering the radiative correction in studies of small particles.

3.3 EFFECTIVE MEDIUM THEORIES

Effective medium theories define an effective dielectric function for a composite material in terms of the dielectric function of its components and their geometrical arrangement [41, 42]. The applicability of effective medium theories is restricted by the size of the structures composing the mixture: sufficiently large to preserve locally their own electromagnetic behavior and small enough for the composite to appear homogeneous compared to the wavelength of the interacting radiation.

The simplest way to obtain the optical properties of a composite material is performing a weighted average (WA), by simply taking into account the relative concentration of each constituent:

$$\varepsilon_{WA} = f \cdot \varepsilon_1 + (1-f) \cdot \varepsilon_2 \tag{3.20}$$

$$\mu_{WA} = f \cdot \mu_1 + (1-f) \cdot \mu_2 \tag{3.21}$$

, where f is the filling fraction of material 1 in the composite.

Over the last century, however, numerous effective medium theories have been proposed, being the Maxwell-Garnett and the Bruggeman expressions the most successful to explain the effective behavior of a large number of composites.

3.3.1 *Extended Maxwell-Garnett (EMG) theory*

If the mixture consists of isolated and poorly interacting spherical inclusions (ε_i, μ_i) embedded in an otherwise homogeneous matrix (ε_h, μ_h), the Maxwell-Garnett formula reads as [8]:

$$\varepsilon_{EMG} = \varepsilon_h \left[1 + \frac{3f\left(\frac{\varepsilon_i - \varepsilon_h}{\varepsilon_i + 2\varepsilon_h}\right)}{1 - f\left(\frac{\varepsilon_i - \varepsilon_h}{\varepsilon_i + 2\varepsilon_h}\right)} \right] \tag{3.22}$$

, where ε_{EMG} is the effective dielectric function, ε_h and ε_i are the dielectric functions of the homogeneous matrix and the inclusions respectively and f is again the filling fraction of material 1. We may extend the Maxwell-Garnett formula to materials with relative magnetic permeability $\mu_r \neq 1$, obtaining:

$$\mu_{EMG} = \mu_h \left[1 + \frac{3f\left(\frac{\mu_i - \mu_h}{\mu_i + 2\mu_h}\right)}{1 - f\left(\frac{\mu_i - \mu_h}{\mu_i + 2\mu_h}\right)} \right] \tag{3.23}$$

, where μ_{EMG} is the effective relative magnetic permeability and μ_h and μ_i are the relative magnetic permeability of the homogeneous matrix and the inclusion respectively.

3.3.2 *Extended Bruggeman (EB) theory*

Another commonly found topology corresponds to aggregate systems with some degree of interconnection between the two components. The role of matrix and inclusions cannot be clearly defined and the matrix where the phases are mixed is considered to be the effective medium itself. For these cases, the Bruggeman theory appears to be more appropriate [8]:

$$f\frac{\varepsilon_i - \varepsilon_{EB}}{\varepsilon_i + 2\varepsilon_{EB}} + (1-f)\frac{\varepsilon_h - \varepsilon_{EB}}{\varepsilon_h + 2\varepsilon_{EB}} = 0 \tag{3.24}$$

, where ε_{EB} is the effective dielectric function and ε_h and ε_i are the dielectric functions of the homogeneous matrix and the inclusions respectively. We may extend the Bruggeman formula to materials with relative magnetic permeability $\mu_r \neq 1$ as well, obtaining:

$$f\frac{\mu_i - \mu_{EB}}{\mu_i + 2\mu_{EB}} + (1-f)\frac{\mu_h - \mu_{EB}}{\mu_h + 2\mu_{EB}} = 0 \tag{3.25}$$

Note that the Bruggeman theory applies to a two-component mixture in which there are no distinguishable inclusions embedded in a definite matrix: both components are treated symmetrically. It might be more correct to say that it applies to a completely randomly inhomogeneous medium; it does not strictly apply to a particulate (segregated) medium because there is no way to decide which component is the particles and which the surrounding medium.

3.3.3 *Combined Approach (CA)*

In the simplest case, when considering targets immersed in dielectric media, the scattering calculation should be carried out using the *relative* optical properties (quotient between the optical properties of the target and those of the dielectric medium) as well as the wavelength in the surrounding medium. Following this idea, we have tried to devise expressions for effective optical properties taking into account the relative concentration of each constituent, to obtain an "effective ratio", according to the following hypothesized expressions:

$$\varepsilon_1^* = \frac{\varepsilon_1}{|\varepsilon_2|} + f \cdot \left(\varepsilon_1 - \frac{\varepsilon_1}{|\varepsilon_2|} \right) \tag{3.26}$$

$$\mu_1^* = \frac{\mu_1}{|\mu_2|} + f \cdot \left(\mu_1 - \frac{\mu_1}{|\mu_2|} \right) \tag{3.27}$$

$$\varepsilon_2^* = \frac{\varepsilon_2}{|\varepsilon_1|} + (1-f) \cdot \left(\varepsilon_2 - \frac{\varepsilon_2}{|\varepsilon_1|} \right) \tag{3.28}$$

$$\mu_2^* = \frac{\mu_2}{|\mu_1|} + (1-f) \cdot \left(\mu_2 - \frac{\mu_2}{|\mu_1|} \right) \tag{3.29}$$

, where f is again the filling fraction of material 1, (ε_1, μ_1) and (ε_2, μ_2) are the optical properties of material 1 and 2 respectively, and (ε_1^*, μ_1^*) and (ε_2^*, μ_2^*) are the renormalized optical properties for each material. These expressions are based only on the physical situation where a given material is surrounded by a dielectric medium, and have been obtained assuming a simple linear construction between two limiting values, corresponding to the filling fractions $f = 0$ (there is only material 2) and $f = 1$ (only material 1), as sketched in Figure 3.5:

Indeed, when f tends to 0, the renormalized dielectric function of a dipole of material 1 should approach the quotient $\varepsilon_1/|\varepsilon_2|$, corresponding to the situation where such dipole is surrounded by an equivalent dense dielectric material 2. On the other hand, when f tends to 1, its renormalized dielectric function should approach its original dielectric function ε_1.

In other words, our Combined Approach (CA) considers the material to be composed of more than one constituent, taking into account their relative concentration, but whose optical properties have been

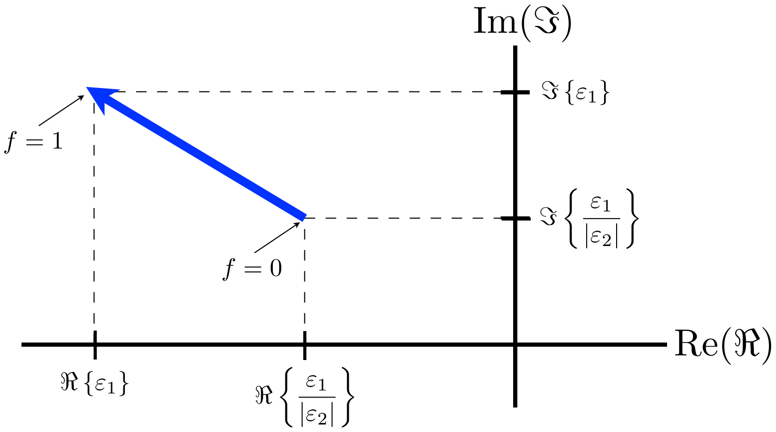

Figure 3.5: Sketch of the linear construction of our proposed Combined Approach, considering an arbitrary material 1 (supposed to be a metal, with $\Re\{\varepsilon_1\} < 0$), as given by Equation (3.26).

renormalized so that each constituent takes account of the presence of the other. Chapter 7 will be devoted to present a comparison of these approaches, showing results emphasizing the influences of optical properties of constituents and their concentration.

4

NUMERICAL METHODS IN ELECTROMAGNETICS

Light scattering is fundamental in order to understand the way light propagates in any media different from vacuum. At the most basic level, atoms and electrons, either as single scatterers, small groups (molecules) or in larger ensembles, are the cause of this scattering process. In the latest case, we can find bulk samples and individual objects particles. Optical properties of individual particles depend on the shape, size and bulk optical properties itself. Some examples of light scattering are phenomena such as the rainbow, red skies at sunset, the very bright colors of stained class windows, opacity of fog, etc. All these phenomena have motivated a lot of research and have leaded to significant developments in both fundamental and applied fields.

In recent times, there has been increasing interest in the scattering of an electromagnetic wave by a cylinder or a sphere, isolated or near a smooth surface [43, 44]. The interest in using light scattering techniques for solving this kind of problems is not only from a basic point of view but also for its applications in many fields, such as meteorology, astronomy, biology and medicine [45–48], atmospheric and surface contamination [49, 50], SERS [51, 52], optical particle characterization [53], etc.

Several theories have been developed for solving the problem of scattering from simple and complex structures, starting from Mie theory [54], developed in 1908 and able to solve analytically the scattering by an isolated sphere (Mie developed this solution in order to explain the colors of suspensions of small metallic particles in water). Although Mie offered an exact solution, in some cases, depending on the size and the refractive index, it might be quite complex. For this reason, there are many approximations available depending on the size and optical properties of the particles. Once simple scattering geometries were fully understood, researchers rapidly moved to more complex structures formed by more than one scatterer, sometimes in suspension others interacting with surfaces.

However, although for some scattering systems, some solutions and methods were proposed, in general, finding an analytical solution to complex scattering systems is in most cases impossible. This situation requires numerical solutions and it was not until recently, when more powerful computers were available, that significant advances appeared.

Obviously a review of all the numerical methods and theories developed for solving the problem of scattering from random structures, or even a list of the works related with this topic, is subject for an entire Thesis and therefore out of the scope of this dissertation. However, it is worthwhile mentioning here some excellent reviews on this topic [55–57], in which some of the most relevant works at this effect are described.

4.1 NUMERICAL SOLUTIONS: A REVIEW

Here we present a brief overview of the most widely used numerical methods for solving the scattering by arbitrary structures.

4.1.1 *Isolated particles*

MIE THEORY Although in this work we have not used the Mie theory in a direct way, we find necessary to give a general view of it as it constitutes one of the basis of light scattering. A more detailed description can be found in Bohren and Huffman [8].

In 1908, Mie [54] found the exact solution to the Maxwell equations for the optical response of a sphere of arbitrary size immersed in a homogeneous medium, with relative optical constants (ε_h, μ_h), and subjected to a plane monochromatic wave. For a homogeneous and isotropic sphere of radius a illuminated by a plane wave of angular frequency ω traveling in the z-direction and linearly polarized along the x-direction, the scattered electromagnetic field can be calculated in every point of space $\mathbf{r}$, and is given by:

$$\mathbf{E}_s(\mathbf{r}) = \sum_{n=1}^{\infty} E_n \left[i a_n \mathbf{N}^{(3)}_{eln} - b_n \mathbf{M}^{(3)}_{oln} \right] \tag{4.1}$$

$$\mathbf{H}_s(\mathbf{r}) = \sqrt{\frac{\varepsilon_h}{\mu_h}} \sum_{n=1}^{\infty} E_n \left[i b_n \mathbf{N}^{(3)}_{oln} + a_n \mathbf{M}^{(3)}_{eln} \right] \tag{4.2}$$

, where $E_n = i^n E_0 \, {}^{(2n+1)}/_{[n(n+1)]}$ with E_0 being the amplitude of the incident electric field, a_n and b_n are the Lorenz-Mie coefficients and $\mathbf{N}^{(3)}_{eln}$, $\mathbf{M}^{(3)}_{oln}$, $\mathbf{N}^{(3)}_{oln}$ and $\mathbf{M}^{(3)}_{eln}$ are the vector spherical harmonics. The Lorenz-Mie coefficients a_n and b_n are given by:

$$a_n = \frac{\mu_h m^2 j_n(mx)[x j_n(x)]' - \mu_r j_n(x)[mx j_n(mx)]'}{\mu_h m^2 j_n(mx)[x h^{(1)}_n(x)]' - \mu_r h^{(1)}_n(x)[mx j_n(mx)]'} \tag{4.3}$$

$$b_n = \frac{\mu_r m^2 j_n(mx)[x j_n(x)]' - \mu_h j_n(x)[mx j_n(mx)]'}{\mu_r m^2 j_n(mx)[x h^{(1)}_n(x)]' - \mu_h h^{(1)}_n(x)[mx j_n(mx)]'} \tag{4.4}$$

, where x is the size parameter, m and μ_r are the relative complex refractive index and magnetic permeability of the particle and j_n and $h_n^{(1)}$ are the Bessel and Hankel functions respectively. The optical response of the particle is then interpreted in terms of the different multipolar contributions.

T-MATRIX The T-matrix method, also known as the extended boundary condition method (EBCM), was first introduced by Waterman [58, 59] and provides a general formulation of the scattering from obstacles of arbitrary size and shape. An excellent review of this method has been published by Mishchenko et al. [60]. This method is a numerical technique based on the integral formulation of Maxwell's equations. It presents a general formulation in which the incident, internal and scattered fields are expanded in series of vector spherical wave functions. After applying the boundary conditions, a matrix is obtained, relating the known expansion coefficients of the incident light to the unknown expansion coefficients of the scattered field. This matrix receives the name of transition matrix or T-matrix and depends only on the physical properties of the scattering object (shape, size and optical constants) as well as on its orientation with respect to the coordinate system.

FINITE-DIFFERENCE TIME-DOMAIN (FDTD) This is another method broadly used in computational electromagnetism [61–64]. It consists on a direct implementation of Maxwell's time-dependent curl equations to solve the temporal variations of electromagnetic waves within a finite space that contains an object of arbitrary shape and properties. In practice, the space including the scatterer is discretized into a grid. The basic element of this discretization is the Yee cell [65, 66]. In general, any function of space and time u can be evaluated as:

$$u\left(i\Delta x, j\Delta y, k\Delta z, n\Delta t\right) = u^n_{i,j,k}$$

, where Δx, Δy, Δz are the lattice space increments in the coordinate directions, and i, j, k are integers. Δt is the time increment, assumed uniform over the observation interval, and n is an integer.

FDTD can have stability problems if the user does not choose the required parameters well. Also, it is important that the time domain step size has to be related to the minimum spatial discretization distance. This is one disadvantage when large objects with fine features are analyzed since the simulation time can grow drastically. Sometimes simulations can become unstable due to spurious reflections if the boundary conditions are not well implemented.

DISCRETE DIPOLE APPROXIMATION (DDA) Due to its relevance in this work, a specific section (Section 4.2) is devoted to this method.

4.1.2 *Scattering from particles near plane interfaces*

The use of light scattering techniques for the detection and characterization of particles upon flat surfaces has been a topic of increasing interest over the last several years because of its wide range of applicability in many fields of science and technology. Much effort has been devoted to modeling the scattered light from these surfaces, including the analysis of different effects and the testing of approximate numerical solutions. Among these effects are multiple scattering, cross-polarization, and enhanced backscattering. The development of models and approximate solutions contributes to our knowledge of the connection between the characteristics of the particle as a diffuser and the scattering patterns obtained from it. The origin of this question dates back to the problem studied by Sommerfeld [67] concerning a dipole in front of a conducting half-space. We outline below five approaches used to model the scattering from particles near plane interfaces and comment on the principal features [68].

EXTINCTION THEOREM The Ewald-Oseen extinction theorem (ET) [69, 70] is derived from an integral representation of the Maxwell equations that includes non-local extended boundary conditions at the surfaces. Two surface integral equations arise in the theoretical model. The first one connects the incident field with the induced surface electric current density on the surfaces, and the second connects this current density with the scattered field. The current density can be seen as the source of the scattered electromagnetic field. Discretization of the system permits the transformation of the first integral equation into a linear system of equations where the values of the surface current density in the surface elements are the unknowns to be determined. The second integral is then used to obtain the scattered field. This treatment of the scattering process is complete and exact in the sense that no additional physical assumptions or approximations are necessary. The multiple interactions substrate-particle and particle-particle are completely included, as well as any other effects, like the possible presence of surface-plasmon polaritons on metallic substrates. There is no restriction on the material of the particles and substrates, which can be dielectric or metallic. Any particle shape can also be considered. The model restrictions occur in the numerical implementation. The number of elements required for the surface (particles and substrate) discretization is related to the dimension of the linear system to be solved numerically. Therefore, the numerical stability of the solutions for a linear system with a large number of unknowns and the available computer memory are practical limitations. For this reason, this method has been almost exclusively employed for one-dimensional problems.

IMAGE THEORY This approach consists of solving the boundary conditions at the particle and at the plane surface simultaneously. To do this, the electromagnetic field components (incident, internal, scattered, and interaction) are expanded in terms of the vector spherical harmonics about two coordinate systems: one in real space about the center of the particle system and the other in image space located at the image of this coordinate system, opposite the plane surface. The incident field is composed of the field arriving directly from the source and from the source after reflecting on the plane substrate. The interaction field is the scattered field from the image particle and can be considered part of the incident field on the particle. The boundary conditions at the substrate surface are more difficult to satisfy. For a perfectly conducting substrate, the boundary conditions can be satisfied exactly by introducing interaction fields emanating from the image coordinate system that are the image of the scattered field emanating from the particle. Since a direct relationship exists between the scattered and interaction fields, all the field components can be found by translating the image fields expressed in vector spherical harmonics about the image coordinate system onto the particle coordinate system. The total scattered field is the superposition of the scattered fields from the source and from the image. When the substrate is not perfectly conducting, the boundary conditions at the substrate are more difficult to satisfy. Exact approaches to doing so require an integration over the plane surface. One approximate solution to this problem assumes that, like for the case of the perfectly conducting substrate, the interaction field is the image of the scattered field but multiplied by a Fresnel reflection coefficient at normal incidence; i.e., we assume the scattered field reflects on the substrate at normal incidence before striking the particle [71–76]. The total scattered far field at angle θ_s is the superposition of the scattered field from the particle and the image of the scattered field emanating from the image coordinate system multiplied by a Fresnel reflection coefficient calculated at angle θ_s The exact solution is asymptotically approached when either the particle is a large distance from the surface or the refractive index of the substrate approaches infinity. This approximation has been shown to provide quite reasonable results in calculating even the polarization state of the scattered light for particles resting on a substrate [75, 76]. This method can also be used to find the scattered field in the near-field region.

MODIFIED DOUBLE INTERACTION MODEL A modified version of the double-interaction model (DIM) developed by Nahm and Wolfe [77] can be used to obtain the electric far field scattered from a particle over a substrate. This model is a ray-tracing model that utilizes the Mie solution for the isolated scatterer to handle the scattering and diffraction by the sphere [78]. It includes the effects of the substrate by incorporating Fresnel reflections. Geometrically, the particle is illuminated by the direct (primary) beam and by the specularly reflected (secondary) beam. The secondary beam acquires a phase shift corresponding to the additional path length and undergoes a Fresnel reflection at the substrate. Two contributions to the total scattered field are generated in any direction by each of the two incoming beams. The first contribution is the beam directly scattered from the particle, and the second one is that scattered and reflected on the substrate. The latter undergoes a Fresnel reflection on the surface and is phase shifted an amount due to this additional path. The total scattered far field is the coherent superposition of the four contributions shown in Figure 4.1:

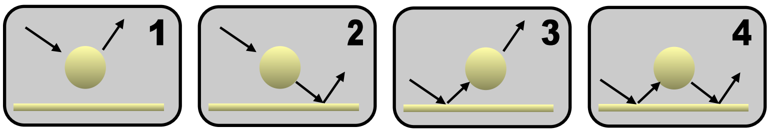

Figure 4.1: Sketch of the four contributions to the scattering: (1) the component of the primary beam that is directly scattered by the particle to the detector; (2) the component of the primary beam that is scattered by the particle then reflected on the substrate before reaching the detector; (3) the component of the secondary beam that is directly scattered by the particle to the detector; and (4) the component of the secondary beam that is scattered by the particle then reflected on the substrate before reaching the detector.

The interaction of the particle with its image is not taken into account. If the particle is illuminated at normal incidence, it completely obscures the image particle; i.e., it causes a shadowing effect [79, 80]. This occurs to a lesser extent at other oblique incident angles. This effect reduces the amplitude of the second, third and fourth scattering components depending on the illumination and observation angles. The geometrical shadowing factor depen- dent on the incident and scattering angles is introduced on these components to account for this effect. The shadowing factor is a first order correction to the interaction term handled rigorously in the image theory method. The major advantage of this model is its transparency. Any physical parameter (e.g., scattering components, enhanced backscattering, shadowing factors, etc.) can be analyzed as a function of any other parameter (scattering angle, particle size, etc.). This model allows for rapid calculations of the scattering intensities for any incident and scattered polarization state. This model can also be applied to particles with regular or irregular shapes because the only requirement is the knowledge of the scattering from the isolated particle. The substrate may also be either metallic or dielectric.

RAY TRACING MODEL The last method we consider is a pure geometrical optics approach. In principle, this is only valid when the wavelength is small compared to the particle size. The approximation is relatively simple and straightforward. From a geometrical point of view, a plane wave incident on a metallic object is a beam of parallel rays of uniform density that is reflected by the object and the substrate. When a ray strikes a boundary, it undergoes a Fresnel refraction or reflection and continues propagating until it strikes another boundary or is sent into the far field. The scattered field is then obtained as the coherent addition of the group of rays emerging from the system with a common angle (small interval of angles). Multiple scattering is inherently considered in this calculus in the included multiple reflections between particle and substrate or between particles. The size of the scattering features must be, in principle, large compared to the incident wavelength. However, the results show that, even for particles with sizes of the order of the wavelength, the method reproduces surprisingly good fits to experiment when the observation is far from the specular direction (where the diffraction effects are less important). It is particularly efficient in calculating backscattering and cross-polarization. Further improvements (implementing the geometrical theory of diffraction) make this method more accurate, and its range of validity may be extended toward the small particle region.

DDSURF DDSURF is a code based on the Coupled-Dipole Method (CDM) for modeling of electromagnetic light scattering from features on a plane surface, written by Schmehl et al. [81]. It was especially developed as a tool for the semiconductor industry, where the optical detection and characterization of surface defects and contaminants is essential for improving the production performance. The code is not being maintained by the authors anymore, in spite of the great success at the beginning.

4.2 CONVENTIONAL DISCRETE DIPOLE APPROXIMATION (DDA)

One of the most widely used methods for modeling the optical response of nano-scale objects is the DDA [82], which allows for calculating scattering and absorption of light by irregular particles. The DDA relies on the same direct-space discretization scheme that is widely used to study the scattering of light by finite objects. Specifically, the assumptions of this methodology are:

- The volume of the object is considered as the union of non-overlapping, simple connected cells j of volume v_j $(j = 1, \dots, N)$ with the total volume of the object given by $V = \sum_j v_j$.
- Each cell j is assumed homogeneous in its material properties and, because of its small size, the electric and magnetic fields are considered as constant throughout the volume v_j.

There are two criteria for validity of the DDA [82]: (1) $|n|kd \lesssim 1$ (so that the dipoles lattice spacing d is small as compared both with the wavelength within the material, $^{2\pi}/_{(\Re\{n\}k)}$, and with the attenuation length (or "skin depth"), $^{2\pi}/_{(\Im\{n\}k)}$, with $\Re\{n\}$ and $\Im\{n\}$ being the real and imaginary parts of the complex refractive index of the material and $k = {}^{\omega}/_{c}$); and (2) d must be small enough (N must be large enough) to describe the target shape with sufficient precision.

In conventional DDA [56, 82], the optical response of each cell is modeled as the excitation of an oscillating electric point dipole $\mathbf{p}_j$ located in its center. Cells are built up from a simple cubic lattice. Each induced electric dipole $\mathbf{p}_j$ is determined by an electric polarizability tensor $\bar{\bar{\alpha}}_j$, reacting to a local electric field $\mathbf{E}_j$, through Equation (2.11), where $\mathbf{p}_j$ is the instantaneous (complex) dipole moment and $\mathbf{E}_j$ is the instantaneous (complex) electric field at position j due to all sources external to the jth cell, i.e. due to the incident electric field at that site and the contributions of all the other $N-1$ oscillating dipoles:

$$\mathbf{E}_j = \mathbf{E}_j^{\text{inc}} - \sum_{k \neq j} \bar{\bar{\mathbf{A}}}_{jk} \mathbf{p}_k \tag{4.5}$$

, where $\mathbf{E}_j^{\text{inc}} = \mathbf{E}_0 \exp(i\mathbf{k} \cdot \mathbf{r}_j)$ is the incident electric field at position j and $-\bar{\bar{\mathbf{A}}}_{jk}\mathbf{p}_k$ is the electric field at the jth dipole resulting from the kth oscillating electric dipole, given by Equation (2.13).

4.3 EXTENDED DDA

In the E-DDA [83], both the electric and magnetic responses of the material are taken into account by considering the excitation of both an oscillating electric and magnetic point dipole located in the center of each cell. In addition, both the relative electric permittivity, $\bar{\bar{\varepsilon}}_r$, and the relative magnetic permeability, $\bar{\bar{\mu}}_r$, of the material, are 2nd order (or rank) tensors. The induced electric dipole $\mathbf{p}_j$ under the action of a local electric field $\mathbf{E}_j$ is given by Equation (2.11). In the same way, the induced magnetic dipole $\mathbf{m}_j$ under the influence of a local magnetic field $\mathbf{H}_j$ is given by Equation (2.12).

$\mathbf{E}_j$ and $\mathbf{H}_j$ are the instantaneous (complex) electric and magnetic fields at position j due to all sources external to the jth cell, i.e. due to the incident electromagnetic field at that site and the contributions of all the other $N-1$ oscillating electric and magnetic dipoles:

$$\begin{bmatrix} \mathbf{E}_j \\ \mathbf{H}_j \end{bmatrix} = \begin{bmatrix} \left(\varepsilon_m \varepsilon_0 \bar{\bar{\alpha}}_j\right)^{-1} \mathbf{p}_j \\ \bar{\bar{\chi}}_j^{-1} \mathbf{m}_j \end{bmatrix} = \begin{bmatrix} \mathbf{E}_j^{\mathrm{inc}} \\ \mathbf{H}_j^{\mathrm{inc}} \end{bmatrix} - \sum_{k \neq j} \begin{bmatrix} \bar{\bar{\mathbf{A}}}_{jk}^{(ee)} & \bar{\bar{\mathbf{A}}}_{jk}^{(eh)} \\ \bar{\bar{\mathbf{A}}}_{jk}^{(he)} & \bar{\bar{\mathbf{A}}}_{jk}^{(hh)} \end{bmatrix} \cdot \begin{bmatrix} \mathbf{p}_k \\ \mathbf{m}_k \end{bmatrix} \tag{4.6}$$

, where $\mathbf{E}_j^{\mathrm{inc}} = \mathbf{E}_0 \exp\left(i\mathbf{k} \cdot \mathbf{r}_j\right)$ and $\mathbf{H}_j^{\mathrm{inc}} = \mathbf{H}_0 \exp\left(i\mathbf{k} \cdot \mathbf{r}_j\right)$ are the incident electric and magnetic fields at position j. $-\bar{\bar{\mathbf{A}}}_{jk}^{(ee)} \mathbf{p}_k$ and $-\bar{\bar{\mathbf{A}}}_{jk}^{(eh)} \mathbf{m}_k$ are the electric fields at the jth dipole resulting from the kth oscillating electric and magnetic dipoles respectively, given by Equations (2.13) and (2.19). Equally, $-\bar{\bar{\mathbf{A}}}_{jk}^{(he)} \mathbf{p}_k$ and $-\bar{\bar{\mathbf{A}}}_{jk}^{(hh)} \mathbf{m}_k$ are the magnetic fields at the jth dipole resulting from the kth oscillating electric and magnetic dipoles respectively, given by Equations (2.14) and (2.20). Notice that the only difference between Equation (4.6) and Equations (2.27), (2.28) is the addition of the incident electromagnetic field and the formalism employed.

4.3.1 *Solving the system of equations*

The electric ($\bar{\bar{\alpha}}_j$) and magnetic ($\bar{\bar{\chi}}_j$) polarizability tensors are given by Equation (3.12) and Equation (3.13) respectively. The most natural way of solving Equation (4.6) is just as Purcell and Pennypacker [84] tried it in their original paper, this is, considering the case as a self-consistent problem. This problem has as a special feature the fact that, in order to solve the problem, we need to know the solution beforehand. Figure 4.2 shows this fact. As can be seen, the problem resembles a spinning carousel. This carousel has the ability that if a possible solution to the problem (initial condition) rides in, it will get closer to the true solution (unknown) as the carousel spins more and more.

This solving method, based on successive approximations, was implemented in the very first version of E-DDA (the one that we shall refer to as *early* E-DDA), proving to be very slow and not convergent on most cases. Being an iterative technique, an initial guess for the dipole moments is required. Here, we assume that the electric and magnetic dipoles are initially excited by the incident electromagnetic field only, so that:

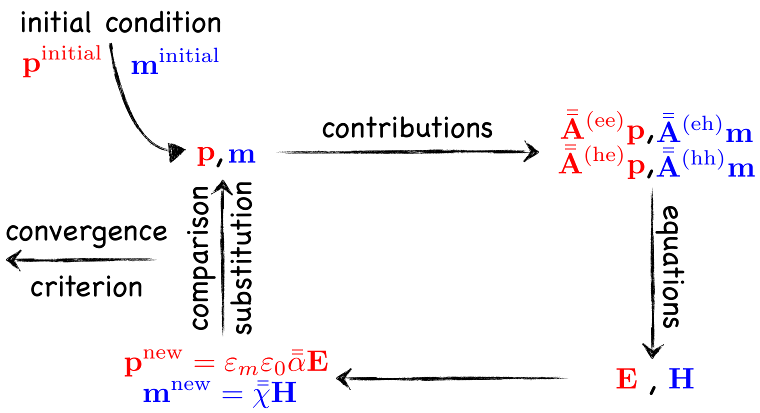

Figure 4.2: Diagram of the self-consistent problem set out to solve Equation (4.6). The iterative process starts with an initial condition, from which the different contributions that produce the new external fields can be calculated. The new external fields allow us to calculate the new dipole moments. Then we obtain the difference between new and old magnitudes. The process ends when a suitable convergence criterion is fulfilled.

$$\mathbf{p}^{\text{initial}} = \varepsilon_m \varepsilon_0 \bar{\bar{\alpha}} \mathbf{E}^{\text{inc}} \tag{4.7}$$

$$\mathbf{m}^{\text{initial}} = \bar{\bar{\chi}} \mathbf{H}^{\text{inc}} \tag{4.8}$$

In each iteration, a new solution for the exciting fields, $\mathbf{p}^{\text{new}}$ and $\mathbf{m}^{\text{new}}$, is found. The cut-off criterion for self-consistency in all our calculations, if not stated otherwise, is:

$$\frac{|\mathbf{p}^{\text{new}} - \mathbf{p}|}{|\mathbf{p}|} \leqslant \text{TOL} \qquad \text{and} \qquad \frac{|\mathbf{m}^{\text{new}} - \mathbf{m}|}{|\mathbf{m}|} \leqslant \text{TOL} \tag{4.9}$$

, where TOL is the error tolerance, set to $\text{TOL} = 10^{-5}$ in order to solve the problem to high accuracy (see Section 11 in [85]).

The most recent version of E-DDA implements the Complex-Conjugate Gradient (CCG) Method with enhancement to maintain convergence in finite precision arithmetic [86] in order to solve Equation (4.6). It is convenient to rewrite the system of equations using its associated matrix form. If we assume that $\bar{\bar{\mathbf{A}}}_{jk}$ are the off-diagonal elements, we may define the diagonal ones as:

$$\begin{aligned} \bar{\bar{\mathbf{A}}}_{jj}^{(ee)} &= -\left(\varepsilon_m \varepsilon_0 \bar{\bar{\alpha}}_j\right)^{-1} & \qquad \bar{\bar{\mathbf{A}}}_{jj}^{(eh)} &= 0 \\ \bar{\bar{\mathbf{A}}}_{jj}^{(he)} &= 0 & \qquad \bar{\bar{\mathbf{A}}}_{jj}^{(hh)} &= -\bar{\bar{\chi}}_j^{-1} \end{aligned} \tag{4.10}$$

So that Equation (4.6) can be reformulated as a set of 2N inhomogeneous, vectorial, complex and linear equations in the form:

$$\sum_{k=1}^{N} \begin{bmatrix} \bar{\bar{\mathbf{A}}}_{jk}^{(ee)} & \bar{\bar{\mathbf{A}}}_{jk}^{(eh)} \\ \bar{\bar{\mathbf{A}}}_{jk}^{(he)} & \bar{\bar{\mathbf{A}}}_{jk}^{(hh)} \end{bmatrix} \cdot \begin{bmatrix} \mathbf{p}_k \\ \mathbf{m}_k \end{bmatrix} = \begin{bmatrix} \mathbf{E}_j^{inc} \\ \mathbf{H}_j^{inc} \end{bmatrix} \tag{4.11}$$

or more conveniently in terms of the exciting electric and magnetic fields $\mathbf{E}_k$ and $\mathbf{H}_k$ instead of $\mathbf{p}_k$ and $\mathbf{m}_k$:

$$\bar{\bar{\mathbf{A}}}\mathbf{x} = \mathbf{b} \tag{4.12}$$

, where $\bar{\bar{\mathbf{A}}}$ is a $6N \times 6N$ matrix, $\mathbf{x}$ is the 6N-dimensional vector of unknowns given by $\mathbf{x} = (\mathbf{E}_1, \mathbf{H}_1, \mathbf{E}_2, \mathbf{H}_2, \dots, \mathbf{E}_N, \mathbf{H}_N)$ and $\mathbf{b}$ is the 6N-dimensional vector of independent terms containing the incident field at each lattice site: $\mathbf{b} = (\mathbf{E}_1^{inc}, \mathbf{H}_1^{inc}, \mathbf{E}_2^{inc}, \mathbf{H}_2^{inc}, \dots, \mathbf{E}_N^{inc}, \mathbf{H}_N^{inc})$.

4.3.2 *Code Performance*

The main achievement of our code in its current version is versatility, in the sense that it is able to deal with situations involving arbitrary electric and magnetic susceptibilities in a broad sense. In the following chapters we shall survey the most representative situations at reach for this code, from the most basic one of a dielectric, to the most generals, such as metals, metamaterials (in particular left-handed materials, with real parts of both ε_r and μ_r negative), magneto-optical materials (with $\bar{\bar{\varepsilon}}_r$ an antisymmetric tensor) or even both electrically and magnetically anisotropic materials. Some of these situations admit direct comparison with past DDA versions (see Table 4.1), while other can only be treated with other calculations methods, and not in a feasible way. The former will contribute to validate our code, while the latter constitute genuine novel results. Both together, prove the potential of E-DDA as a new and reliable computing tool. It is interesting to remark that the polarization state of the incident radiation can be arbitrary (elliptical in the most general case), allowing polarimetric calculations to be performed.

The extinction cross section is computed from the forward scattering amplitude using the optical theorem [20] for both electric and magnetic dipole moments [22]:

$$C_{ext} = \frac{k}{\varepsilon_m \varepsilon_0 |\mathbf{E}_0|^2} \sum_{j=1}^{N} \Im\left\{ \left(\mathbf{E}_j^{inc}\right)^* \cdot \mathbf{p}_j + \mu_m \mu_0 \left[\left(\mathbf{H}_j^{inc}\right)^* \cdot \mathbf{m}_j \right] \right\} \tag{4.13}$$

MATERIAL	DDA	E-DDA
dielectric	✔	✔
metal	✔	✔
magneto-optical	✘	✔
negative index material	✘	✔
bianisotropic	✘	✔

Table 4.1: Materials at hand for both conventional DDA and E-DDA.

The absorption cross section is obtained by summing over the rate of energy dissipation by each of the dipoles (electric and magnetic), as given by [22]:

$$C_{\mathrm{abs}} = \frac{k}{\varepsilon_m \varepsilon_0 |\mathbf{E}_0|^2} \sum_{j=1}^{N} \left\{ \Im\left(\mathbf{E}_j^* \cdot \mathbf{P}_j\right) - \frac{k^3}{6\pi \varepsilon_m \varepsilon_0} |\mathbf{P}_j|^2 + \mu_m \mu_0 \left[\Im\left(\mathbf{H}_j^* \cdot \mathbf{M}_j\right) - \frac{k^3}{6\pi} |\mathbf{M}_j|^2 \right] \right\} \tag{4.14}$$

The scattering cross-section can be easily obtained by the difference of the extinction and absorption cross-sections: $C_{\mathrm{sca}} = C_{\mathrm{ext}} - C_{\mathrm{abs}}$, but a more convenient way is to compute the far-field scattered by the object [22]:

$$C_{\mathrm{sca}} = \frac{k^2}{16\pi^2 \varepsilon_m \varepsilon_0 |\mathbf{E}_0|^2} \times \int \left| \sum_{j=1}^{N} \exp(-ik\mathbf{n} \cdot \mathbf{r}_j) \left\{ \frac{1}{\sqrt{\varepsilon_m \varepsilon_0}} \left[\mathbf{p}_j - (\mathbf{n} \cdot \mathbf{p}_j)\mathbf{n} \right] - \sqrt{\mu_m \mu_0}\, \mathbf{n} \times \mathbf{m}_j \right\} \right|^2 d\Omega \tag{4.15}$$

, where **n** is a unit vector in the direction of scattering. Additionally, we can also define the phase-lag cross-section in terms of the imaginary part of the forward-scattering amplitude [20]:

$$C_{\mathrm{pha}} = \frac{k}{2\varepsilon_m \varepsilon_0 |\mathbf{E}_0|^2} \sum_{j=1}^{N} \Re\left\{ \left(\mathbf{E}_j^{\mathrm{inc}}\right)^* \cdot \mathbf{p}_j + \mu_m \mu_0 \left[\left(\mathbf{H}_j^{\mathrm{inc}}\right)^* \cdot \mathbf{m}_j \right] \right\} \tag{4.16}$$

Conventional angular scattering patterns (scattered intensities) can be obtained, as well as the full Mueller Matrix of the system, completing the far-field results list. As for local magnitudes, these include dipole moments, fields or Poynting vector distributions, local phase functions, etc.

The scattered intensity I is defined as the absolute value of the time-averaged Poynting vector $\langle \mathbf{S} \rangle$, calculated as $\langle \mathbf{S} \rangle = \frac{1}{2}\Re\{\mathbf{E} \times \mathbf{H}^*\}$, where

E and **H** are the scattered electric and magnetic fields respectively [8]. Of course, the scattered intensity is strongly angle dependent.

Part II

RESULTS

The main results obtained within this Thesis are described in Chapters 5 to 8. An opening chapter is devoted to the initial validation of the results obtained with the E-DDA code. Then some applications of the method are presented, emphasizing the versatility of the E-DDA implementation, including:

- Magneto-optical materials (Chapter 6).
- Composite materials (Chapter 7).

Finally, Chapter 8 serves as a placeholder chapter, where a variety of works, all connected in different ways to the main body of the Thesis, is presented. A short Chapter 9 with a summary and the main conclusions closes this part.

5

VALIDATION OF THE E-DDA

This chapter is devoted to the validation of the computational tool that we call E-DDA, presented in Section 4.3. The chapter is divided into three sections. The first one refers to several self-consistency tests made with an early version of the code. Section 5.2 is devoted to check the reliability of our results with a full-featured version of the code, comparing them to the well-proved DDSCAT code from Draine and Flatau [82, 85].

Finally, Section 5.3 shows genuine novel results obtained with E-DDA. These results do not admit direct comparison with past DDA versions, although they correspond to a situation in which we already have a knowledge of the system behavior, namely the well-known null-scattering conditions proposed by Kerker et al. [31], found valid for anisotropic media as well.

5.1 SELF-CONSISTENCY TESTS

Because at the beginning the E-DDA code had important limitations, results in this section have been obtained for very small spherical particles, in order to keep the total number of dipoles as low as possible. Moreover, the material of which these particles are made from was chosen to be dielectric, in order to keep the influence of the optical properties as low as possible. The extinction efficiency Q_{ext} is the most experimentally accessible parameter as it takes account of both absorption and scattering, so we have used it in all cases as the representative solution for the electromagnetic problem.

5.1.1 *Symmetry tests*

A sphere has total symmetry, so that theoretically, we should obtain the same solution independent from the incident angle. The extinction efficiency for a sphere of radius $R = 6\,\text{nm}$ is shown in Figure 5.1, varying the incidence angle (please notice the scale and the magnitude of the variations, with relative value $\sim 10^{-5}$).

This deviation from the theoretical prediction must be due to numerical errors only, since we are modifying the direction of the incident beam with respect to the cartesian axes chosen for the discretization of the sphere. Indeed, a statistical analysis of the data allows for obtaining a mean value $\bar{Q}_{ext} = 5.42423 \times 10^{-6}$ and a standard deviation $\sigma_s = 4.96258 \times 10^{-11}$.

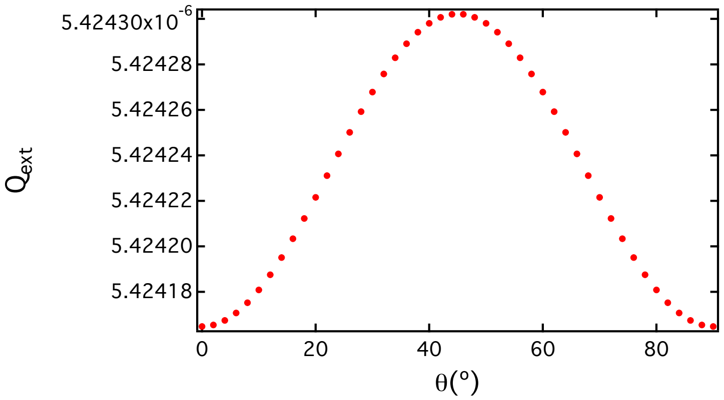

Figure 5.1: Extinction efficiency as a function of the incidence angle for a sphere of radius $R = 6\,\text{nm}$ with ($\varepsilon_r = 2.0$, $\mu_r = 1.0$). The dipole spacing is $d = 1\,\text{nm}$. The incident wavelength *in vacuo* is $\lambda = 500\,\text{nm}$.

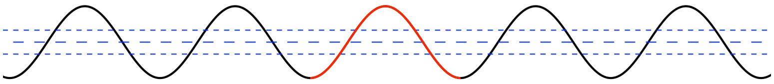

Figure 5.2: Graphical representation of the periodicity of the extinction efficiency as a function of the incidence angle. The calculated case is shown in red (between 0° and 90°, with logical symmetry around 45°, while the dashed blue lines show the mean value together with the standard deviation.

Another case, this time with a relative magnetic permeability μ_r different from one, is shown in Figure 5.3, with $\bar{Q}_{\text{ext}} = 1.08602 \times 10^{-5}$ and $\sigma_s = 4.96905 \times 10^{-11}$. The great similarity between both cases invites us to think that, as already pointed, an estimation of the relative error of the extinction efficiency may be given by ${}^{\delta Q_{\text{ext}}}/_{Q_{\text{ext}}} = 10^{-5}$.

5.1.2 *Convergence tests*

The extinction efficiency for a sphere of radius $R = 2\,\text{nm}$ varying the dipole spacing (and therefore the total number of dipoles) is shown in Figure 5.4. It can be seen that this early version of E-DDA does not converge as well as DDSCAT 7.0.7, despite the great similarities between both calculations (notice the order of magnitude of the efficiencies involved). This may be due to multiple reasons, although the most probable one is the solving method used. While our calculation makes use of a self consistent solving scheme, simply introducing the output as the new input in every iteration, the software by Draine and Flatau [85] utilizes a much more sophisticated solving method based on Fast-Fourier Transformations (FFT) and conjugate gradients, which assures a much quicker and more stable convergence.

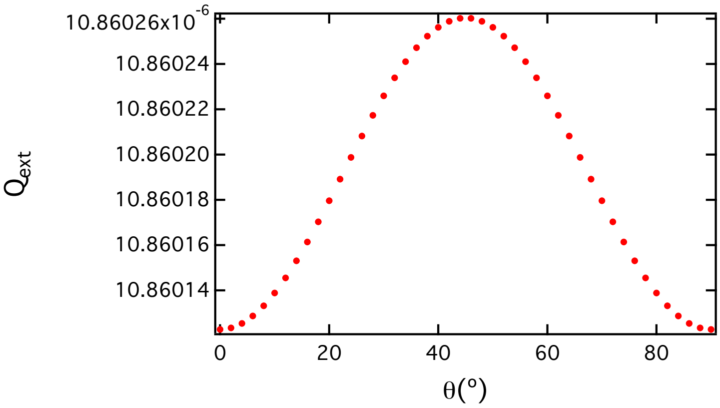

Figure 5.3: Extinction efficiency as a function of the incidence angle for a sphere of radius $R = 6\,\text{nm}$ with ($\varepsilon_r = 2.0$, $\mu_r = 2.0$). The dipole spacing is $d = 1\,\text{nm}$. The incident wavelength *in vacuo* is $\lambda = 500\,\text{nm}$.

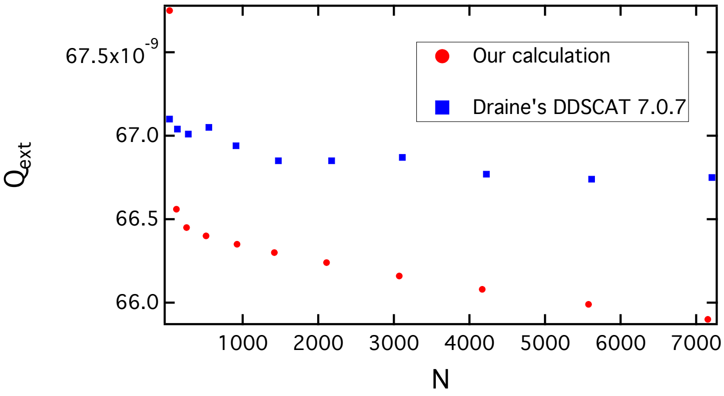

Figure 5.4: Extinction efficiency as a function of the total number of dipoles N for a sphere of radius $R = 2\,\text{nm}$ with ($\varepsilon_r = 2.0$, $\mu_r = 1.0$). The incident wavelength *in vacuo* is $\lambda = 500\,\text{nm}$. Results obtained with DDSCAT are also shown for comparison purposes.

Figure 5.5 shows the same case as before (Figure 5.4) but this time with a relative magnetic permeability μ_r different from 1. Notice again the apparent lack of convergence. This time Draine's software does not allow for a relative magnetic permeability different from 1, so its results cannot be shown. It can be seen how the addition of a magnetic permeability does not significantly modify the convergence, in spite of the increase in complexity in the calculation. The solving method implemented in this early version of E-DDA did not allow for targets discretized with $N > 10000$, that is why results with larger N are not shown.

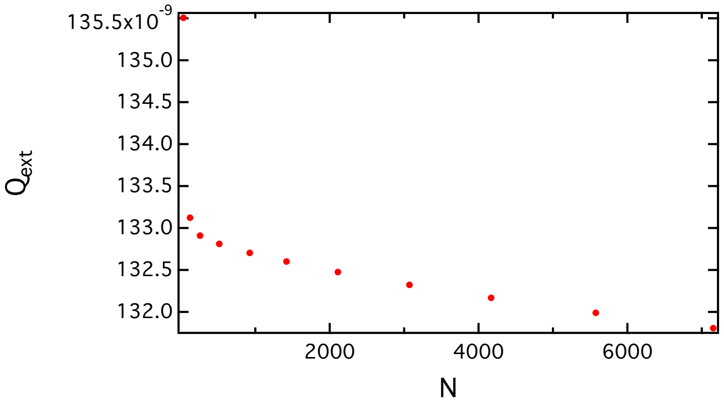

Figure 5.5: Extinction efficiency as a function of the total number of dipoles N for a sphere of radius $R = 2\,\text{nm}$ with ($\varepsilon_r = 2.0$, $\mu_r = 2.0$). The incident wavelength *in vacuo* is $\lambda = 500\,\text{nm}$.

5.2 TESTING THE CODE: NANOSHELLS

To check the reliability of E-DDA, we have performed some calculations on systems that conventional methods can solve. Figure 5.6 shows the extinction, absorption and scattering efficiencies for both a gold sphere of radius $R = 20\,\text{nm}$, and a sphere with a dielectric core (inclusion, $\varepsilon_c = 2$) of radius $R_c = 12\,\text{nm}$ and a metallic shell (gold, optical constants taken from Johnson and Christy [87]), for an external radius $R = 20\,\text{nm}$. Comparison between our code and the well-proved DDSCAT code from Draine and Flatau [82, 85] is also presented, finding a very good agreement in both the spectral shape and the absolute differences for all the efficiencies within the optical range.

5.3 E-DDA ON ANISOTROPIC MEDIA

When the E-DDA is used in the most general case of an anisotropic scatterer with both $\bar{\bar{\varepsilon}}_r$ and $\bar{\bar{\mu}}_r$ tensorial magnitudes, it is possible to find a situation in which we already have a knowledge of the system behavior. Such is the case of particles with directional scattering imposed by their optical constants as, for instance, the null-scattering conditions proposed by Kerker et al. [31]. It will be shown here that these well-known conditions remain valid for anisotropic media. As a reminder, Kerker's null scattering conditions are obtained when the electric and magnetic polarizabilities meet certain stipulations. In particular, when $\bar{\bar{\alpha}} = \bar{\bar{\chi}}$ the backscattering gain equals zero, and when $\bar{\bar{\alpha}} = -\bar{\bar{\chi}}$ the forward scattering is zero. These conditions lead to $\bar{\bar{\varepsilon}}_r = \bar{\bar{\mu}}_r$ for the first case, and $\bar{\bar{\varepsilon}}_r = \left(4\bar{\bar{\mathbf{I}}} - \bar{\bar{\mu}}_r\right)\left(2\bar{\bar{\mu}}_r + \bar{\bar{\mathbf{I}}}\right)^{-1}$ for the latter. However, these relations fail to include the radiative correction [20]. It can be shown that the zero-backward scattering condition re-

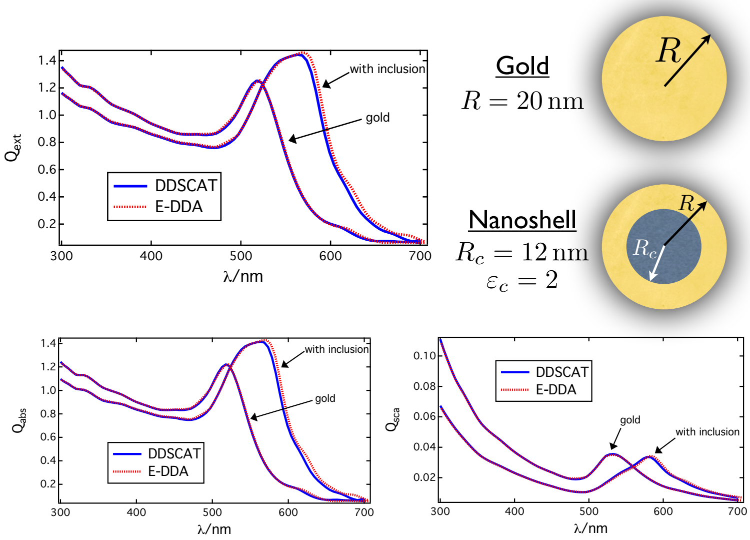

Figure 5.6: Extinction, absorption and scattering efficiencies for both a gold sphere of radius $R = 20\,\text{nm}$, and a sphere with a dielectric core (inclusion, $\varepsilon_c = 2$) of radius $R_c = 12\,\text{nm}$ and a metallic shell (gold), for an external radius $R = 20\,\text{nm}$. Comparison between our code and the well-established DDSCAT code is also provided. The dipole spacing was $d = 4\,\text{nm}$, with $N = 515$.

mains valid, that is, $\bar{\bar{\varepsilon}}_r = \bar{\bar{\mu}}_r$. But, for the zero-forward scattering condition, we obtain the new relation (see Section 3.2):

$$\bar{\bar{\mu}}_r = \left[4\bar{\bar{I}} - \bar{\bar{\varepsilon}}_r - \frac{i(kd)^3}{\pi}(\bar{\bar{\varepsilon}}_r - \bar{\bar{I}})\right]\left[2\bar{\bar{I}} + \bar{\bar{\varepsilon}}_r - \frac{i(kd)^3}{\pi}(\bar{\bar{\varepsilon}}_r - \bar{\bar{I}})\right]^{-1} \tag{5.1}$$

Let us now consider a set of three different permittivity tensors. The first case (isotropic material) is the scalar case:

$$\bar{\bar{\varepsilon}}_{r_1} = \begin{pmatrix} 2.0+0.01i & 0 & 0 \\ 0 & 2.0+0.01i & 0 \\ 0 & 0 & 2.0+0.01i \end{pmatrix} = (2.0+0.01i)\bar{\bar{I}} \tag{5.2}$$

The second case is chosen in the form of a typical magneto-optical material, with an antisymmetric relative electric permittivity tensor $\bar{\bar{\varepsilon}}_{r_2}$ given by (magnetization along z-axis):

$$\bar{\bar{\varepsilon}}_{r_2} = \begin{pmatrix} 2.0+0.01i & 0.3+0.2i & 0 \\ -0.3-0.2i & 2.0+0.01i & 0 \\ 0 & 0 & 2.0+0.01i \end{pmatrix} \tag{5.3}$$

For the third case we propose a symmetric permittivity tensor $\bar{\bar{\varepsilon}}_{r_3}$:

$$\bar{\bar{\varepsilon}}_{r_3} = \begin{pmatrix} 2.0 + 0.01i & 0.3 + 0.2i & 0 \\ 0.3 + 0.2i & 2.0 + 0.01i & 0 \\ 0 & 0 & 2.0 + 0.01i \end{pmatrix} \tag{5.4}$$

For each of these three cases we shall define two values of the relative magnetic permeability tensor in order to fulfill each of the zero scattering conditions (this makes six different materials as a whole). We now consider an sphere of diameter $D = 20\,\text{nm}$ made of those materials, illuminated with a wavelength of $\lambda = 500\,\text{nm}$, obtaining that the zero-forward scattering condition is, for each case:

$$\bar{\bar{\mu}}_{r_1} = (0.4 - 3.6005 \times 10^{-3} i)\bar{\bar{\mathbf{I}}} \tag{5.5}$$

$$\bar{\bar{\mu}}_{r_2} = \begin{pmatrix} 3.9232 \times 10^{-1} - 2.0508 \times 10^{-2} i & -1.0899 \times 10^{-1} - 6.8489 \times 10^{-2} i & 0 \\ 1.0899 \times 10^{-1} + 6.8489 \times 10^{-2} i & 3.9232 \times 10^{-1} - 2.0508 \times 10^{-2} i & 0 \\ 0 & 0 & 0.4 - 3.6005 \times 10^{-3} i \end{pmatrix} \tag{5.6}$$

$$\bar{\bar{\mu}}_{r_3} = \begin{pmatrix} 4.0712 \times 10^{-1} + 1.3870 \times 10^{-2} i & -1.0804 \times 10^{-1} - 7.3802 \times 10^{-2} i & 0 \\ -1.0804 \times 10^{-1} - 7.3802 \times 10^{-2} i & 4.0712 \times 10^{-1} + 1.3870 \times 10^{-2} i & 0 \\ 0 & 0 & 0.4 - 3.6005 \times 10^{-3} i \end{pmatrix} \tag{5.7}$$

and $\bar{\bar{\mu}}_{r_i} = \bar{\bar{\varepsilon}}_{r_i} (i = 1, 2, 3)$ for the zero backward. The scattering patterns in Figure 5.7 show that Kerker's conditions are being satisfied. It is worth noticing that, while the isotropic case can be computed by means of conventional numerical methods (producing a perfect match), the anisotropic ones do not admit such comparison in a feasible way. By using E-DDA, we obtain results that show that the systems behave exactly as expected from the theoretically imposed condition, that is, exhibiting zero-back and zero-forward scattering.

To sum up Chapter 5, we have validated our E-DDA code by first performing both symmetry and convergence tests that allow us to check the self-consistency of our calculation method. We have then compared results for a case where the applicability range overlaps with the one of the well-proved DDSCAT code, which includes inhomogeneities and presence of metallic and dielectric media, finding a very good agreement. We have applied the proposed method to a situation out of reach for current implementations of the DDA, like Kerker's null-scattering (backward and forward) conditions for anisotropic (both electric and magnetic) media. We have verified numerically these conditions in its tensorial form.

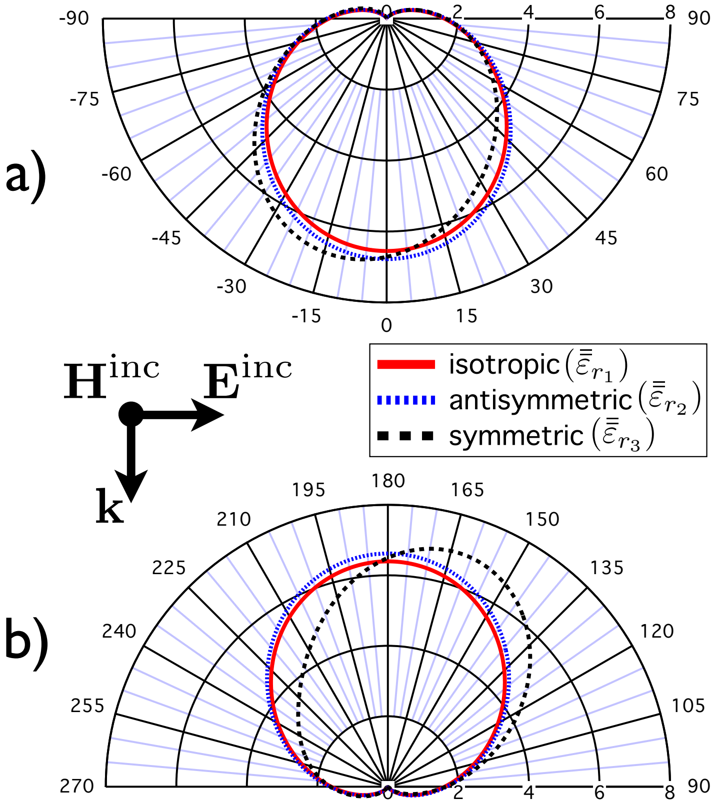

Figure 5.7: a) Zero-backward scattering ($\bar{\bar{\mu}}_r = \bar{\bar{\varepsilon}}_r$). b) Zero-forward scattering. In every case, the dipole spacing was $d = 2\,\text{nm}$, with $N = 515$.

6

E-DDA APPLIED TO MAGNETO-OPTICAL MATERIALS

6.1 INTRODUCTION

Electromagnetic scattering from nanometer-scale particles is currently a topic of great interest, which is being investigated both theoretically and experimentally for the purpose of understanding the underlying physics and investigate novel near- and far-field optical effects [10, 88, 89]. Also, the technological challenge of reducing the scale to work with light has opened new and better possibilities of applications in crucial fields such as those related to health [90–92], optical communications [93], information storing [94] and photonics in general [95–97]. Much of this recent drive has been triggered by the availability of nano-fabrication facilities that allow for the design and realization of nano-scale materials [98]. Also, the development of nanometer-scale optical probes like near-field scanning optical microscopy [99] has been crucial in this respect. The vast majority of recent studies are performed on metal nano-structures and are focused on the effects on the scattered field due to the excitation of resonances from surface or localized plasmons [63, 100–102]. On the other end, the recent interest in magneto-plasmonics, i.e. solid state materials that combine magnetic and plasmonic functionalities, has brought forward numerous studies of the interplay between plasmon excitations and magnetism in nano-sized or nano-scale defined structures [103–109]. However, little attention has been paid to other potentially interesting effects arising from the mutual interplay between magneto-optical activity and light-matter coupling in spatially confined geometries [110–112], which are independent of resonance excitations. At the same time, the exploration of these effects poses fundamental questions in magneto-optics of nano-scale materials and requires new impulses towards experimental [113, 114] and modeling efforts [21, 83, 115].

To address these fundamental issues of magneto-optical scattering from nanometer-scale magnetic structures, we developed a modeling approach that relies on a recently developed finite element computational method, which is an extension of the discrete dipole approximation [83]. The method allows for the calculation of the optical and magneto-optical scattering from non-spherical nano-structures. This aspect is particularly relevant as the majority of experiments are carried out using flat, non-spherical nanometer-scale objects [111, 116]. In addition, and since the far-field scattering is measured from a collection of many nano-objects, we have extended the calculations to the experimentally relevant case of an ordered array of non-interacting identical nano-structures.

In order to separate optical and magneto-optical effects that are arising from the nanometer-scale confinement, we have also compared our calculations to a reference case that neglects the effects of the lateral confinement on the induced dipoles distribution. Hereby, we define a fictitious (dummy) laterally confined structure made of identical dipoles behaving as if they were part of an infinite film, viz., modeled as a single layer of dipoles under the assumption of translational invariance of the induced dipole moment. This reference case, that has the same level of discretization as well as the same local material properties and approximation assumptions, is what we later call our infinite layer (IL) approach.

We applied these two approaches to predict the optical and magneto-optical responses in the near- and far-field for cobalt disks of sizes from $200-1000\,\mathrm{nm}$, illuminated with a wavelength of $\lambda = 632.8\,\mathrm{nm}$ under normal incidence. The nano-structures are magnetized in the disk plane and the magneto-optical response is calculated for the so called transverse magneto-optical Kerr effect (T-MOKE) configuration, in which the electric field of the linearly polarized incoming light is parallel to the scattering plane, while the magnetization of the disk is perpendicular to it.

Our results show that although the nano-confinement effects appear in the near-field optical and magneto-optical responses of all disks diameters, far-field effects show up only for disks that have a diameter smaller than the wavelength of the incoming light *in vacuo* λ. More importantly, we observe that the optical and magneto-optical contributions to the far-field intensity scale in an almost identical fashion, so that the normalized magneto-optical response, which is the experimentally relevant quantity, is only very weakly affected by the confinement even in the case of sub-wavelength sized disks.

The work is organized as follows: in Section 6.2, the theoretical background, on which our numerical method is based, is presented. In Section 6.3, the scattering geometry together with the sample magneto-optical properties are shown. Section 6.4 is devoted to the presentation and discussion of the main results obtained from our numerical model. Finally, in Section 9.2, the main conclusions of this research are summarized.

6.2 THEORY

6.2.1 *Finite particle (FP) approach*

Our approach for modeling the optical and magneto-optical responses of nano-scale objects utilizes the recently developed E-DDA methodology [83], described in Section 4.3[1]. Let us assume that the magneto-optical material is magnetized along the z-direction, then the relative dielectric tensor $\bar{\bar{\varepsilon}}_r$ is given by [117]:

$$\bar{\bar{\varepsilon}}_r = \begin{pmatrix} \varepsilon_d & -i\varepsilon_d Q & 0 \\ i\varepsilon_d Q & \varepsilon_d & 0 \\ 0 & 0 & \varepsilon_d \end{pmatrix} \tag{6.1}$$

, where Q is the magneto-optical Voigt parameter accounting for the coupling between the electric field and the magnetization. It can be shown that the electric polarizability tensor (given by Equation (3.12)), neglecting second order terms, $O(\varepsilon_{off}^2)$, has the following form:

$$\bar{\bar{\alpha}}_j = \begin{pmatrix} \alpha_d & \alpha_{off} & 0 \\ -\alpha_{off} & \alpha_d & 0 \\ 0 & 0 & \alpha_d \end{pmatrix} \tag{6.2}$$

, where α_d and α_{off} are the diagonal and the off-diagonal elements of the electric polarizability tensor respectively. Direct application of the E-DDA to the actual disk shape structure will provide the solution that we refer to as Finite Particle (FP) approach.

6.2.2 *Infinite layer (IL) approach*

For the purpose of evidencing finite lateral size effects in our calculations, we implemented a numerical approach to the problem having the same level of local properties representation and numerical approximations but which neglects the effects of the lateral confinement on the induced dipoles distribution.

In the IL approach, the dipole-dipole interactions are assumed to be the same as for an infinite film at every point of the structure, so that any particle can be represented by placing non-interacting dipoles on a properly shaped grid, whose polarizability tensor have been renormalized to include the infinite film interactions exactly. In the derivation of this approach, each electric dipole interacts with an infinite number of surrounding electric dipoles, each of which having an electric polarizability $\bar{\bar{\alpha}}_j$ given by Equation (3.12), as shown in Figure 6.1.

---

[1] In the E-DDA, both the electric and magnetic responses of the material are taken into account by considering the excitation of both an oscillating electric and magnetic dipole. In addition, both the relative electric permittivity, $\bar{\bar{\varepsilon}}_r$, and the relative magnetic permeability, $\bar{\bar{\mu}}_r$, of the material, are 2nd order (or rank) tensors, although in order to treat magnetic materials in the optical range, we can consider $\bar{\bar{\mu}}_r = \bar{\bar{\mathbf{I}}}$.

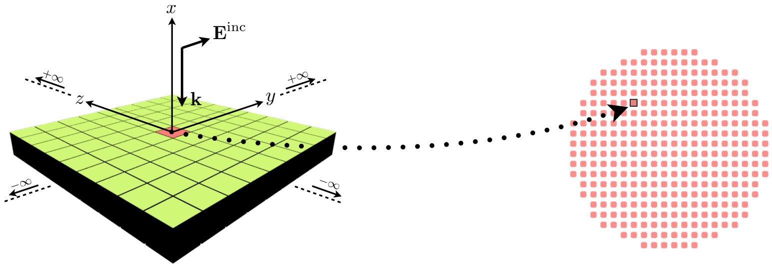

Figure 6.1: Infinite layer approach. Every dipole interacts with all the other dipoles. Subsequently, this dipole is inserted in each cell of the discretization mesh to model any arbitrary planar shape (no further interaction is considered).

The dipole moment acquired by each of this electric dipoles is given by:

$$\mathbf{p}_j = \varepsilon_0 \bar{\bar{\alpha}}_j \left(\mathbf{E}_j^{\mathrm{inc}} + \sum_{k \neq j} \bar{\bar{\mathbf{A}}}_{jk} \mathbf{p}_k \right) \tag{6.3}$$

To express this dipole moment in terms of an effective electric polarizability that incorporates all interactions, we define:

$$\mathbf{p}_j = \varepsilon_0 \bar{\bar{\alpha}}_{\mathrm{eff}} \mathbf{E}_j^{\mathrm{inc}} \tag{6.4}$$

For normal incidence radiation, the exciting field as well as the lateral film structure are translationally invariant, so that, assuming all the dipoles have the same electric polarizability tensor $\bar{\bar{\alpha}}_j \equiv \bar{\bar{\alpha}}$, the resulting polarization pattern also has translational invariance and all electric dipoles within the film acquire the same dipole moment, i.e. $\mathbf{p}_j = \mathbf{p}_k = \mathbf{p}_{\mathrm{IL}}$. Then:

$$\left(\bar{\bar{\mathbf{I}}} - \varepsilon_0 \bar{\bar{\alpha}} \sum_{k \neq j} \bar{\bar{\mathbf{A}}}_{jk} \right) \mathbf{p}_{\mathrm{IL}} = \varepsilon_0 \bar{\bar{\alpha}} \mathbf{E}^{\mathrm{inc}} \tag{6.5}$$

$$\mathbf{p}_{\mathrm{IL}} = \varepsilon_0 \underbrace{\left(\bar{\bar{\mathbf{I}}} - \varepsilon_0 \bar{\bar{\alpha}} \sum_{k \neq j} \bar{\bar{\mathbf{A}}}_{jk} \right)^{-1} \bar{\bar{\alpha}}}_{\bar{\bar{\alpha}}_{\mathrm{eff}}} \mathbf{E}^{\mathrm{inc}} \tag{6.6}$$

leading to:

$$\boxed{\bar{\bar{\alpha}}_{\mathrm{eff}} = \left(\bar{\bar{\mathbf{I}}} - \varepsilon_0 \bar{\bar{\alpha}} \sum_{k \neq j} \bar{\bar{\mathbf{A}}}_{jk} \right)^{-1} \bar{\bar{\alpha}}} \tag{6.7}$$

For the calculation of the infinite sum in Equation (6.7), a suitable truncation criterion must be established by studying its convergence. For this purpose, we analyzed the "order" $^1/_2 N^{1/2}$ (N being the total number of dipoles) dependence of the numerical values. Here we found that calculation of up to an order of 1000, corresponding to 4,000,000 dipoles, allowed for a very accurate extraction of the effective polarizability tensor.

Once converged, the transfer function tensor sum $\sum_{k\neq j} \bar{\bar{\mathbf{A}}}_{jk}$ becomes:

$$\sum_{k\neq j} \bar{\bar{\mathbf{A}}}_{jk} = \begin{pmatrix} s_{xx} & 0 & 0 \\ 0 & s_{yy} & 0 \\ 0 & 0 & s_{zz} \end{pmatrix} \tag{6.8}$$

, with:

$$\begin{aligned} s_{xx} &= -6.50 \pm 0.04 \times 10^{35} + i\,0 \pm 4 \times 10^{33}\ [\mathrm{F}^{-1}\mathrm{m}^{-2}] \\ s_{yy} &= 3.24 \pm 0.02 \times 10^{35} + i\,2.2 \pm 0.2 \times 10^{34}\ [\mathrm{F}^{-1}\mathrm{m}^{-2}] \\ s_{zz} &= s_{yy} \end{aligned}$$

Please notice that these values were obtained for a single layer of cobalt, discretized with a dipole spacing $d = 5\,\mathrm{nm}$, and illuminated with a plane wave of $\lambda = 632.8\,\mathrm{nm}$.

6.3 SAMPLE GEOMETRY AND MATERIAL PARAMETERS

In order to obtain the optical and magneto-optical responses of disk-shaped objects, we have used material parameters of cobalt, as given in Ref. [118] with $\varepsilon_r = -12.6 + 22.88i$ and $Q = 0.034 + 0.014i$, for $\lambda = 632.8\,\mathrm{nm}$. All calculations are performed twice: first as fully self-consistent FP particle calculations, and then for comparison purpose within the framework of the IL approach. Figure 6.2 shows the specific MOKE configuration used here, with a set of disks arranged on a two-dimensional square lattice of period a. The scattering properties of the complete lattice will be considered specifically in Section 6.4.2.2. The disks are supposed to be embedded in vacuum, and illuminated by a monochromatic incident beam under normal incidence. The incident electric field $\mathbf{E}_j^{\mathrm{inc}}$ is linearly polarized along the y-direction and the sample magnetization is perpendicular to the incident electric field, so that the wave vector $\mathbf{k}$, the incident electric field $\mathbf{E}_j^{\mathrm{inc}}$ and the magnetization $\mathbf{M}$ are all orthogonal to each other. This arrangement corresponds to the T-MOKE geometry where changes in the sample magnetization lead to changes in the intensity of the scattered field, leaving its polarization state unchanged [117]. Applying the above values in Equation (6.1), the relative dielectric tensor becomes (assuming that the external magnetic field is large enough to reach magnetization saturation along the z-axis of the sample):

$$\bar{\bar{\varepsilon}}_r = \begin{pmatrix} \varepsilon_d & \pm\varepsilon_{off} & 0 \\ \mp\varepsilon_{off} & \varepsilon_d & 0 \\ 0 & 0 & \varepsilon_d \end{pmatrix} \tag{6.9}$$

, where $\varepsilon_d = -12.6 + 22.88i$ and $\varepsilon_{off} = 0.60152 + 0.74872i$. Notice as well that, according to the T-MOKE configuration shown in Figure 6.2 (magnetization **M** in z-direction), only the diagonal and the xy-elements of the dielectric tensor are different from zero, with their sign depending on the direction of the magnetization along the z-axis.

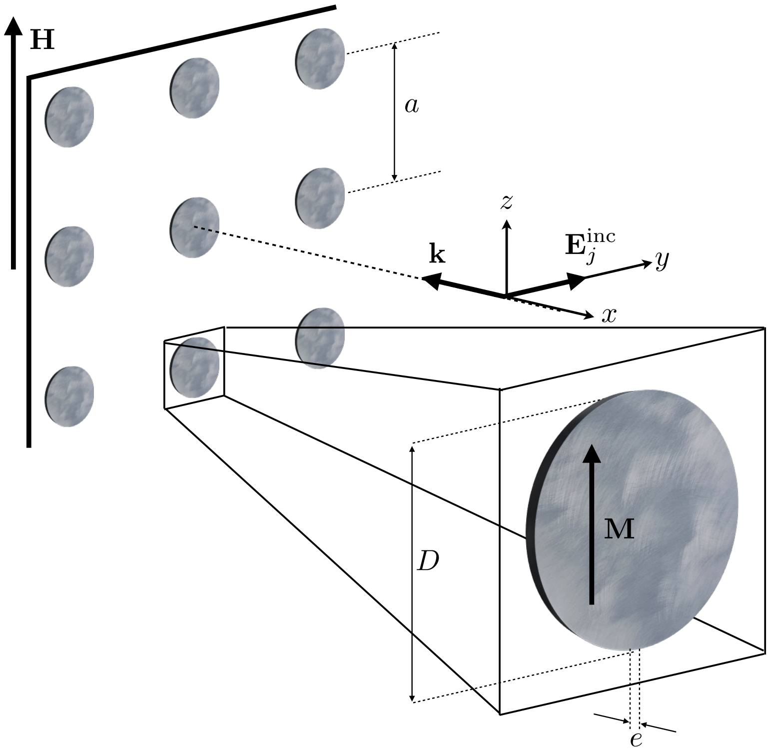

Figure 6.2: T-MOKE configuration tipically used in an experimental setup, with an array of disks of thickness e with constant lattice period a along both surface plane dimensions. The incoming light wavevector, with $\lambda = 632.8$ nm, is in the -x-direction, the incident electric field $\mathbf{E}_j^{inc}$ is linearly polarized along the y-direction, and the magnetization **M** is perpendicular to the chosen scattering plane (considering X-Y plane).

In our numerical calculations, different diameters for the disks have been considered, ranging from $D = 200$ nm to $D = 1000$ nm, with all of them having a thickness of $e = 5$ nm. The lattice period, a, has been chosen large enough, ranging from 700 nm to 15 µm, so that interactions between the disks are very weak and can be neglected. Thus, we can simplify our simulations to calculations on a single disk only and, with these results, predict the diffracting behavior of the entire array under uniform illumination. The single disk simulations have been performed by using the E-DDA code, with a dipole spacing of $d = 5\,\text{nm}$. Correspondingly, we only consider a single layer of electric dipoles for cubic cells of volume $\nu_j = d^3$. We used a grid with $d = 5\,\text{nm}$ that is much finer than the widely used one [82] based on $|n|kd \lesssim 1$, which would correspond to $d < 20\,\text{nm}$[2]. Calculations using a finer grid of $d = 2.5\,\text{nm}$ produced no significant changes in the results.

In the single layer calculation, all dipoles are contained in a planar structure, so that in the absence of magneto-optical effects, only the y and z components of the local polarization are different from zero. This allows us to easily relate the out of plane (x) component of $\mathbf{p}_j$ with the MO contribution.

It is important to notice that the general observations made here still hold if one were to replace the single layer calculation with a multilayer calculation, but it is not as straightforward to isolate the magneto-optically induced polarization pattern in this case.

The T-MOKE is usually characterized by the parameter ΔI, which here we defined as the absolute change in the intensity of the light scattered by a medium when the magnetization $\mathbf{M}$ of the medium is reversed:

$$\Delta I = |I(\mathbf{M}) - I(-\mathbf{M})| \tag{6.10}$$

, where I is the scattered light intensity.

6.4 RESULTS AND DISCUSSION

6.4.1 *Dipole moment distributions*

A comparison of the resulting polarization pattern is summarized in Figure 6.3, where the spatial distributions of the primary optical (y-component) and MO (x-component) dipole moment are shown for a set of disks, ranging from $D = 200\,\text{nm}$ to $D = 1000\,\text{nm}$, calculated with the FP approach and normalized by the dipole moment obtained with the IL reference method, i.e. (on each cell j):

$$|p_y| = \frac{|p_y|_{FP}}{|p_y|_{IL}} \quad \text{and} \quad |p_x| = \frac{|p_x|_{FP}}{|p_x|_{IL}} \tag{6.11}$$

The first thing to notice when looking at Figure 6.3 is that the distributions of $|p_y|$ and $|p_x|$ are not homogeneous and show noticeable departures from 1, i.e. there are important confinement modifications to both the primary optical (y) and the MO (x) responses of the disks.

---

[2] For absorbing materials such as metals, the original criterion might not be sufficient, as the skin depth is far smaller than the wavelength.

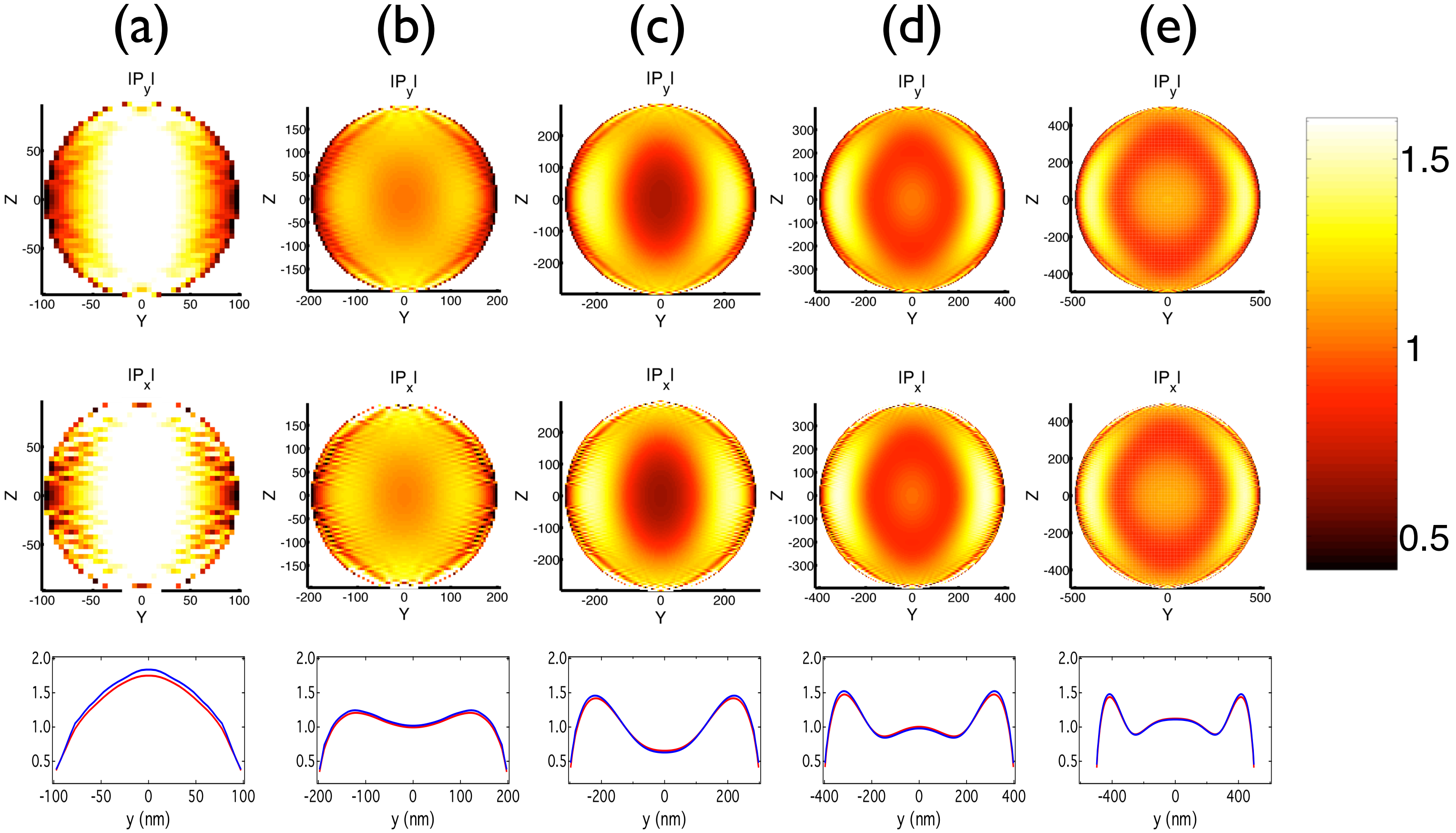

Figure 6.3: Absolute value of the primary optical (y) and MO (x) components of the induced dipole moment for several sizes normalized to the IL calculation. From left to right, each column corresponds to one disk size, (a) D = 200 nm, (b) D = 400 nm, (c) D = 600 nm, (d) D = 800 nm and (e) D = 1000 nm. The color scale is the same for all maps. The third row shows line profiles along the y-direction ($z = 0$) for both the primary optical (red lines) and the magneto-optical (blue lines) components.

The second important aspect that is visualized by the polarization pattern in Figure 6.3 is the fact that the MO response pattern is very similar, if not outright indistinguishable from the lateral p_y-structure, indicating that the magneto-optical effect is a small perturbation of the optical response and thus mimics its behavior. These results are in agreement with recent results obtained by other authors [119].

In general, a confined geometry results in the appearance of different oscillation modes in the dipole amplitude spatial distribution, coming from the finite size (and shape) self-interaction. This is clearly seen in the third row of Figure 6.3, where line profiles along the y-direction ($z = 0$) are shown for both the primary optical (red lines) and the magneto-optical (blue lines) component. These geometry induced interactions do not only modify the lateral distribution of the dipole pattern, but can also result in collective effects, as hinted by the overall enhancement found in the smallest disk size shown, $D = 200\,\text{nm}$, Figure 6.3a. Indeed, the $D = 200\,\text{nm}$ presents the most important deviation from the IL approach, with high values of the dipole moment even in the central region of the disk.

The case $D = 400\,\text{nm}$ (Figure 6.3b) already starts to show the appearance of a new central minimum, as well as two regions with high values of dipole moment. This is clearly seen in the case $D = 600\,\text{nm}$ (see Figure 6.3c). As D increases, Figures 6.3d and e, the oscillation of the spatial distribution of the dipole moment amplitude appears, resulting in new minima and maxima that nucleate in the center of the disk and expand (and squash together) towards the edges.

Both in the optical and the MO components, the phase distributions are all very uniform, being the dipole moments inside the particle almost in phase with the IL reference dipole, as shown in Figure 6.4. Again the MO component follows the optical response in all cases.

Following the simple arguments presented when discussing the case of two interacting electric dipoles, we can understand two important features of the maps of the primary optical response, i.e. the y-component, shown in the first row of Figure 6.3. For all sizes, it is found that along the y-direction, there is a decrease near the boundaries of the disk. This can be explained due to the absence of neighboring electric dipoles outside the particle. The missing dipoles would be supporting those at the boundary, the same way neighboring dipoles support each other in the interior of the disk due to their alignment (see Figure 2.3a). Thus the induced dipole moment at the boundary is smaller than inside the disk or in the case of the IL reference calculation, for which the neighbors extend to infinity. In the case of the MO (x) response (see Fig 6.3, second row), it can be seen that it follows the p_y even in the boundary region.

In order to show the global behavior of the induced dipole moment in the disks as a function of both the MO constant Q and the size, we have calculated the averaged dipole moment inside the disks. In

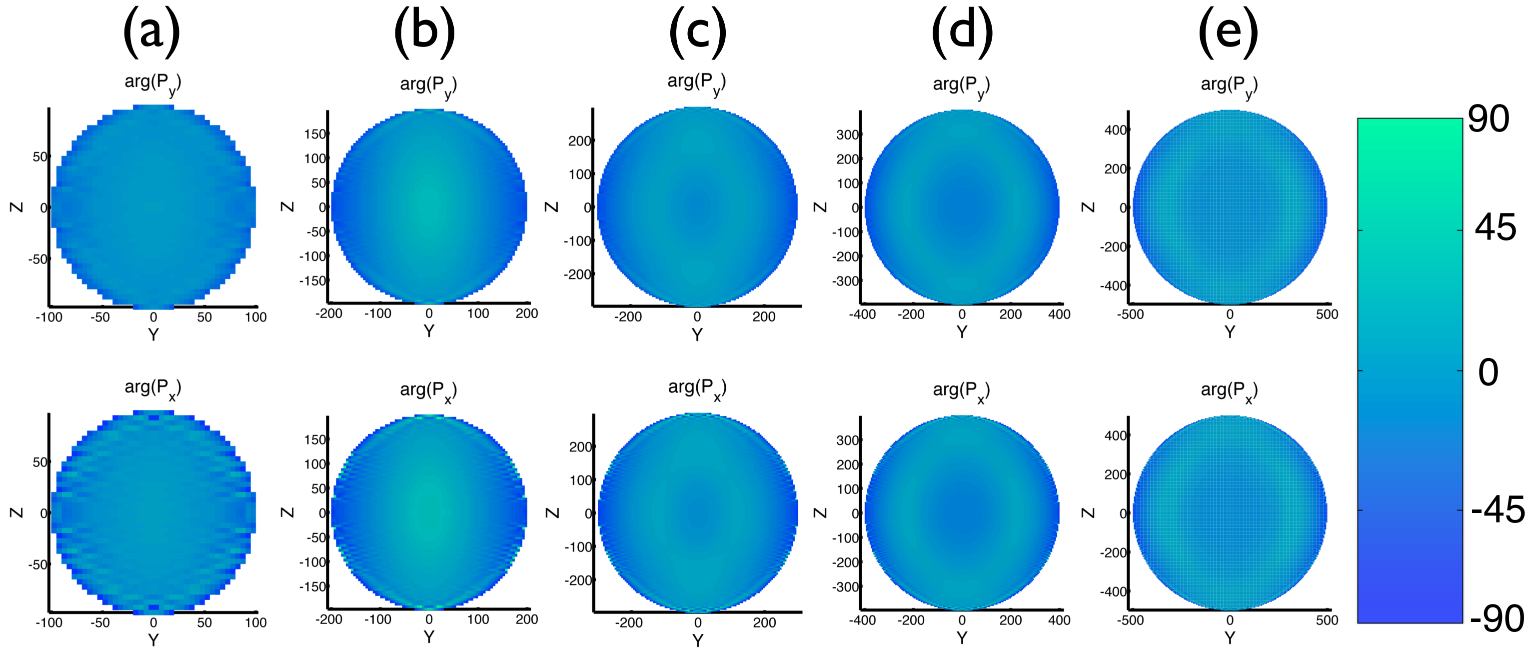

Figure 6.4: Phase of the primary optical (y) and MO (x) components of the induced dipole moment for several sizes relative to the IL calculation. From left to right, each column corresponds to one disk size, (a) D = 200 nm, (b) D = 400 nm, (c) D = 600 nm, (d) D = 800 nm and (e) D = 1000 nm. The color scale is the same for all maps.

Figure 6.5, all results correspond to the spatial average over the disk, normalized to the IL results.

$$|\langle p_y \rangle| = \frac{|\langle p_y \rangle|_{FP}}{|p_y|_{IL}} \quad \text{and} \quad |\langle p_x \rangle| = \frac{|\langle p_x \rangle|_{FP}}{|p_x|_{IL}} \tag{6.12}$$

Figure 6.5 shows the absolute value of the averaged primary optical (y) and MO (x) components of the induced dipole moment normalized to IL results, as a function of the disk diameter D.

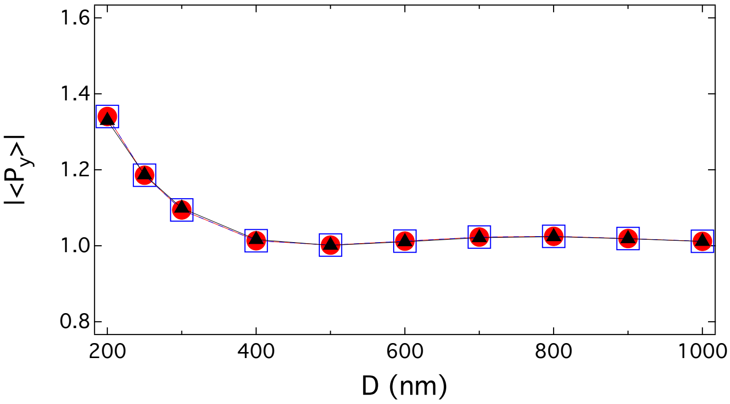

(a) Primary optical response.

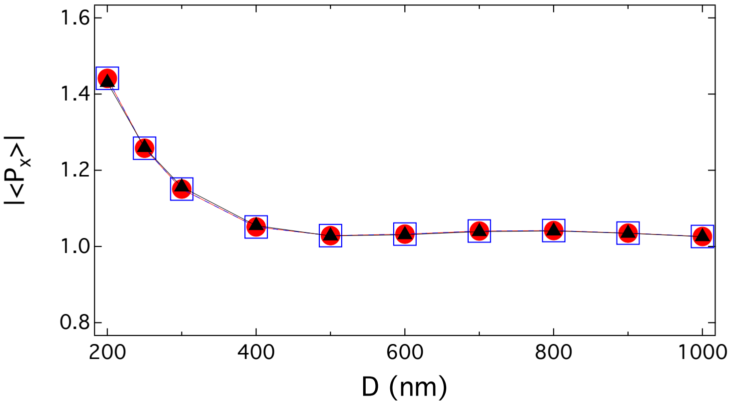

(b) Magneto-optical response.

Figure 6.5: Absolute value of the averaged (a) primary optical (y) and (b) MO (x) components of the induced dipole moment for three different values of the MO constant (full red circles for Q, blue squares for $Q/10$ and black triangles for $Q \cdot 10$), as a function of the disk diameter D.

Obviously, the averaged dipole moment in the FP calculation tends to the IL when the size of the disk is increased, and, therefore, the average of the relative amounts tends to 1, as observed in Figures 6.5a and 6.5b. As we decrease the disk diameter, the average dipole moment grows, according to what we had already discussed in relation to the case of $D = 200\,\text{nm}$ disk and its induced polarization distribution (Figure 6.3a). Again, we can see how the MO component enhancement resembles the optical one, although they are not fully identical (one can see quantitatively that the overall p_x enhancement is a bit larger than the p_y enhancement for small disks, $D \leqslant 400\,\mathrm{nm}$). These results indicate that we are in the small perturbation regime of magneto-optics. In order to corroborate this, we have performed calculations varying the strength of the magneto-optical coupling Q, either dividing it or multiplying it by 10, which is also shown in Figure 6.5 (blue squares and black triangles respectively).

It is clearly seen from the results in Figure 6.5 that, if we make the MO coupling constant Q ten times either smaller or larger, the results normalized to a corresponding IL calculation are completely preserved. This confirms that we are in the linear perturbation regime[119], as anticipated by the close similarity of the x and y patterns in Figure 6.3. It is important to keep in mind that, of course, the magneto-optical effect is changed with Q, but this is normalized out by the IL-normalization. Thus, Q, $Q/10$ and $Q \cdot 10$ are perfectly linear in the MO-induced effects. This point will be addressed in further detail in Section 9.2.

Figure 6.6 shows the phase of the averaged primary optical (y) and MO (x) components of the induced dipole moment relative to the phase of the IL dipole, as a function of the disk diameter D. Again, we can see how the MO component enhancement resembles the optical one.

Once more, the phase of the averaged dipole moment in the FP calculation tends to the IL when the size of the disk is increased, and, therefore, the average of the relative amounts tends to 0, as observed in Figures 6.6a and 6.6b. The interesting feature of these curves lies in how, as we decrease the disk diameter, the phase of the average dipole moment tends to the phase of the single dipole. Assuming the T-MOKE geometry illustrated in Figure 6.2 and using Equations (2.11) and (6.2), it may be shown that the induced dipole moment of a single dipole is given by (assuming $\varepsilon_m = 1$):

$$\mathbf{p}^{\text{single}} = \varepsilon_0 E_0 \begin{pmatrix} \alpha_{\text{off}} \\ \alpha_d \\ 0 \end{pmatrix} \tag{6.13}$$

, where E_0 is the amplitude of the incident electric field. The phase of the optical and magneto-optical components of the single dipole are thus given by:

$$\arg(p_y^{\text{single}}) = \arg(\alpha_d) \tag{6.14}$$

$$\arg(p_x^{\text{single}}) = \arg(\alpha_{\text{off}}) \tag{6.15}$$

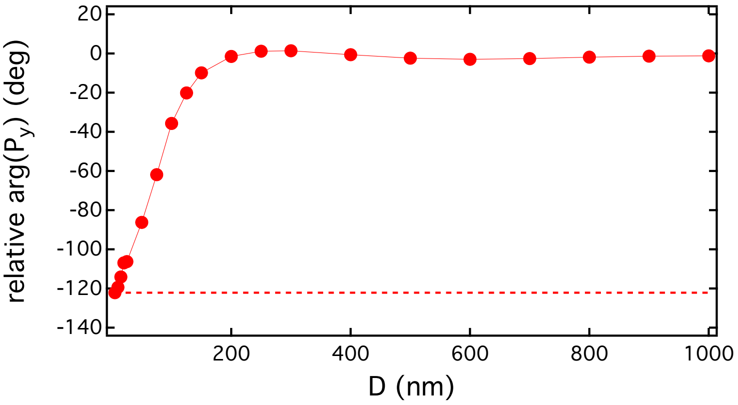

(a) Primary optical response.

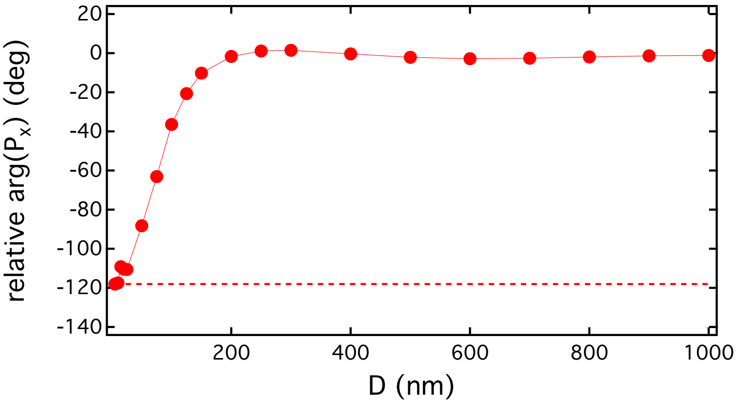

(b) Magneto-optical response.

Figure 6.6: Phase of the averaged (a) primary optical (y) and (b) MO (x) components of the induced dipole moment relative to the phase of the IL dipole, as a function of the disk diameter D. The dashed line represents the single dipole limit, as given in Equations (6.14) and (6.15).

6.4.2 *Far-field*

Experimental measurements of MO effects rely primarily on far-field observation of the scattering changes induced by the presence of a net magnetization. In this section we first calculate and discuss the properties of single disks to achieve a good understanding of their general response. Then, we derive and discuss the magneto-optical response of an array of disks, since experiments make use of arrays.

6.4.2.1 *Single disks*

Figure 6.7 shows the far-field patterns of scattered intensity I and the MO signal ΔI calculated in the X-Y plane, which is the relevant plane for T-MOKE. The IL reference calculation is also shown, in order to compare both approaches and illustrate the confinements effects.

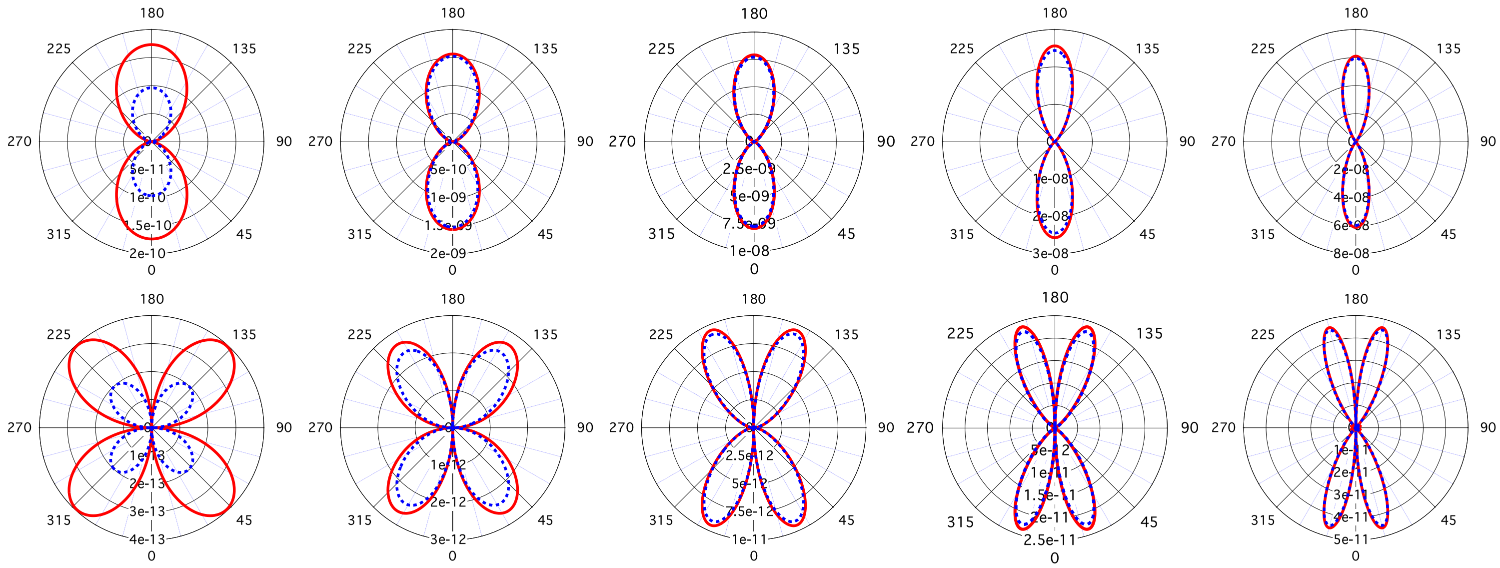

Figure 6.7: Polar plots of the far-field scattered intensity (first row) and ΔI (second row) patterns for several sizes for both the FP and the IL approaches. From left to right, each column corresponds to one disk size, ranging from D = 200 nm, D = 400 nm, D = 600 nm, D = 800 nm and D = 1000 nm. Solid (red) and dashed (blue) lines correspond to the FP and IL approaches respectively. The ΔI patterns are obtained by computing the difference in scattered intensity under magnetization reversal. Notice that 0° and 180° are the backward and forward directions respectively, while the incident electric field oscillates in the $90^\circ - 270^\circ$ direction.

According to the previously discussed findings on the optical and MO dipole distributions, the far-field scattered intensity patterns converge to those obtained with the IL approach (see first row of plots in Figure 6.7), as the disk diameter is increased. All disks show mostly dipolar behavior, i.e. a two lobes scattering pattern with almost no scattered intensity at 90° and 270° (direction of oscillation of the incident electric field). In the case of small disks ($D < \lambda$), a size-dependent enhancement of the scattering intensity is observed. Moreover, scattering from large disks tends to be more directional, around the forward and backward directions, as should be expected for particles of radius larger than the wavelength. The case $D = 200\,\text{nm}$ clearly shows the biggest difference between FP and IL in both I and ΔI, in accordance to results shown in Figure 6.3, indicating that phase changes inside the particle are minimal.

The ΔI patterns (second row in Figure 6.7) show values about three orders of magnitude smaller than the scattered intensity I patterns, being this ratio consistent with the relative magnitude between the MO and optical effects in a material such as Co. As in the case of the I patterns, the ΔI patterns also converge to those obtained with the IL reference method upon increasing the disk diameter. In the forward and backward directions (transmission and reflection respectively), ΔI is zero, since at those directions, the MO response produces *only* a second order scattering effect (see Eq. (3) in Ref. [**?**]), that is insensitive to the sign of $\mathbf{M}$ and thus it does not show up in a difference measurement based upon magnetization reversal, such as ΔI. Along the 90° and 270° direction, the scattered intensity coming from dipoles oscillating along the x-direction is maximum, although insensitive too to the direction of magnetization, therefore producing a deep minimum of ΔI along this axis. The characteristic four-lobe shape of these patterns arises as a consequence of those minima. Of course the curve shape and the direction of the maxima depend on both the relative phase of the radiation coming from the optical and magneto-optical dipoles as well as on the different optical paths, so that they cause an intensity change that depends strongly on the radiation direction.

The normalized MO signal, $\Delta I/I$, the so-called figure of merit of T-MOKE, remains nearly constant, regardless of the disk size in the entire range investigated here, and it is strongest around the 90° and 270° directions, because the total scattered intensity into those directions is almost zero.

6.4.2.2 *Disks lattice*

The computed results shown so far correspond to isolated cobalt disks. However, and in order to compare the computed results with those of real experiments [103], we have implemented a two-dimensional array of disks in our calculation, as shown in Figure 6.2. Experimentally, the MO scattering behavior of a single nano-disk cannot be accurately obtained. However, an ordered array, while preserving all the conditions assumed for each individual scatterer, allows for a more efficient measurement of the scattering, not only for the signal increase produced by the large number of objects, but also for its constructive interference effect. The diffracted spots allow for sampling the scattering pattern at different angles simultaneously, while maintaining the very simple normal incidence geometry, where measurements in reflection are not useful because no T-MOKE effect can be expected in such direction.

From the MO response corresponding to single disks, as obtained with the FP calculation, the far-field scattered intensity is computed along the diffraction directions, neglecting any optical interaction between different disks in the array. The lattice equation at normal incidence for horizontal observations, i.e. scattering in the X-Y plane containing both the surface normal and the incident electric field, is:

$$m\lambda = a \sin\varphi \tag{6.16}$$

, where m is the horizontal diffraction order, λ the incoming light wavelength (*in vacuo*), a the lattice period and φ the horizontal diffraction angle, measured with respect to the lattice normal direction. From Eq. (6.16), one can easily obtain the angular positions at which we must sample the scattered intensity patterns (Figure 6.7), given by $\varphi = \arcsin\left(\frac{m\lambda}{a}\right)$.

Figure 6.8a shows the normalized MO signal $\Delta I/I$ for the case $D = 200\,\text{nm}$, as a function of the lattice parameter, a, and for several diffraction orders from $m = 1$ to $m = 5$. For each value of a, the MO signal increases with the order. More precisely, Figure 6.8b shows that $\Delta I/I$ vs m behavior is due to its dependence on the diffraction angle φ. The increase in the T-MOKE signal with the diffraction angle is primarily a direct consequence of the drop in intensity I, although there is also an increase in the MO signal ΔI, simply due to the increase of the diffraction angle φ, as can be seen in Figure 6.7, first column second row.

Using this representation, the $\Delta I/I$ for all the diffracted beams lie on top of each other, with the starting angle depending on the diffraction order. In Figure 6.8b, $\Delta I/I(\varphi)$ computed using the IL approach is also shown, with an almost perfect match between $\Delta I/I(\varphi)$ computed using the FP approach. We chose the case $D = 200\,\text{nm}$ since it presents substantial deviations from the IL approach, and therefore allows us to confirm very visibly that the geometric confinement does not substantially affect the far-field results in terms of the magneto-optically induced relative intensity change, which is the conventional experimental observable. The results for all other sizes look nearly identical, i.e. show almost exactly the expected behavior that one would derive from the IL approximation for $\Delta I/I$.

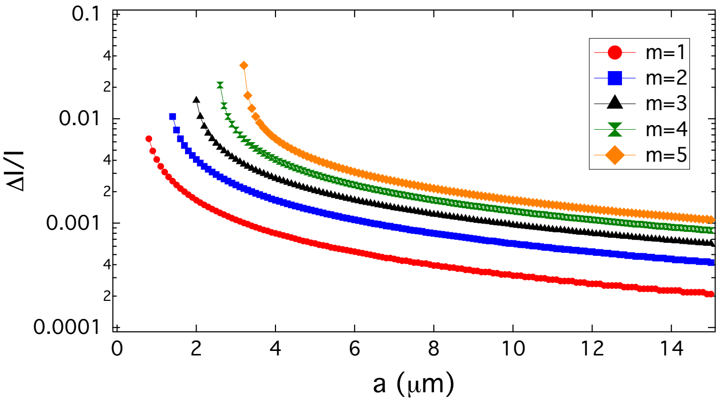

(a) $^{\Delta I}/_{I}$ vs. lattice period a.

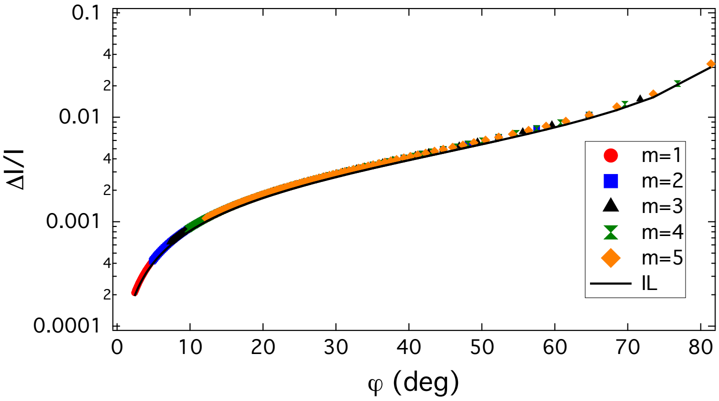

(b) $^{\Delta I}/_{I}$ vs. diffraction angle φ.

Figure 6.8: Normalized MO signal $^{\Delta I}/_{I}$ for several horizontal diffraction orders m for $D = 200\,\text{nm}$, with $\lambda = 632.8\,\text{nm}$.

The gap between neighboring disks, given as $g = a - D$, imposes a minimum for the physically meaningful lattice period corresponding to $g = 0$, i.e. $a_{\text{min}} = D$. However, in order to avoid the near-field optical interactions between the disks, which will complicate the issue and is beyond the scope of this work, it is a good experimental strategy to use values that are substantially larger than a_{min}, also because this would make more diffraction orders available, i.e. more values of φ accessible, although there should be enough magnetic material in the unit cell in order to keep I and ΔI above the noise level. These considerations are among those to be taken account, when it comes to the design of disk lattices to be used in experiments.

6.5 CONCLUSIONS

The main conclusion one can draw from the presented results is the fact that the experimentally accessible $^{\Delta I}/_{I}$-ratio seems virtually unaffected by the geometric confinement of the disks, despite the remarkable size-induced differences that are found in the dipole moment distributions especially for sub-wavelength disks. We have shown that the insensitivity of the $^{\Delta I}/_{I}$-ratio to lateral confinement is a consequence of the close similarity of the optical and magneto-optical polarization patterns, irrespective of disk size, and of the fact that their contributions to the far-field intensity scale nearly in the same way.

To discuss this aspect further, we make the following argument of how the magneto-optical response primarily originates. E_x is the result of the MO-effect only because it does not exist in the case without MO-coupling. Therefore E_x is only caused by the p_x from neighboring dipoles: $E_x = s_{xx} p_x$ (see Equation (6.8)). Furthermore, the entire dipole p_x is a small correction being driven by E_y. Consequently, as a first approximation we can use E_y from the MO-free system as the leading contribution, or equivalently neglect the MO term, $\alpha_{off} E_x$, for the calculation of p_y. Thus, we approximate $p_y \approx P_{y_{scalar}} = \varepsilon_0 \alpha_d E y$, where $P_{y_{scalar}}$ is the optical component coming from a MO-effect free, purely scalar calculation without off-diagonal elements in the dielectric tensor, so that:

$$p_x \approx P_{x_{scalar}} = \varepsilon_0 \left(\alpha_d s_{xx} p_x + \frac{\alpha_{off}}{\varepsilon_0 \alpha_d} P_{y_{scalar}} \right) \tag{6.17}$$

$$P_{x_{scalar}} = \frac{1}{1 - \varepsilon_0 \alpha_d s_{xx}} \frac{\alpha_{off}}{\alpha_d} P_{y_{scalar}} \tag{6.18}$$

If we now have a look at Eq. (6.7) from the Appendix, it can be shown that, neglecting second order MO-terms, i.e. $O\left(\alpha_{off}^2\right)$ terms:

$$\frac{1}{1 - \varepsilon_0 \alpha_d s_{xx}} = \frac{\alpha_{xx_{eff}}}{\alpha_d} \tag{6.19}$$

, so that the approximative relation between the optical and the MO dipole moment components is given as:

$$P_{x_{scalar}} = \frac{\alpha_{xx_{eff}}}{\alpha_d} \frac{\alpha_{off}}{\alpha_d} P_{y_{scalar}} \tag{6.20}$$

Figure 6.9 shows an example of this approximate relation and demonstrates how close this semi-scalar approach is to the exact result. Both the primary optical and the MO components for the case $D = 600\,\text{nm}$ are shown, from both tensorial and scalar calculations, all normalized to the same infinite layer calculation. This result opens up a pathway to undertake time efficient calculations of magneto-optical responses, in which the true magneto-optical nature of materials is considered only after the confinement induced optical polarization pattern has been calculated by means of relations similar to Equation (6.20). It

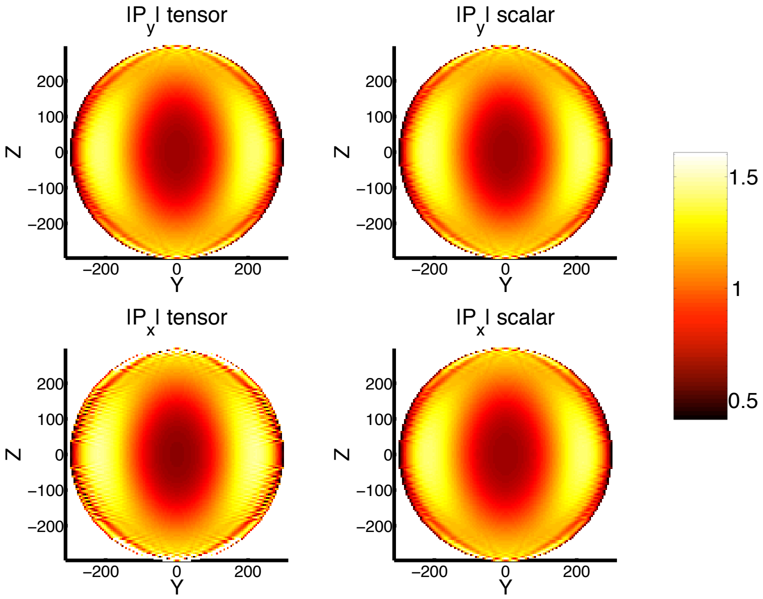

Figure 6.9: Primary optical (first row) and MO (second row) components for the case $D = 600\,\text{nm}$, from both tensorial (left column) and scalar (right column) calculations, all normalized to the IL calculation. The color scale is the same for all the plots.

is, however, important to stress that the scalar approach reached in Equation (6.20) no longer holds in conditions of strong MO effect.

As a summary, we have investigated the optical and magneto-optical responses of nano-scale ferromagnetic disks by means of numerical simulations, using a discrete dipole approximation. The disks were illuminated under normal incidence with a wavelength of $\lambda = 632.8\,\text{nm}$, assuming the transverse magneto-optical Kerr effect (T-MOKE) configuration. Results show that the strong similarity between the optical and magneto-optical nano-scale confinement effects also results in the fact that the normalized magneto-optically induced far-field light intensity relative change $^{\Delta I}/_{I}$, which is the quantity measured in experiments, is only weakly affected even in the case of sub-wavelength sized disks, so that the far-field predictions coming from a film electromagnetic solution [103] remain highly accurate. We demonstrate this by calculating the diffracted light intensities and intensity changes produced by nano-disk arrays, which are commonly used in experimental studies of nano-structure magneto-optics.

7

COMPOSITE MATERIALS

Research on metamaterial structures undergoes continuous progress due to their unique electromagnetic behavior and the associated application potential [120]. With constant advances in design approaches [121] and fabrication capabilities [122], metamaterial development appears to be restricted by the properties of naturally available materials used to build “à la carte" structures. In this sense, composite materials may assist with the tailoring of the optical properties of such sophisticated structures, for example considering a metamaterial structure embedded in a dielectric matrix.

Given that particle sizes larger than diameter $\sim 3\,\text{nm}$ (hundreds of atoms) become increasingly computationally demanding using exact techniques (like the Density Functional Theory), it is necessary to model these composite materials using either effective medium theories (such as the Maxwell-Garnett formalism [123]) or approximative solutions based for example on finite element methods, such as the DDA [82, 83].

In any case, effective medium theories describe the effective dielectric function of complex systems through the dielectric function of its constituents and some additional parameter, like the filling fraction of each component [41]. Therefore, these theories can provide just an approximate description of the effective behavior of complex mixtures and it is questionable to what extent real random composites can be described by simple mixing formulae. Indeed, none of these approaches (effective medium theories or DDA) explicitly considers the distortion of the optical properties due to the embedding medium, acknowledging that a more advanced description is necessary for a correct prediction of the observed effective dielectric function and its consequences. This ends in a disagreement with experimental results [124], in spite of the fact that these theories are well accepted by the scientific community.

As a step towards a more advanced description, we have tried to devise expressions for effective optical properties taking into account the change in the local properties of each constituent due to the relative concentration in its surroundings. In other words, we propose a Combined Approach (CA) that considers the composite material to be made of discrete elements whose optical properties have been renormalized so that each constituent perceives the presence of the other according to its actual proportion in the composite.

In this chapter we present a spectral analysis of composite nanostructures using an E-DDA [83], emphasizing the influences of optical properties of constituents and their concentration. We have performed simulations on typical shapes, like spheres and disks, both 3-D objects in which the discretization is followed by a random distribution of constituents when necessary. For the composition, we have used both noble and base metals, as well as the case of a metamaterial embedded in a dielectric matrix.

The chapter is organized as follows: in Section 7.1, the three models for the composite that we used are presented. In Section 7.2, the scattering geometry together with the material parameters are shown. Section 7.3 is devoted to the presentation and discussion of the main results obtained from our numerical model. Finally, in Section 7.4, the main conclusions of this research are summarized.

7.1 THREE MODELS FOR THE COMPOSITE

7.1.1 *Discrete Alloy (DA)*

Direct application of the E-DDA to some given composite nanostructures (composed of more than one constituent) will provide the solution that we refer to as Discrete Alloy (DA). In this approach, each constituent preserves its bulk optical properties. The E-DDA formalism allows for considering different distributions of the constituents. Our choice consists of an uniform random distribution, where the optical properties of each dipole are assigned based on the filling fraction of each constituent.

7.1.2 *Extended Maxwell-Garnett (EMG)*

In this case, direct application of the E-DDA to the nanostructure with all dipoles having the same averaged optical properties (ε_{MG}, μ_{MG}, given by Equations (3.22) and (3.23) respectively) will provide the solution that we refer to as Extended Maxwell-Garnett (EMG).

7.1.3 *Combined Approach (CA)*

Our Combined Approach (CA) considers the material to be composed of more than one constituent, each of them in the same relative concentration (and distribution) as in our DA approach, but whose optical properties have been renormalized so that each constituent takes account of the presence of the other.

7.2 SYSTEM DESCRIPTION AND MATERIAL PARAMETERS

We have performed simulations by using the E-DDA code on different composite materials and geometries, from conventional alloy-like metal-metal mixtures to more complex metamaterial-dielectric composites. For the first part (conventional mixtures), we have used permalloy-like mixtures (Py, composed of nickel and iron, a typical magneto-optical material with interesting applications [125]) as well as silver-gold (Ag-Au) alloys (which present typical plasmonic resonances in the visible range). The considered geometries have been a sphere of diameter $D = 60\,\text{nm}$ and a disk of diameter $D = 268\,\text{nm}$ and thickness $t = 2\,\text{nm}$ (same volume as the sphere). These geometries are often used in experiments and have a wide range of applications, as they are accessible to the current technology.

The bulk optical properties for silver and gold have been taken from Johnson and Christy [87], while the optical properties of iron and nickel have been taken from Krinchik and Artem'ev [126].

In order to correctly choose a proper value for the dipole spacing, we have performed a discretization study of the convergence of the absorption efficiency corresponding to a sphere of diameter $D = 60\,\text{nm}$, made of 50% Ag - 50% Au, by varying the dipole spacing from $d = 10\,\text{nm}$ to $d = 0.8\,\text{nm}$, as shown in Figure 7.1a. For this particular case, we have compared the Discrete Alloy and the Weighted Average (Equations (3.20) and (3.21)) approaches.

There are two remarkable features in these results. Firstly, the choice of a criterion for the local properties of each discrete element in the composite material is crucial, especially when some of the constituents show a resonant behavior within the spectral range under study. We shall return to this point later. Secondly, and concerning the mathematical convergence, our choice of $d = 2\,\text{nm}$ already provides us with stable results. This is consistent with the widely used grid fineness criterion ($|n|kd \lesssim 1$) [82]. Figure 7.1b shows the upper bound for the dipole spacing d according to such criterion for the optical properties of silver, gold, iron and nickel. As can be seen, the value of $d = 2\,\text{nm}$ is well below each of the curves for all wavelengths[1].

For the second part (metamaterial-dielectric composites), we have simulated a sphere of diameter $D = 3\,\text{mm}$ composed of a metamaterial having typical optical properties of a left-handed material [127], as shown in Figure 7.2 (notice the microwave range), and a dielectric material with $(\varepsilon, \mu) = (2, 1)$. The dipole spacing for these calculations was $d = 0.2\,\text{mm}$, according to the corresponding convergence criterion.

---

[1] For absorbing materials such as metals, the original criterion might not be sufficient, as the skin depth is far smaller than the wavelength.

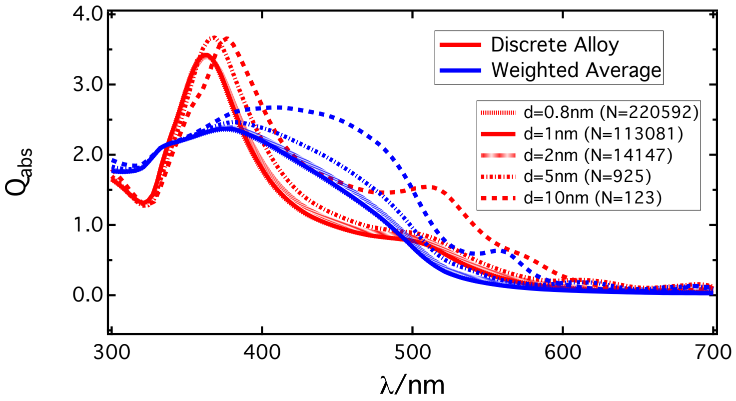

(a) Convergence of the spectral absorption efficiency for the heterogeneous (discrete alloy) and the homogeneous (weighted average) cases for several values of the dipole spacing, varying from $d = 10\,\text{nm}$ to $d = 0.8\,\text{nm}$.

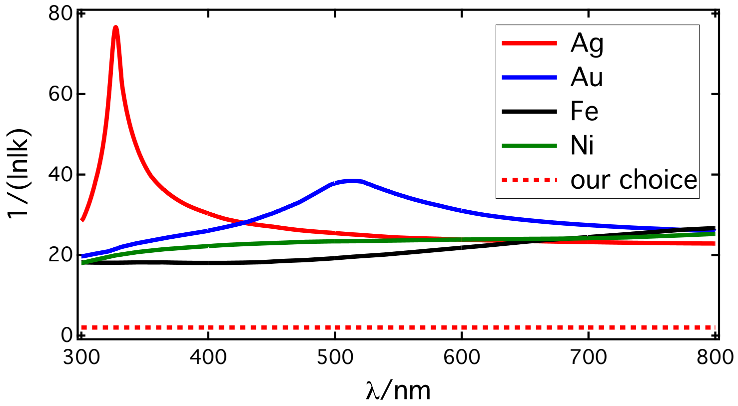

(b) Upper bound for the dipole spacing d according to the widely used grid fineness criterion $|n|kd \lesssim 1$ [82] for the optical properties of silver, gold, iron and nickel. Our choice of $d = 2\,\text{nm}$ is also shown (red dashed line) for comparison purposes only.

Figure 7.1: Discretization study corresponding to a sphere of diameter $D = 60\,\text{nm}$, made of 50% Ag - 50% Au.

7.3 RESULTS

7.3.1 *Conventional mixtures*

A summary of the results obtained for conventional mixtures is presented in Figures 7.3 and 7.4, where the absorption efficiency Q_{abs} as a function of both the incident wavelength (horizontal axis) and the relative concentration (vertical axis) is shown for Py-like mixtures (first row) as well as for silver-gold alloys (second row). Particle geometry is either spheres (Figure 7.3) or disks (Figure 7.4). In all cases the absorption efficiency has been computed twice, first using the Discrete Alloy approach (first column) and then applying the Extended Maxwell-Garnett effective medium theory (second column).

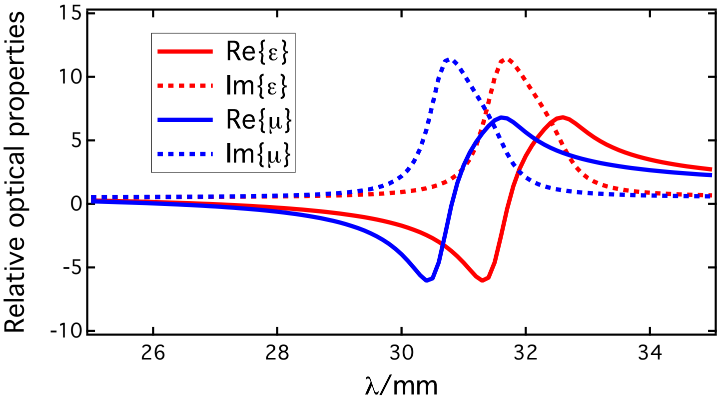

Figure 7.2: Relative optical properties (ε, μ) of the metamaterial that we have used, with both an electric and a magnetic resonance in the microwave range.

For the case of Py-like spheres (first row in Figure 7.3, in which none of the constituents show a resonant behavior), both the DA approach and the EMG theory give very similar results (if not outright indistinguishable), indicating that the constituents (Fe and Ni) either do not interact too much with each other or the result of it produces optical properties that are very similar to the averaged values. For the Ag-Au sphere case, however, both the DA and the EMG calculations preserve the individual resonances of the constituents (see arrows in the second row of Figure 7.3).

In the case of disks (Figure 7.4), however, both the mixing (DA) and the averaging (EMG) show evidence of the constituents' resonant behavior (see for example the first row in Figure 7.4, corresponding to Py-like mixtures, with the first resonance coming from the Ni and holding until more than 50% Fe content).

It is an experimental fact that, in the case of silver-gold spheres, experiment and theory agree that the plasmon frequency increases with increasing Ag content [128]. This means that, in the second row of Figure 7.3, we should see a single resonance peak varying smoothly with increasing Ag content, instead of the two separate resonances that are found. It is true that the EMG theory results already show more diffuse resonances, as a consequence of the optical properties averaging. On the other hand, the DA results keep the resonances further, as in this case we consider the composite as the union of two materials whose optical properties remain the same as in the original bulk material, therefore showing more of their original resonances. Far from explaining the experimental results, the DA approach (Figure 7.3c) slightly shifts the silver resonance to the blue, and not towards the gold as should be expected.

We now use our Combined Approach (Figure 7.5) in order to obtain the spectral absorption efficiency corresponding to the same Ag-Au sphere as in Figure 7.3 ($D = 60\,\text{nm}$).

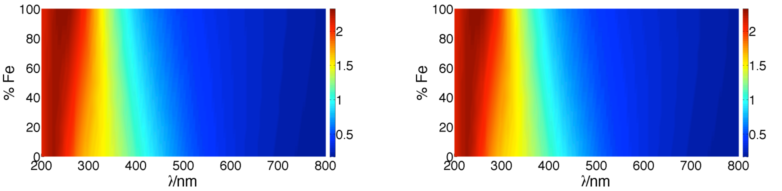

(a) Iron and nickel, DA approach. (b) Iron and nickel, EMG approach.

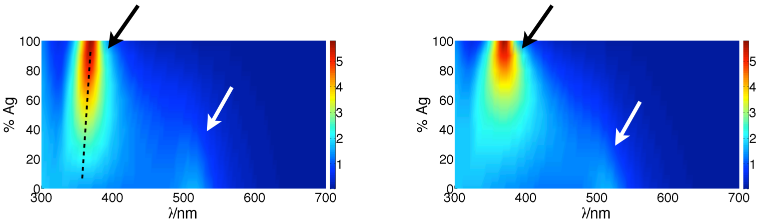

(c) Silver and gold, DA approach. (d) Silver and gold, EMG approach.

Figure 7.3: Spectral absorption efficiency corresponding to spheres of diameter $D = 60\,\mathrm{nm}$.

Now, the silver resonance starts to shift towards the gold resonance with decreasing Ag content. Although very promising, this result does not reach the desired outcome of a single resonance peak varying smoothly with composition with the right slope. It is important to know that S. Link et al. [124] already warn us about this, stating that the band structure of the gold-silver alloys is quite different from pure gold or silver. In the same reference, the authors claim that a linear combination of the dielectric functions of each material cannot explain the variation of the plasmon absorption maximum. Indeed, theoretical predictions agree with experimental results only when experimental dielectric data for alloy films are used [129].

Still, the Combined Approach shows an important advantage. Because it models each material fraction with its own properties but modulated by those of the nearest neighbors, it can implement some experimental facts concerning the constituents distribution (order-disorder, heterogeneities, cluster segregation) in a straightforward way.

7.3.2 *Metamaterial embedded in a dielectric matrix*

We have been working during the last years in the extension of several computational methods "to allow for materials with magnetic properties in the optical range". This is the case our E-DDA code, an Extension of the Discrete Dipole Approximation which allows for the calculation of materials with relative magnetic permeability $\mu < 0$ as well as tensorial optical properties. In addition, inhomogeneous media can be readily considered, so we may ask ourselves about the

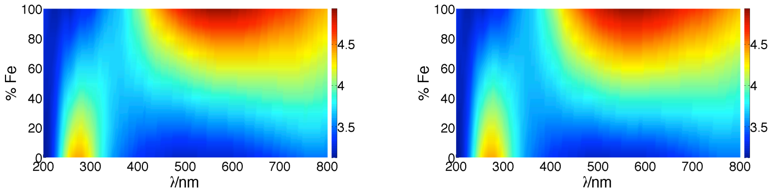

(a) Iron and nickel, DA approach.

(b) Iron and nickel, EMG approach.

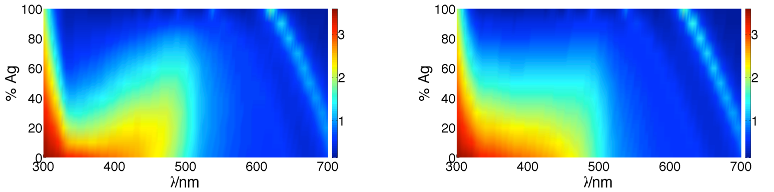

(c) Silver and gold, DA approach.

(d) Silver and gold, EMG approach.

Figure 7.4: Spectral absorption efficiency corresponding to disks of diameter $D = 268\,\mathrm{nm}$ and thickness $t = 2\,\mathrm{nm}$.

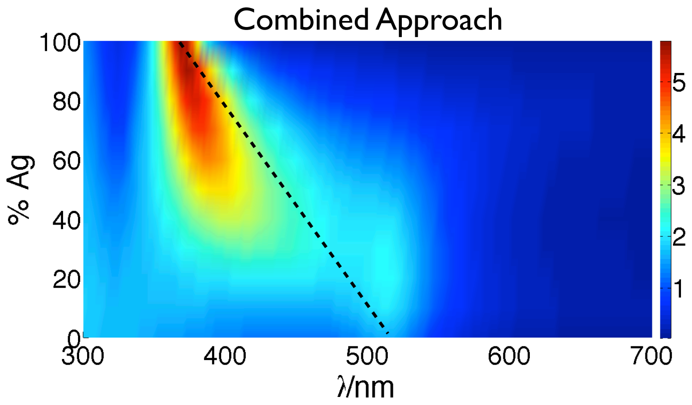

Figure 7.5: Spectral absorption efficiency corresponding to a sphere of diameter $D = 60\,\mathrm{nm}$ made of silver and gold, calculated with our Combined Approach.

behavior of composite materials with non-conventional optical properties.

It is possible to imagine a system where the nanostructured material (metamaterial) forms discrete elements integrated within a conventional material (e.g. a dielectric), which provides geometric support. This kind of composite may not be yet implemented, but will take on a new topicality as soon as metamaterials behavior is reliable and their properties the desired ones.

Figure 7.6 shows the spectral extinction efficiency corresponding to a sphere of diameter $D = 3\,\mathrm{mm}$ made of mix of a metamaterial, with optical properties given by Figure 7.2, and a dielectric material with $(\varepsilon, \mu) = (2, 1)$. Results in Figure 7.6 have been normalized by their corresponding maximum values (each approach separately), so the color is as much as 1 for each plot. The entire system is embedded in vacuum.

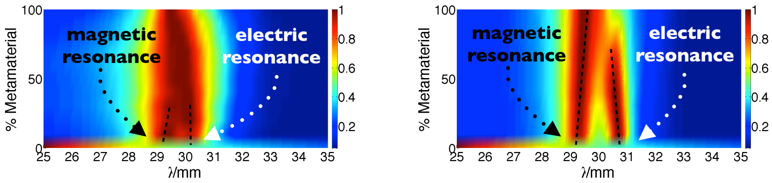

(a) Discrete Alloy.

(b) Extended Maxwell-Garnett.

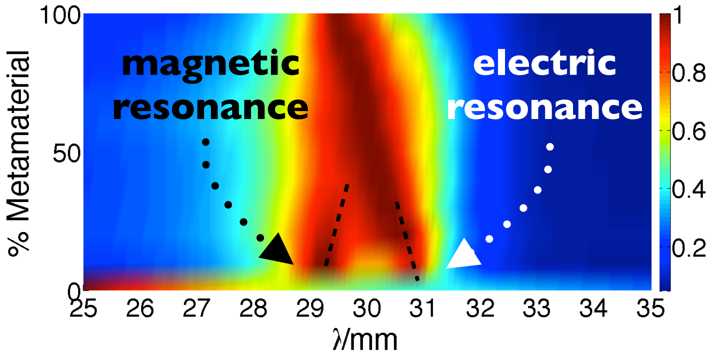

(c) Combined approach.

Figure 7.6: Normalized (by maximum values) spectral extinction efficiency corresponding to a sphere of diameter $D = 3\,\text{mm}$ made of a metamaterial and a dielectric material.

The first thing to notice when looking at Figure 7.6 is that there are significant differences between the three approaches (with the CA being a clear combination of both the DA approach and the EMG theory). EMG results show separately the positions of the electric and magnetic resonances while "red shifting" the resonance of electric origin. The DA approach, however, mixes up both resonances while preserving their spectral position even at very low metamaterial concentrations. Our CA shows features from both cases, with mixed up resonances as well as a clear shift towards the "red" at low metamaterial concentrations (see arrows in Figure 7.6).

It is important to note that the considered metamaterial has both an electric and a magnetic resonance in the microwave range. As we are embedding it in a dielectric matrix with $(\varepsilon, \mu) = (2, 1)$, only the electric resonance is affected ("red shifted") by the ambient medium. In order to explore this aspect further, we have considered a single dipole with the same optical properties as those given by Figure 7.2, either embedded in air or in a dielectric medium with $(\varepsilon, \mu) = (2, 1)$, in order to clearly see this selective shift. Figure 7.7 shows the extinction efficiency for this single dipole either embedded in air or in the dielectric medium, normalized by their maximum values respectively.

For this calculation, we have used our DA approach, considering a single dipole only.

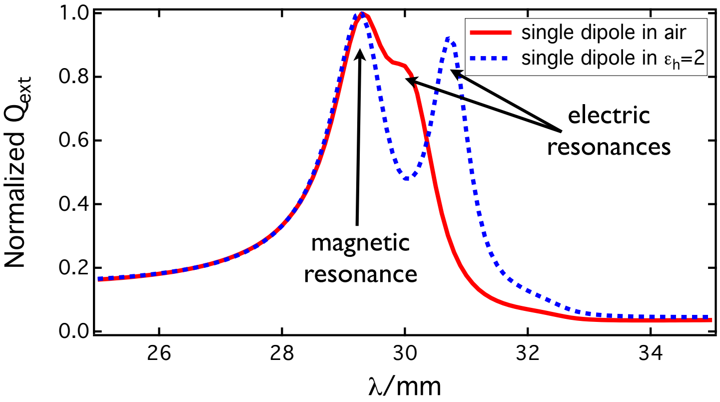

Figure 7.7: Normalized (by maximum values) spectral extinction efficiency corresponding to a single dipole with optical properties given by Figure 7.2, either embedded in air or in a dielectric material with $(\varepsilon, \mu) = (2, 1)$.

As expected, the magnetic resonance is unaffected by the surrounding dielectric medium. As for the electric resonance, not only the shift, but also the quantitative variation, are in agreement with previous results shown in Figure 7.6 (results in Figure 7.7 are normalized as well, so the maximum values for both situations are 1).

7.4 CONCLUSIONS

We have resorted to a Coupled Dipole Method code in order to compare several approaches to the analysis of the optical behavior of composite materials, starting with nanoscopic conventional objects in the visible domain. In the first place we have preserved for each discrete element the nature of its constituent material, assuming bulk properties, and secondly we have assigned some overall properties to each discrete element of the particle. When these two approaches are applied to silver/gold spheres and the proportion of each constituent is varied smoothly, the results completely disagree to those observed in the experiment, as they are described in the literature: instead of the smooth linear shift observed in the experimental resonant peak from the silver to the gold one, when the fraction of gold increases, what these models predict is either a stable position of the resonances, or even a shift in the opposite direction. With our Combined Approach, however, there is a clear move of the spectral peak in the direction pointed out by the experiment. Although the linear dependence predicted by this approach has a slope that is slightly smaller than the experimental one, we think that it is an advance in this kind of modeling, as it preserves the individual nature of the constituents and at the same time introduces a variation in the optical properties of a discrete element that is given by the properties of the surrounding medium. This is key in modeling any kind of composite material, admitting that handling macroscopic properties is only an approach to the exact solution of the electronic band structure of each particular discrete element. Not surprisingly, the difference between all these approaches becomes very small when there is no resonance within the spectral range of interest.

Then, considering that the former result is a sort of validation of our Combined Approach, we have applied it to a non-conventional material, whose properties are hypothesized here for millimeter objects in the microwave domain. The development and combination of technologies is continuously producing new metamaterials, and its combination with conventional materials will presumably produce composite materials for which the current modeling and computing capabilities do not appear to be fully prepared. Our version of the DDA code, the E-DDA code, has been formulated to tackle this problem, and is able to deal with non-conventional materials that can be characterized either with magnetic and tensor properties.

8

ADDITIONAL ASPECTS

8.1 CORRECTIONS TO THE POLARIZABILITY

In Section 3.1.3, a correction to the polarizability tensor due to the "radiative reaction" was introduced in Equation (3.12). This correction is $O((kd)^3)$, the product kd expressing the ratio of d to λ, being d the distance of the discretization, in principle much smaller than λ. Several other corrections of $O((kd)^2)$ have been proposed. The first one was proposed by Goedecke and O'Brien [130] and independently in two other publications by different authors [131, 132]. Draine and Goodman [133] pointed out that considering electric fields constant for evaluating integrals over a cell introduces errors of order $O((kd)^2)$. This represents a problem for many polarizability corrections, based on integral equations. Draine and Goodman approached this problem from a different angle. They determined the optimal polarizability in the sense that an infinite lattice of point dipoles with such polarizability would lead to the same propagation of plane waves[1] as in a medium with a given refractive index. This polarizability was called lattice dispersion relation (LDR). It has been shown [134] that the LDR derivation is not completely accurate, since the resulting dipole moment does not satisfy the transversality condition, for which a correction was proposed. This corrected LDR (CLDR) differs principally in the fact that the polarizability tensor cannot be made isotropic but only diagonal [134], though not dependent on the incident polarization.

Dungey and Bohren [135], using results by Doyle [136], proposed the following treatment of the polarizability. First, each cubic cell is replaced by the inscribed sphere that is called a dipolar subunit with a higher relative electric permittivity as determined by the Maxwell-Garnett effective medium theory [8]. Next, the dipole moment of the equivalent sphere is determined using the Mie theory, and the polarizability is defined as [15]:

$$\alpha^M = \frac{6\pi i}{k^3} a_1 \tag{8.1}$$

, where a_1 is the electric dipole coefficient from the Mie theory. We denote this formulation for the polarizability as the a_1-term method (note that this terminology was introduced later [137]). It should be noted that the Mie theory is based on the assumption that the external electric field is a plane wave. In most applications of the DDA this

---

[1] With certain direction of propagation and polarization state.

is true for the incident electric field, but not for the field created by other subvolumes. Therefore the a_1-term method is expected to be correct only for very small cell size.

The previous approaches have in common that they all start from the Clausius-Mossotti relation and simply add a finite-frequency correction. They also suppose that the field susceptibility tensor is constant over any given subunit. It was pointed out that the Clausius-Mossotti relation may not hold for every subunit; rather, for each subunit the polarizability should be related to its local environment [138–140]. Chaumet et al. [141] proposed direct integration of the Green's tensor (IT). A Weyl expansion of the Green's tensor is performed, transforming it to a form allowing efficient numerical computation.

All the above techniques are aimed at reducing discretization errors; only a few aim at reducing shape errors. Some of them employ adaptive discretization (different dipole sizes) to better describe the shape of the scatterer. Another approach is to average the susceptibility in boundary subvolumes[2], the so-called weighted discretization (WD), as proposed by Piller [142].

Currently, there are no rigorous theoretical reasons for preferring one formulation over others. However, theoretical analyses of DDA convergence when refining discretization recently conducted by Yurkin et al. [143], showed that IT and WD significantly improve the convergence of shape and discretization errors, respectively. Experimental verification of these theoretical conclusions is still to be performed.

8.2 EXTENDED INFINITE FILM

Electromagnetic metamaterials are artificially structured media typically composed of arrays of resonant electromagnetic circuits, the dimension and spacing of which are considerably smaller than the free-space wavelengths of operation. The constitutive parameters for metamaterials exhibit artifacts related to the finite size of the metamaterial cell relative to the wavelength. The unified model presented in this section will be to consider a wave propagating in an infinite, periodic array of thin, polarizable sheets, in a similar fashion as Smith [144]. Although metamaterial elements certainly have considerable physical extent along the propagation direction within the unit cell, we assume here that their effective dipolar response is restricted to a plane.

The polarization of an infinite array of dipoles illuminated with a monochromatic electromagnetic wave can be computed self-consistently by considering the field at the location of one dipole formed from the summation of the responding fields from all dipoles excluding the

---

[2] Any subvolume that has non-zero intersection with both the scatterer and the outer medium. All such subvolumes are accounted for.

given dipole. The effective permittivity or permeability of the collective can then be expressed in terms of the polarizability of the individual dipolar element. For field excitations at finite frequency and wavelength, retardation effects lead to dispersion effects that can be included in the dipole model [145].

Within the scope of the dipole model, it is convenient to first sum over planes of dipoles for periodic arrays and sub-sequently to take into account the interaction of the planes along the propagation direction [145, 146]. Since the applied electromagnetic field is uniform over a plane of dipoles (assuming the wave is incident along a principal axis), the effects of spatial dispersion occur due to the phase variation of the field along the direction perpendicular to the planes.

The geometry of the model is shown in Figure 8.1. A series of l simultaneously electrically and magnetically polarizable, planar sheets, of width d, is spaced apart with periodicity t. We assume that an electromagnetic wave propagates in the direction along the normal to the sheets, with fields polarized in the plane of the sheets.

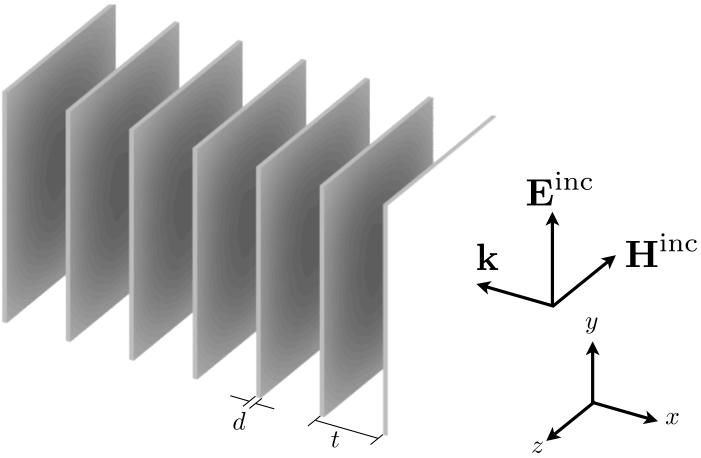

Figure 8.1: Periodic system of l electrically and magnetically polarizable sheets. The sheets have thickness d and are spaced a distance t apart. An electromagnetic wave is assumed to propagate along the direction normal to the sheets.

We must calculate l electric and magnetic dipole moments. Let's write here the i-th electric and magnetic dipole moments $\mathbf{p}_i$ and $\mathbf{m}_i$, with $i = 1 \dots l$ (and assuming the entire system is in vacuum):

$$\mathbf{p}_i = \varepsilon_0 \bar{\bar{\alpha}} \left[\mathbf{E}_i^{\text{inc}} + \sum_{j=1}^{l} \left(\sum_{k \in j} \bar{\bar{\mathbf{A}}}_{ik}^{(ee)} \mathbf{p}_j + \sum_{k \in j} \bar{\bar{\mathbf{A}}}_{ik}^{(eh)} \mathbf{m}_j \right) \right] \tag{8.2}$$

$$\mathbf{m}_i = \bar{\bar{\chi}} \left[\mathbf{H}_i^{\text{inc}} + \sum_{j=1}^{l} \left(\sum_{k \in j} \bar{\bar{\mathbf{A}}}_{ik}^{(he)} \mathbf{p}_j + \sum_{k \in j} \bar{\bar{\mathbf{A}}}_{ik}^{(hh)} \mathbf{m}_j \right) \right] \tag{8.3}$$

, where we are already assuming that both the incident electromagnetic field on each layer (which can be written as $\mathbf{E}_i^{inc} = \mathbf{E}_0 e^{-ikx_i}$ and $\mathbf{H}_i^{inc} = \mathbf{H}_0 e^{-ikx_i}$, where $|\mathbf{H}_0| = \sqrt{\frac{\varepsilon_0}{\mu_0}}|\mathbf{E}_0|$ and $x_i = -(i-1) \cdot t$) and the dipole moments (electric and magnetic) of all the dipoles within each layer are all the same, which under normal incidence is correct.

A word about the notation:

1. There are l layers. This means that we must have a system of $2l$ matrix equations (each matrix equation having 3 equations as well).
2. $i = 1 \dots l$ represents the layer i, on which we are calculating the effect of the layer i itself and the rest of the other $l-1$ layers. Each layer acquires an electric dipole moment $\mathbf{p}_i$ and a magnetic dipole moment $\mathbf{m}_i$.
3. j runs over all the layers i with $i = 1 \dots l$. It represents the layers that are *creating* an effect on itself and on the other layers.
4. $k \in j$ is actually a double-index, as it runs over a 2D lattice, representing all dipoles on layer j.
5. $\mathbf{p}_j$ and $\mathbf{m}_j$ are the electric and magnetic dipole moments of the layer j ($j = 1 \dots l$), respectively.

Each electric and magnetic dipole produces both an electric and a magnetic field on each other. To calculate both the electric and the magnetic fields, we assume that the dipoles $\mathbf{p}_i$ and $\mathbf{m}_i$ are located on the center of the layer i (this is, their coordinates are $\mathbf{r}_i = (x_i, 0, 0)$).

$\bar{\bar{\mathbf{A}}}_{ik}^{(ee)} \rightarrow$ electric field produced on layer i by electric dipoles located on k

$\bar{\bar{\mathbf{A}}}_{ik}^{(eh)} \rightarrow$ electric field produced on layer i by magnetic dipoles located on k

$\bar{\bar{\mathbf{A}}}_{ik}^{(he)} \rightarrow$ magnetic field produced on layer i by electric dipoles located on k

$\bar{\bar{\mathbf{A}}}_{ik}^{(hh)} \rightarrow$ magnetic field produced on layer i by magnetic dipoles located on k

We can make further assumptions and simplify the notation:

1.

$$\sum_{k \in j, k \neq 0} \bar{\bar{\mathbf{A}}}_{jk}^{(ee)} = \bar{\bar{\mathbf{A}}}_0 \quad \forall j = 1 \dots l \tag{8.4}$$

$$\sum_{k \in j, k \neq 0} \bar{\bar{\mathbf{A}}}_{jk}^{(eh)} = \bar{\bar{\mathbf{B}}}_0 \quad \forall j = 1 \dots l \tag{8.5}$$

$$\sum_{k \in j, k \neq 0} \bar{\bar{\mathbf{A}}}_{jk}^{(he)} = \bar{\bar{\mathbf{C}}}_0 \quad \forall j = 1 \dots l \tag{8.6}$$

$$\sum_{k \in j, k \neq 0} \bar{\bar{\mathbf{A}}}_{jk}^{(hh)} = \bar{\bar{\mathbf{D}}}_0 \quad \forall j = 1 \dots l \tag{8.7}$$

(the sums relating the effect of one layer on itself are layer independent)

2.

$$\sum_{k\in j}\bar{\bar{\mathbf{A}}}^{(ee)}_{j'k}=\sum_{k\in j'}\bar{\bar{\mathbf{A}}}^{(ee)}_{jk}=\bar{\bar{\mathbf{A}}}_{|j'-j|}\tag{8.8}$$

$$\sum_{k\in j}\bar{\bar{\mathbf{A}}}^{(eh)}_{j'k}=\sum_{k\in j'}\bar{\bar{\mathbf{A}}}^{(eh)}_{jk}=\bar{\bar{\mathbf{B}}}_{|j'-j|}\tag{8.9}$$

$$\sum_{k\in j}\bar{\bar{\mathbf{A}}}^{(he)}_{j'k}=\sum_{k\in j'}\bar{\bar{\mathbf{A}}}^{(he)}_{jk}=\bar{\bar{\mathbf{C}}}_{|j'-j|}\tag{8.10}$$

$$\sum_{k\in j}\bar{\bar{\mathbf{A}}}^{(hh)}_{j'k}=\sum_{k\in j'}\bar{\bar{\mathbf{A}}}^{(hh)}_{jk}=\bar{\bar{\mathbf{D}}}_{|j'-j|}\tag{8.11}$$

(the sums relating the effect of the layer j on the layer j' are the same as the sums relating the effect of the layer j' on the layer j)

Please notice that **Equations** (8.8)**-**(8.11) **are true only because of the sum**. The equalities do not hold addend by addend. Please take into account that, although the sums may be the same, the effect itself is not the same because $\mathbf{p}_j \neq \mathbf{p}_{j'}$ and $\mathbf{m}_j \neq \mathbf{m}_{j'}$ (and the effect is the product of the sum and the dipole moment).

We may write Equations (8.2) and (8.3) in terms of the exciting fields instead of the acquired dipole moments, just to avoid numerical instabilities. By using the relations $\mathbf{p}_i = \varepsilon_0\bar{\bar{\alpha}}\mathbf{E}_i$ and $\mathbf{m}_i = \bar{\bar{\chi}}\mathbf{H}_i$, and using the previously introduced notation, we get:

$$\mathbf{E}_i=\mathbf{E}_i^{\text{inc}}+\sum_{j=1}^{l}\left(\varepsilon_0\bar{\bar{\mathbf{A}}}_{|i-j|}\bar{\bar{\alpha}}\mathbf{E}_j+\bar{\bar{\mathbf{B}}}_{|i-j|}\bar{\bar{\chi}}\mathbf{H}_j\right)\tag{8.12}$$

$$\mathbf{H}_i=\mathbf{H}_i^{\text{inc}}+\sum_{j=1}^{l}\left(\varepsilon_0\bar{\bar{\mathbf{C}}}_{|i-j|}\bar{\bar{\alpha}}\mathbf{E}_j+\bar{\bar{\mathbf{D}}}_{|i-j|}\bar{\bar{\chi}}\mathbf{H}_j\right)\tag{8.13}$$

Arranging the system of equations in matrix form, we have:

$$\bar{\bar{\mathbf{M}}}\mathbf{x}=\mathbf{x}^{\text{inc}}\tag{8.14}$$

, where $\bar{\bar{\mathbf{M}}}$ is a $6l \times 6l$ block-symmetric matrix containing all the needed sums, given by:

$$\bar{\bar{\mathbf{M}}} = \left(\begin{array}{cc|cc|c|cc}
\bar{\bar{\mathbf{I}}} - \varepsilon_0 \bar{\bar{\mathbf{A}}}_0 \bar{\bar{\alpha}} & -\bar{\bar{\mathbf{B}}}_0 \bar{\bar{\chi}} & -\varepsilon_0 \bar{\bar{\mathbf{A}}}_1 \bar{\bar{\alpha}} & -\bar{\bar{\mathbf{B}}}_1 \bar{\bar{\chi}} & \dots & -\varepsilon_0 \bar{\bar{\mathbf{A}}}_{l-1} \bar{\bar{\alpha}} & -\bar{\bar{\mathbf{B}}}_{l-1} \bar{\bar{\chi}} \\
-\varepsilon_0 \bar{\bar{\mathbf{C}}}_0 \bar{\bar{\alpha}} & \bar{\bar{\mathbf{I}}} - \bar{\bar{\mathbf{D}}}_0 \bar{\bar{\chi}} & -\varepsilon_0 \bar{\bar{\mathbf{C}}}_1 \bar{\bar{\alpha}} & -\bar{\bar{\mathbf{D}}}_1 \bar{\bar{\chi}} & \dots & -\varepsilon_0 \bar{\bar{\mathbf{C}}}_{l-1} \bar{\bar{\alpha}} & -\bar{\bar{\mathbf{D}}}_{l-1} \bar{\bar{\chi}} \\
\hline
-\varepsilon_0 \bar{\bar{\mathbf{A}}}_1 \bar{\bar{\alpha}} & -\bar{\bar{\mathbf{B}}}_1 \bar{\bar{\chi}} & \bar{\bar{\mathbf{I}}} - \varepsilon_0 \bar{\bar{\mathbf{A}}}_0 \bar{\bar{\alpha}} & -\bar{\bar{\mathbf{B}}}_0 \bar{\bar{\chi}} & \dots & -\varepsilon_0 \bar{\bar{\mathbf{A}}}_{l-2} \bar{\bar{\alpha}} & -\bar{\bar{\mathbf{B}}}_{l-2} \bar{\bar{\chi}} \\
-\varepsilon_0 \bar{\bar{\mathbf{C}}}_1 \bar{\bar{\alpha}} & -\bar{\bar{\mathbf{D}}}_1 \bar{\bar{\chi}} & -\varepsilon_0 \bar{\bar{\mathbf{C}}}_0 \bar{\bar{\alpha}} & \bar{\bar{\mathbf{I}}} - \bar{\bar{\mathbf{D}}}_0 \bar{\bar{\chi}} & \dots & -\varepsilon_0 \bar{\bar{\mathbf{C}}}_{l-2} \bar{\bar{\alpha}} & -\bar{\bar{\mathbf{D}}}_{l-2} \bar{\bar{\chi}} \\
\hline
\vdots & \vdots & \vdots & \vdots & \vdots & \vdots & \vdots \\
\hline
-\varepsilon_0 \bar{\bar{\mathbf{A}}}_{l-1} \bar{\bar{\alpha}} & -\bar{\bar{\mathbf{B}}}_{l-1} \bar{\bar{\chi}} & -\varepsilon_0 \bar{\bar{\mathbf{A}}}_{l-2} \bar{\bar{\alpha}} & -\bar{\bar{\mathbf{B}}}_{l-2} \bar{\bar{\chi}} & \dots & \bar{\bar{\mathbf{I}}} - \varepsilon_0 \bar{\bar{\mathbf{A}}}_0 \bar{\bar{\alpha}} & -\bar{\bar{\mathbf{B}}}_0 \bar{\bar{\chi}} \\
-\varepsilon_0 \bar{\bar{\mathbf{C}}}_{l-1} \bar{\bar{\alpha}} & -\bar{\bar{\mathbf{D}}}_{l-1} \bar{\bar{\chi}} & -\varepsilon_0 \bar{\bar{\mathbf{C}}}_{l-2} \bar{\bar{\alpha}} & -\bar{\bar{\mathbf{D}}}_{l-2} \bar{\bar{\chi}} & \dots & -\varepsilon_0 \bar{\bar{\mathbf{C}}}_0 \bar{\bar{\alpha}} & \bar{\bar{\mathbf{I}}} - \bar{\bar{\mathbf{D}}}_0 \bar{\bar{\chi}}
\end{array}\right)$$

$\mathbf{x}$ and $\mathbf{x}^{\text{inc}}$ are 6l-dimensional vectors containing the total exciting electric and magnetic fields and the incoming electric and magnetic fields on each layer respectively (3 components each).

$$\mathbf{x} = \begin{pmatrix} \mathbf{E}_1 \\ \mathbf{H}_1 \\ \mathbf{E}_2 \\ \mathbf{H}_2 \\ \vdots \\ \mathbf{E}_l \\ \mathbf{H}_l \end{pmatrix}; \qquad \mathbf{x}_{\text{inc}} = \begin{pmatrix} \mathbf{E}_1^{\text{inc}} \\ \mathbf{H}_1^{\text{inc}} \\ \mathbf{E}_2^{\text{inc}} \\ \mathbf{H}_2^{\text{inc}} \\ \vdots \\ \mathbf{E}_l^{\text{inc}} \\ \mathbf{H}_l^{\text{inc}} \end{pmatrix} \tag{8.15}$$

The formal solution can be written as:

$$\mathbf{x} = \bar{\bar{\mathbf{M}}}^{-1} \mathbf{x}_{\text{inc}} \tag{8.16}$$

8.3 PERIODIC ARRAY OF MAGNETO-OPTICAL PARTICLES ON A MULTILAYERED SUBSTRATE

We present a generalization of the discrete dipole approximation method to the scattering of light by a periodic array of anisotropic (magneto-optic) particles on a multilayered substrate. This formulation of the coupled dipole method relies on the same direct-space discretization scheme that is widely used to study the scattering of light by finite objects. The method is extended to deal with an array of particles near or on a multilayered substrate by computing the appropriated Green's function. The electric field diffracted by a plasmonic structure made of a plane metallic slab in interaction with a periodic array of small particles may then be obtained. The field can be computed in the near and far zones, under plane-wave illumination or using a point electric-dipole source.

8.3.1 *Reflection dyadic from a layered media bounded by a planar surface*

Let us consider a multilayered substrate as sketched in Figure 8.2.

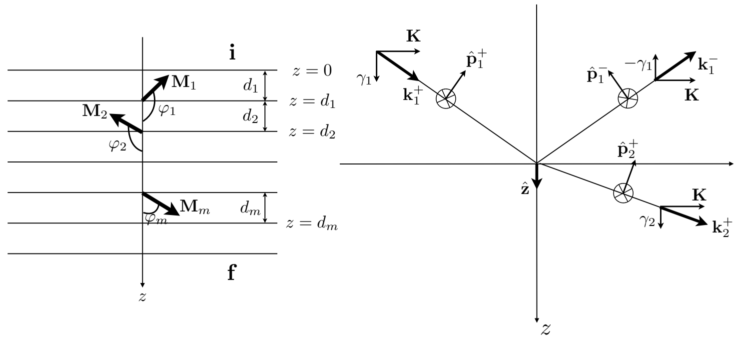

Figure 8.2: Sketch of the geometry of the multilayered system together with the definition of the different vectors (following Sipe's notation [147]).

We assume an incoming plane wave given by:

$$\mathbf{E}_{\mathbf{i}}^{\mathrm{inc}} = \left(E_{s,\mathbf{i}}^{+}\hat{\mathbf{s}} + E_{p,\mathbf{i}}^{+}\hat{\mathbf{p}}_{\mathbf{i}}^{+}\right) e^{i\mathbf{K}\cdot\mathbf{r}} e^{+i\gamma_i z} \tag{8.17}$$

, where $\gamma_i = +\sqrt{k_i^2 - |\mathbf{K}|^2}$ with $k_i = k_0 n_i = (\omega/c) n_i$ being n_i the (real) refraction index in the **i** region of the incoming beam (z<0). Following Sipe's notation [147],

$$\mathbf{k}_{\mathrm{inc}} \equiv \mathbf{k}_{\mathbf{i}}^{+} = \mathbf{K} + \gamma_i \hat{\mathbf{u}}_z \quad , \quad \mathbf{K} = k_x \hat{\mathbf{u}}_x + k_u \hat{\mathbf{u}}_y \tag{8.18}$$

$$\hat{\mathbf{s}}(\mathbf{K}) \equiv \frac{\mathbf{K} \times \hat{\mathbf{u}}_z}{|\mathbf{K}|} \tag{8.19}$$

$$\hat{\mathbf{p}}_{\mathbf{i}}^{\pm}(\mathbf{K}) \equiv \mathbf{k}_{\mathbf{i}}^{\pm} \times \hat{\mathbf{s}} = (\mathbf{K} \pm \gamma_i \hat{\mathbf{u}}_z) \times \hat{\mathbf{s}} = \frac{-|\mathbf{K}|^2 \hat{\mathbf{u}}_z \pm \gamma_i \mathbf{K}}{|\mathbf{K}| k_i} \tag{8.20}$$

Notice that the sign of $\hat{\mathbf{p}}$ differs from the definition in the original Sipe's paper. With the present definition, the z-component of $\hat{\mathbf{p}}^{\pm}$ is always negative. In terms of the reflection matrix $\bar{\bar{\mathbf{R}}}(\mathbf{K})$, the "specular" reflected beam will be:

$$\begin{aligned}\mathbf{E}_{\mathbf{i}}^{\text{ref}} &= \left(E_{s,\mathbf{i}}^{-}\hat{\mathbf{s}} + E_{p,\mathbf{i}}^{-}\hat{\mathbf{p}}_{\mathbf{i}}^{-}\right) e^{i\mathbf{K}\cdot\mathbf{r}} e^{-i\gamma_i z} \\ &= \left[\left(R_{ss}E_{s,\mathbf{i}}^{+} + R_{sp}E_{p,\mathbf{i}}^{+}\right)\hat{\mathbf{s}} + \left(R_{pp}E_{p,\mathbf{i}}^{+} + R_{ps}E_{s,\mathbf{i}}^{+}\right)\hat{\mathbf{p}}_{\mathbf{i}}^{-}\right] e^{i\mathbf{K}\cdot\mathbf{r}} e^{-i\gamma_i z}\end{aligned} \tag{8.21}$$

, and the transmitted beam:

$$\begin{aligned}\mathbf{E}_{\mathbf{f}}^{\text{tra}} &= \left(E_{s,\mathbf{f}}^{+}\hat{\mathbf{s}} + E_{p,\mathbf{f}}^{+}\hat{\mathbf{p}}_{\mathbf{f}}^{+}\right) e^{i\mathbf{K}\cdot\mathbf{r}} e^{+i\gamma_f z} \\ &= \left[\left(T_{pp}E_{p,\mathbf{i}}^{+} + T_{ps}E_{s,\mathbf{i}}^{+}\right)\hat{\mathbf{p}}_{\mathbf{f}}^{+} + \left(T_{ss}E_{s,\mathbf{i}}^{+} + T_{sp}E_{p,\mathbf{i}}^{+}\right)\hat{\mathbf{s}}\right] e^{i\mathbf{K}\cdot\mathbf{r}} e^{i\gamma_f z}\end{aligned} \tag{8.22}$$

The solution for the total field in the region **i** ($z < 0$) is simply given by the sum of incident and reflected waves:

$$\begin{aligned}\mathbf{E}_0(\mathbf{r}) = \left(E_{s,\mathbf{i}}^{+}\hat{\mathbf{s}} + E_{p,\mathbf{i}}^{+}\hat{\mathbf{p}}_{\mathbf{i}}^{+}\right) e^{i\mathbf{K}\cdot\mathbf{r}} e^{+i\gamma_i z} \\ + \left(E_{s,\mathbf{i}}^{-}\hat{\mathbf{s}} + E_{p,\mathbf{i}}^{-}\hat{\mathbf{p}}_{\mathbf{i}}^{-}\right) e^{i\mathbf{K}\cdot\mathbf{r}} e^{-i\gamma_i z}\end{aligned} \tag{8.23}$$

8.3.2 *Finite target on a flat surface*

Let us consider a finite target characterized by a dielectric permittivity tensor $\bar{\bar{\varepsilon}}(\mathbf{r})$ embedded in an otherwise homogeneous media **i** with $\varepsilon_m = n_{\mathbf{i}}^2$ (real). The object is located over a flat surface ($z = 0$) of known Fresnel reflection coefficients. In absence of free currents, it may be shown that the electric field is given by the solution of the integral equation:

$$\mathbf{E}(\mathbf{r}) = \mathbf{E}_0(\mathbf{r}) + k_0^2 \int \bar{\bar{\mathbf{G}}}(\mathbf{r},\mathbf{r}')\left[\varepsilon(\mathbf{r}') - \varepsilon_m\right]\mathbf{E}(\mathbf{r}')d^3\mathbf{r}' \tag{8.24}$$

, where $k = \sqrt{\varepsilon_m}\omega/c$ and $k_0 = \omega/c$. $\mathbf{E}_0(\mathbf{r})$ is the solution of the Maxwell equations in absence of the target. For a multilayered substrate, it is given by Equation (8.23) (to this end we will consider only fields in the **i** region. We then remove the **i** label in what follows).

The Green tensor $\bar{\bar{\mathbf{G}}}(\mathbf{r},\mathbf{r}_0)$ connects an electric dipole source $\mathbf{p}$ at a position $\mathbf{r}_0$ to the electric field at a position $\mathbf{r}$ through the relation:

$$\mathbf{E}(\mathbf{r})_{\text{dipole}} = \frac{k^2}{\varepsilon_m \varepsilon_0}\bar{\bar{\mathbf{G}}}(\mathbf{r},\mathbf{r}_0)\mathbf{p} \tag{8.25}$$

When these two points are located in the same region, $\bar{\bar{\mathbf{G}}}(\mathbf{r},\mathbf{r}_0)$ can be written as the sum of a free space (source) contribution and the reflected (non-singular) contribution:

$$\bar{\bar{\mathbf{G}}}(\mathbf{r},\mathbf{r}_0) = \bar{\bar{\mathbf{G}}}^{(0)}(\mathbf{r},\mathbf{r}_0) + \bar{\bar{\mathbf{G}}}_{B,surf}(\mathbf{r},\mathbf{r}_0) \tag{8.26}$$

8.3.3 *Periodic array of magneto-optical particles on a surface*

Let us consider a periodic (rectangular) array of "anisotropic" objects. For each small volume element of one of the objects (let's say the one at the "center" of the lattice), located at $\mathbf{r}_i$, we have a periodic array of small volume elements located at:

$$\mathbf{r}_{i;n,m} = \mathbf{r}_i + na\hat{\mathbf{u}}_x + mb\hat{\mathbf{u}}_y \quad \text{with } n,m \text{ integers} \tag{8.27}$$

For a non-perturbed field given by Equation (8.23), $E_0 \sim e^{i\mathbf{K}\cdot\mathbf{r}}$, the induced dipole in each volume element does not depend on n,m except for a phase factor, i.e.:

$$\mathbf{p}_{i;n,m} = \mathbf{p}_i e^{i\mathbf{K}\cdot(\mathbf{r}_{i;n,m}-\mathbf{r}_i)} = \mathbf{p}_i e^{i\mathbf{K}\cdot(na\hat{\mathbf{u}}_x+mb\hat{\mathbf{u}}_y)} \tag{8.28}$$

, where $\mathbf{p}_i \equiv \mathbf{p}_{i;0,0} = \varepsilon_m\varepsilon_0\bar{\bar{\alpha}}\mathbf{E}^{inc}$, being $\mathbf{E}^{inc}$ the actual incoming field towards the dipole located at $\mathbf{r}_i$. The total scattered field is then given by:

$$\begin{aligned}\mathbf{E}_{scatt} &= \frac{k^2}{\varepsilon_m\varepsilon_0}\sum_{n,m}\sum_{i=1}^{N}\bar{\bar{\mathbf{G}}}(\mathbf{r},\mathbf{r}_{i;n,m})\mathbf{p}_{i;n,m} \\ &= \frac{k^2}{\varepsilon_m\varepsilon_0}\sum_{i=1}^{N}\left\{\sum_{n,m}\bar{\bar{\mathbf{G}}}(\mathbf{r},\mathbf{r}_{i;n,m})e^{i\mathbf{K}\cdot(na\hat{\mathbf{u}}_x+mb\hat{\mathbf{u}}_y)}\right\}\mathbf{p}_i\end{aligned} \tag{8.29}$$

8.3.3.1 *Green's sum and diffracted beams*

Let us discuss the Green sum and some of its general properties. A useful representation of the Green tensor can be obtained by using a Weyl expansion:

$$g(r) \equiv \frac{e^{ik|\mathbf{r}-\mathbf{r}_0|}}{4\pi|\mathbf{r}-\mathbf{r}_0|} = \int\frac{d^2\mathbf{K}}{(2\pi)^2}e^{i\mathbf{K}\cdot(\mathbf{r}-\mathbf{r}_0)}\left\{\frac{i}{2\gamma}e^{i\gamma|z-z_0|}\right\} \tag{8.30}$$

, where $\gamma = +\sqrt{k^2-|\mathbf{K}|^2}$. We then have:

$$\bar{\bar{\mathbf{G}}}^{(0)}_E(\mathbf{r},\mathbf{r}_0)\mathbf{p} = \int\frac{d^2\mathbf{K}'}{(2\pi)^2}\left\{\bar{\bar{\mathbf{g}}}^{(0)}(\mathbf{K}',z,z_0)\mathbf{p}\right\}e^{i\mathbf{K}'\cdot(\mathbf{r}-\mathbf{r}_0)} \tag{8.31}$$

, where:

$$\bar{\bar{\mathbf{g}}}^{(0)}(\mathbf{K}', z, z_0)\mathbf{p} \equiv k^2 \left\{(\mathbf{p}\cdot\hat{\mathbf{s}})\hat{\mathbf{s}} + (\mathbf{p}\cdot\hat{\mathbf{p}}^{\pm})\hat{\mathbf{p}}^{\pm}\right\} \frac{i}{2\gamma} e^{\pm i\gamma(z-z_0)} \tag{8.32}$$

and $+(-)$ corresponds to waves propagating towards $z > z_0$ ($z < z_0$). $\hat{\mathbf{s}}$ and $\hat{\mathbf{p}}$ are unitary vectors perpendicular (s) and parallel (p) to the plane of incidence, given by Equations (8.19) and (8.20), respectively.

By using the Weyl expansion,

$$\bar{\bar{\mathbb{G}}}(\mathbf{r})\mathbf{p}_i \equiv \left\{\sum_{n,m} \bar{\bar{\mathbf{G}}}(\mathbf{r}, \mathbf{r}_{i;n,m}) e^{i\mathbf{K}\cdot(na\hat{\mathbf{u}}_x + mb\hat{\mathbf{u}}_y)}\right\} \mathbf{p}_i \tag{8.33}$$

$$= \int \frac{d^2\mathbf{K}'}{(2\pi)^2} \left\{\bar{\bar{\mathbf{g}}}(\mathbf{K}', z, z_i)\mathbf{p}_i\right\} e^{i\mathbf{K}'\cdot(\mathbf{r}-\mathbf{r}_i)} \times \sum_{n,m} e^{i(\mathbf{K}-\mathbf{K}')\cdot(na\hat{\mathbf{u}}_x + mb\hat{\mathbf{u}}_y)} \tag{8.34}$$

It may be shown that:

$$\sum_{n,m} e^{i(\mathbf{K}-\mathbf{K}')\cdot\mathbf{r}_{nm}} = \sum_{n} e^{i(K_x - K'_x)an} \sum_{m} e^{i(K_y - K'_y)bm} \tag{8.35}$$

$$= \frac{(2\pi)^2}{ab} \sum_{n,m} \delta\left(K'_x - \left[K_x + \frac{2\pi n}{a}\right]\right) \delta\left(K'_y - \left[K_y + \frac{2\pi m}{b}\right]\right) \tag{8.36}$$

, and:

$$\bar{\bar{\mathbb{G}}}(\mathbf{r})\mathbf{p}_i = \frac{1}{ab} \sum_{n,m} \{\bar{\bar{\mathbf{g}}}(\mathbf{K} + \mathbf{K}_{nm}, z, z_i)\mathbf{p}_i\} e^{i(\mathbf{K}+\mathbf{K}_{nm})\cdot(\mathbf{r}-\mathbf{r}_i)} \tag{8.37}$$

, where the sum runs over the diffracted modes. Finally we have:

$$\mathbf{E}_{\text{scatt}} = \sum_i \frac{k^2}{\varepsilon_m \varepsilon_0} \bar{\bar{\mathbb{G}}}(\mathbf{r})\mathbf{p}_i = \frac{1}{\varepsilon_m \varepsilon_0} \frac{k^2}{ab} \sum_i \sum_{n,m} \{\bar{\bar{\mathbf{g}}}(\mathbf{K} + \mathbf{K}_{nm}, z, z_i)\mathbf{p}_i\} e^{i(\mathbf{K}+\mathbf{K}_{nm})\cdot(\mathbf{r}-\mathbf{r}_i)} \tag{8.38}$$

Equation (8.38) gives the electric field everywhere (except in the small volumes around $\mathbf{r} = \mathbf{r}_i + na\hat{\mathbf{u}}_x + mb\hat{\mathbf{u}}_y$) once we know the electric dipoles $\mathbf{p}_i$.

The solution for the Green tensor in the region z, $z_0 < 0$ is simply given by the sum of incident and reflected waves (see Equation (8.23)):

$$\begin{aligned}
\bar{\bar{\mathbf{g}}}(\mathbf{K}, z, z_0)\mathbf{p} &= \bar{\bar{\mathbf{g}}}^{(0)}(\mathbf{K}, z, z_0)\mathbf{p} + \bar{\bar{\mathbf{g}}}_{\mathrm{B,surf}}(\mathbf{K}, z, z_0)\mathbf{p} \\
&= k^2 \left\{ \frac{i}{2\gamma} e^{i\gamma|z-z_0|} \right\} \left\{ (\mathbf{p} \cdot \hat{\mathbf{s}})\hat{\mathbf{s}} + (\mathbf{p} \cdot \hat{\mathbf{p}}^{\pm})\hat{\mathbf{p}}^{\pm} \right\} \\
&+ k^2 \left\{ \frac{i}{2\gamma} e^{-i\gamma(z+z_0)} \right\} \left\{ \left[R_{ss}(\mathbf{p} \cdot \hat{\mathbf{s}}) + R_{sp}(\mathbf{p} \cdot \hat{\mathbf{p}}^{+}) \right] \right\} \hat{\mathbf{s}} \\
&+ k^2 \left\{ \frac{i}{2\gamma} e^{-i\gamma(z+z_0)} \right\} \left\{ \left[R_{ps}(\mathbf{p} \cdot \hat{\mathbf{s}}) + R_{pp}(\mathbf{p} \cdot \hat{\mathbf{p}}^{+}) \right] \right\} \hat{\mathbf{p}}^{-}
\end{aligned} \tag{8.39}$$

8.3.4 *Image dipole approximation*

The problem of dipole radiation in or near planar layered media is of significance to many fields of study. It is encountered in antenna theory, single molecule spectroscopy, cavity quantum electrodynamics, integrated optics, circuit design (microstrips) and surface contamination control. In his original paper [67], in 1909, Sommerfeld developed a theory for a radiating dipole oriented vertically above a planar and lossy ground. He found two different asymptotic solutions: space waves (spherical waves) and surface waves. The later had already been investigated by Zenneck [148]. At first glance, the calculation of the field (free space Green's tensor) possesses a simple mathematical description, and the planar interfaces have reduced dimensionality. Furthermore, the planar interfaces are constant coordinate surfaces for different coordinate systems. It is therefore very astonishing that there is no closed solution for this elementary problem, not even for the vertically oriented dipole which has a perfect rotational symmetry. The desired simplicity is only obtained for limiting cases, such as ideally conducting interfaces or the quasi-static limit.

The computational effort can be considerably reduced if retardation is neglected. In this case the fields will still satisfy Maxwell's equations in both half-spaces, but the standard static image theory is applied to approximately match the boundary conditions. We will outline the principle of this approximation for a single interface. Since the electromagnetic field is considered in its static limit ($k \to 0$) the electric and magnetic fields are decoupled and can be treated separately. For simplicity, only the electric field is considered.

Figure 8.3 shows an arbitrary oriented dipole above a planar interface and its induced dipole in the medium below. The distance of the image dipole to the interface is the same as for the primary dipole. However, the magnitude of the image dipole moment is different.

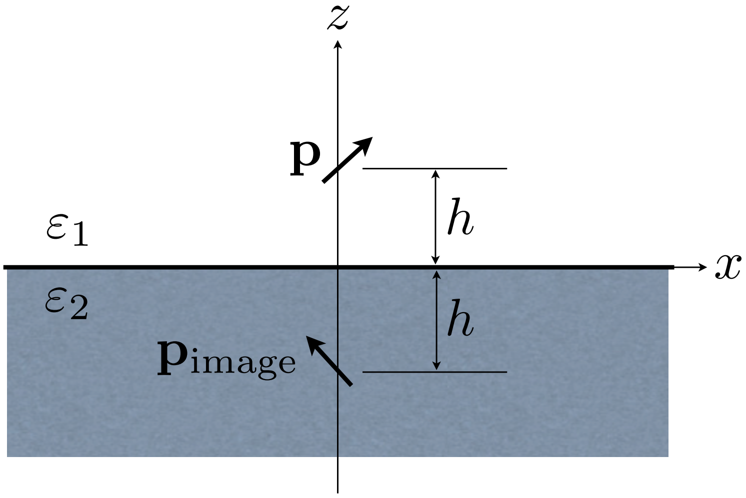

Figure 8.3: Principle of the image dipole approximation. $\mathbf{p}$ and $\mathbf{p}_{\text{image}}$ denote the primary dipole and the image dipole, respectively. Static image theory is applied to determine the magnitude of $\mathbf{p}_{\text{image}}$.

The static electric field of the primary dipole in the upper-half-space reads as:

$$\mathbf{E}_{\text{prim}} = -\nabla\phi, \qquad \text{with} \qquad \phi(\mathbf{r}) = \frac{1}{4\pi\varepsilon_1\varepsilon_0}\frac{\mathbf{p}\cdot\mathbf{r}}{r^3} \tag{8.40}$$

The vector $\mathbf{r}$ denotes the radial vector measured from the position of the primary dipole and r is its magnitude. Similarly, the corresponding radial vector of the image dipole is denoted by $\mathbf{r}'$. For simplicity, the dipole moment $\mathbf{p}$ is decomposed into its parallel and vertical parts with respect to the planar interface. Without loss of generality, the parallel component is assumed to point in the x-direction:

$$\mathbf{p} = p_x\mathbf{n}_x + p_z\mathbf{n}_z \tag{8.41}$$

, where $\mathbf{n}_x$ and $\mathbf{n}_z$ denote the unit vectors in the $x-$ and $z-$directions, respectively. In the following, the electric field will be considered for each of the two major orientations separately.

8.3.4.1 *Vertical dipole*

For a dipole $\mathbf{p} = p_z\mathbf{n}_z$, the evaluation of the primary electric field in Equation (8.40) in cartesian coordinates leads to:

$$\mathbf{E}_{\text{prim}} = \frac{p_z}{4\pi\varepsilon_1\varepsilon_0}\left[\frac{3x(z-h)}{r^5}, \frac{3y(z-h)}{r^5}, \frac{3(z-h)^2}{r^5} - \frac{1}{r^3}\right] \tag{8.42}$$

, where h is the height of the dipole above the interface. Assuming an image dipole $\mathbf{p} = p_z \mathbf{n}_z$, a similar expression can be derived for the image field $\mathbf{E}_{\text{image}}$:

$$\mathbf{E}_{\text{image}} = \frac{p_z}{4\pi\varepsilon_1\varepsilon_0}\left[\frac{3x(z+h)}{r'^5}, \frac{3y(z+h)}{r'^5}, \frac{3(z+h)^2}{r'^5} - \frac{1}{r'^3}\right] \tag{8.43}$$

, where r' denotes the radial distance measured from the location of the image dipole. A reasonable ansatz for the total field $\mathbf{E}$ in either of the two half-spaces is:

$$\mathbf{E} = \begin{cases} \mathbf{E}_{\text{prim}} + A_\nu \mathbf{E}_{\text{image}} & z > 0 \\ B_\nu \mathbf{E}_{\text{prim}} & z < 0 \end{cases} \tag{8.44}$$

, with two unknown parameters A_ν and B_ν. By requiring the boundary conditions at the interface $z = 0$, A_ν and B_ν can be determined as:

$$A_\nu = \frac{\varepsilon_2 - \varepsilon_1}{\varepsilon_2 + \varepsilon_1} \tag{8.45}$$

$$B_\nu = \frac{\varepsilon_2}{\varepsilon_1}\frac{2\varepsilon_2}{\varepsilon_2 + \varepsilon_1} \tag{8.46}$$

A_ν and B_ν correspond to the Fresnel reflection and transmission coefficients in the quasi-static limit.

8.3.4.2 *Horizontal dipole*

The procedure for a dipole $\mathbf{p} = p_x \mathbf{n}_x$ is similar. The primary and the image fields turn out to be:

$$\mathbf{E}_{\text{prim}} = \frac{p_x}{4\pi\varepsilon_1\varepsilon_0}\left[\frac{3x^2}{r^5} - \frac{1}{r^3}, \frac{3xy}{r^5}, \frac{3x(z-h)}{r^5}\right] \tag{8.47}$$

$$\mathbf{E}_{\text{image}} = \frac{p_x}{4\pi\varepsilon_1\varepsilon_0}\left[\frac{3x^2}{r'^5} - \frac{1}{r'^3}, \frac{3xy}{r'^5}, \frac{3x(z+h)}{r'^5}\right] \tag{8.48}$$

The corresponding ansatz for the total field $\mathbf{E}$ in either of the two half-spaces is:

$$\mathbf{E} = \begin{cases} \mathbf{E}_{\text{prim}} + A_h \mathbf{E}_{\text{image}} & z > 0 \\ B_h \mathbf{E}_{\text{prim}} & z < 0 \end{cases} \tag{8.49}$$

As before, the unknown parameters A_h and B_h can be determined by the boundary conditions at $z = 0$ as:

$$A_h = -\frac{\varepsilon_2 - \varepsilon_1}{\varepsilon_2 + \varepsilon_1} \tag{8.50}$$

$$B_h = \frac{\varepsilon_2}{\varepsilon_1} \frac{2\varepsilon_2}{\varepsilon_2 + \varepsilon_1} \tag{8.51}$$

Except for the sign of A_h, these two parameters are identical to the parameters A_v, B_v calculated for the vertical dipole.

8.3.4.3 *Including retardation*

Using the parameters A_v, B_v, A_h and B_h the magnitude of the image dipole is:

$$\left|\mathbf{p}_{\text{image}}\right| = \frac{\varepsilon_2 - \varepsilon_1}{\varepsilon_2 + \varepsilon_1} |\mathbf{p}| \tag{8.52}$$

As indicated in Figure 8.3, the horizontal components of $\mathbf{p}_{\text{image}}$ and $\mathbf{p}$ point in different directions if their vertical components have the same direction. To obtain the static field in the upper half-space, the fields of the two dipoles $\mathbf{p}$ and $\mathbf{p}_{\text{image}}$ have to be superposed. The field in the lower half-space simply corresponds to the attenuated primary dipole field. The attenuation is given by the factor $2\varepsilon_2/(\varepsilon_1 + \varepsilon_2)$. Note that the dipoles are considered to be located in the same medium as the point of observation.

So far, the location, orientation and magnitude of the dipole moments $\mathbf{p}$ and $\mathbf{p}_{\text{image}}$ have been determined. In order to fulfill Maxwell's equations in both half-spaces, the static dipole fields are replaced by their non-retarded forms:

$$\mathbf{E} \sim [\nabla\nabla\cdot] \frac{\mathbf{p}}{r} \qquad \rightarrow \qquad \mathbf{E} \sim \left[k^2 + \nabla\nabla\cdot\right] \frac{\mathbf{p}}{r} e^{ikr} \tag{8.53}$$

Although this substitution rescues Maxwell's equations in both half-spaces it introduces a violation of the boundary conditions. The image dipole approximation therefore has obvious limitations. In order to keep the errors in bounds, the height h of the primary dipole must be small and the fields may only be evaluated in a limited range from the dipole location. In fact, the image dipole approximation leads to reasonable accuracy as long as short-range interactions are considered.

8.4 QUANTUM EFFECTS IN SMALL METAL NANOPARTICLES

The remarkable growth of nanotechnology has been driven by the ability to alter material properties as dimensions are reduced towards the atomic scale. Nanomaterials exhibit physical and chemical properties very different from those of their bulk counterparts, often resulting from enhanced surface interactions or quantum confinement.

Therefore, the plasmonic properties of particles in the quantum size regime (radii below 10 nm) have recently received a renewed attention [149], fueled by the race of technologies towards the low nano-scale domain. For instance, it has been shown that cancer treatments based on delivering drugs using nanoparticles (NPs) with radii below 10 nm showed better antitumour efficiency than those using larger particles [150].

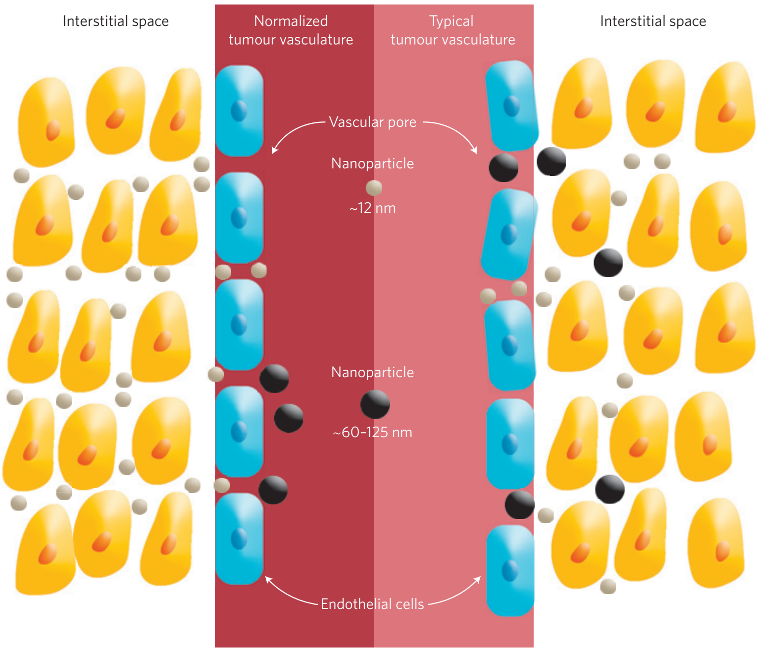

Figure 8.4: Size-dependent transport of nanotherapeutics. The blood vessels in a typical tumour contain pores of various sizes, which allow nanoparticles of different sizes (black and grey) to enter the tumour (right). However, these pores also cause the interstitial fluid pressure to increase, which limits convective transport of nanoparticles into the tumour. Decreasing the size of these pores (a process called vascular normalization) increases convection and the interstitial penetration of small ($\sim 12\,\mathrm{nm}$) nanotherapeutics (left). However, for larger nanoparticles ($\sim 60 - 125\,\mathrm{nm}$) this increase in convection is overridden by an increase in steric and hydrodynamic hindrances. Reprinted by permission from Macmillan Publishers Ltd [150].

But the scale reduction demands a better approach to the plasmonic behavior of NPs, because localized surface plasmon resonances (LSPRs) become more sensitive to the quantum nature of the conduction electrons.

Concerning the interaction between metallic NPs, it has also attracted a good deal of interest for the past ten years. The physics of this interaction is rich and opens nice perspectives for applications, such as single molecule detection [51, 151], solar cells [152], or high harmonic generation [153]. Although the plasmon hybridization model [154] is an elegant physical picture of this interaction, in order to properly calculate the optical response of a dimer, numerical simulations are still needed.

Here, we examine the plasmonic properties of both individual nanospheres and dimers made of silver and gold, with radii ranging from 10 to 1 nm, extending from the classically described regime to the quantum size regime. For all dimer cases, the minimum gap considered has been $l_{gap} = 1\,\mathrm{nm}$. Very recently, Esteban et al. [155] and Savage et al. [156] have successfully described the coupling across sub-nanometer gaps with a quantum-corrected model that includes electron tunneling and tunneling resistivity at the gap. According to Fig. 2 from [155], the electron tunneling transmission vanishes when the gap is larger than $\approx 8\,\text{Å}$. Then, from 1 nm on, quantum corrections are required due to the size of the particles only. We have studied the spectral extinction cross-section by using the T-matrix method [157, 158], one of the most powerful and widely used tools for accurately computing light scattering by nonspherical particles, both single and aggregated, based on directly solving Maxwell's equations.

8.4.1 *Infinite spherical well model*

To model the optical properties of quantum-sized plasmonic particles, a revised expression for the permittivity is required. In our analysis, the standard Drude model is recast with Lorentzian terms that are defined quantum mechanically (QM), based on fundamental physical phenomena. Classically, Lorentzian terms can be added to the Drude expression to account for the nearly-free nature of electrons in the bulk metal. These terms include a set of oscillator resonance frequencies and corresponding weighted strengths unique to each material [159]. Here, rather than using Lorentzians to fit the bulk data [160, 161], we employ them to explain the changing dielectric function as particle diameter decreases to the quantum size regime. As will be shown, the nature of the Lorentzian terms is based on fundamental physical phenomena, such as electron transition frequencies and oscillator strengths.

Following the example of Genzel et al. [162] and Kraus and Schatz [163], the relevant conduction electrons are treated as a free electron gas constrained by infinite potential barriers at the physical edges of the particle. Transition frequencies correspond to the allowed quantum energies of conduction electron transitions from occupied states i within the k-space Fermi sphere to unoccupied states f immediately outside.

The overall permittivity expression can then be described as follows:

$$\varepsilon(\omega) = \varepsilon_{IB} + \omega_p^2 \sum_i \sum_f \frac{S_{if}}{\omega_{if}^2 - \omega^2 - i\gamma\omega} \tag{8.54}$$

ε_{IB} is a frequency-dependent correction term to account for the contribution of the d-band valence electrons to interband transitions at higher energies. It is constant with particle diameter over the size range of this model, as validated in the literature [164]. Here, this additional corrective term was fit to the imaginary portion of the literature permittivity data [87]. The corresponding correction to the real portion of the permittivity was calculated through Kramers-Kronig consistency [8].

The plasma frequency, ω_p, is defined as:

$$\omega_p = \sqrt{\frac{n_e e^2}{\varepsilon_0 M}} \tag{8.55}$$

where n_e is the volumetric conduction electron density (given 1 electron per atom), e is the elementary charge, ε_0 is the permittivity of free space, and M is the mass of the electron. At frequencies below ω_p ($9.01\,\text{eV}/\hbar$ for silver [149] and $9.0\,\text{eV}/\hbar$ for gold [165]), a free-electron metal can effectively screen the incident electromagnetic radiation and acts in a reflective manner, but above the plasma frequency, the metal becomes transparent and acts as a dielectric.

The scattering frequency γ is dependent on the nanosphere dimension through the following relation:

$$\gamma = \gamma_{\text{bulk}} + \frac{A v_F}{R} \tag{8.56}$$

where γ_{bulk} is an empirical constant for each material ($0.016\,\text{eV}/\hbar$ for silver [149] and $0.07\,\text{eV}/\hbar$ for gold [165]), R is the particle radius, and v_F is the Fermi velocity of electrons ($\approx 1.4 \times 10^6\,\text{m/s}$ for both silver [166] and gold [165]). A is a fitting coefficient whose value has varied in the literature from 0.1 to 2, depending on the model and experimental system [167–170]. Here, we use $A = 0.25$, a value based on both single particle experiments and *ab initio* calculations [164, 165].

The frequency of electron transitions from occupied to excited states can be described as:

$$\omega_{if} = \frac{E_f - E_i}{\hbar} \tag{8.57}$$

, where the energy levels E_f and E_i depend on the geometry and potential of the system. We assume that the nanocrystal's physical shape closely approximates a sphere and treat the conduction electrons as particles in an infinite spherical well. The Schrödinger equation for a free particle in spherical coordinates has the well known solutions:

$$\psi(r,\theta,\phi) = j_l(kr) Y_{lm}(\theta,\phi) \tag{8.58}$$

, where:

$$k^2 = \frac{2mE}{\hbar^2} \tag{8.59}$$

Applying the boundary condition $j_l(kR) = 0$, it may be shown that the allowed energies are given by:

$$E_{nl} = \frac{\hbar^2}{2MR^2}\beta^2_{n,l} \tag{8.60}$$

, where M is the mass of the electron, R is the radius of the sphere, n and l are the principle and azimuthal quantum numbers, respectively, and $\beta_{n,l} = k_{nl}R$ denotes the nth zero of the lth spherical Bessel function.

Since we are interested in the large energy limit we can use the asymptotic form of the spherical Bessel functions:

$$j_l(kr) = \frac{\cos\left[kr - \frac{\pi}{2}(l+1)\right]}{kr} \tag{8.61}$$

and write the allowed energies as:

$$E = \frac{\hbar^2\pi^2}{8MR^2}(2n+l+2)^2 \tag{8.62}$$

Figure 8.5 shows the comparison between the exact numerical value for the energies, as given by Equation (8.60), and the approximate analytical solution found in Equation (8.62). As can be seen, the approximate solution provides very accurate results even for small values of both n and l.

If we define the excited states' orbital numbers as $n_f = n + \Delta n$ and $l_f = l + \Delta l$, the the transition frequencies can be expressed as:

$$\omega_{if} = \frac{\hbar\pi^2}{8MR^2}(4n + 2\Delta n + 2l + \Delta l + 4)(2\Delta n + \Delta l) \tag{8.63}$$

The relative weight of each of these transitions is given by their oscillator strength terms. As dictated by the Thomas-Reiche-Kuhn sum rules, these terms sum to unity and can be described using the standard quantum harmonic oscillator definition:

$$S_{if} = \frac{2M\omega_{if}}{\hbar N}| < f|z|i > |^2 \tag{8.64}$$

, where N is the number of conduction electrons in the nanosphere. After additional simplification and degeneracy considerations described

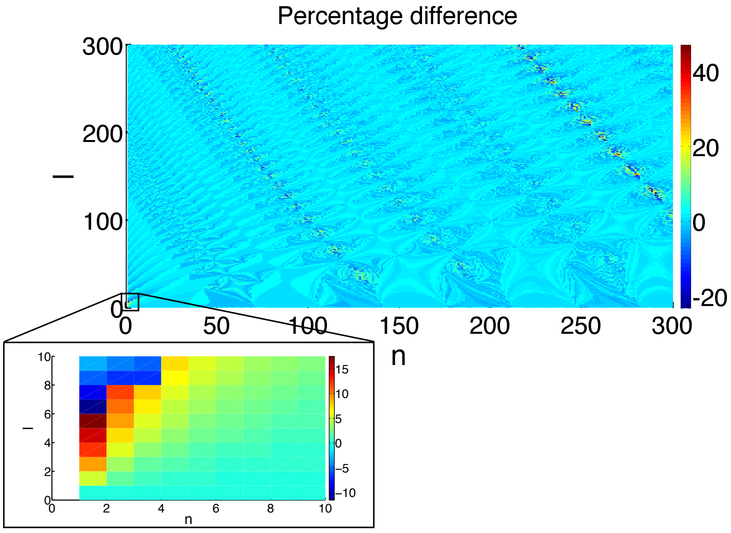

Figure 8.5: Percentage difference between the exact numerical solution given by Equation (8.60), and the approximate analytical solution found in Equation (8.62). The inset just shows a detailed zoomed area.

elsewhere [162], the final expression for the oscillator strength is given as:

$$
\begin{aligned}
S_{if} \equiv S_{n,l,\Delta n,\Delta l} &= \delta_{\Delta l,-1} \frac{16 l (2n+2\Delta n+l+1)^2 (2n+l+2)^2}{\pi^2 n_F^3 (4n+2\Delta n+2l+3)^3 (2\Delta n-1)^3} \\
&+ \delta_{\Delta l,+1} \frac{16 (l+1)(2n+2\Delta n+l+3)^2 (2n+l+2)^2}{\pi^2 n_F^3 (4n+2\Delta n+2l+5)^3 (2\Delta n+1)^3}
\end{aligned}
\tag{8.65}
$$

, where n_F is the value of the quantum number n on the Fermi surface when $l = 0$. The magnetic quantum number m, has already been incorporated into the terms and acts as a multiplicative degeneracy factor.

Using Equations (8.55), (8.56), (8.63) and (8.65), the overall permittivity can be described by evaluating Equation (8.54) over the following ranges, as described elsewhere [162]:

$$
\begin{aligned}
\Delta l &= -1, 1 \\
\frac{1-\Delta l}{2} &\leqslant \Delta n \leqslant n_F \\
0 \leqslant n &\leqslant n_F - \frac{1-\Delta l}{2} \\
2(n_F - n - \Delta n + \frac{1-\Delta l}{2}) &\leqslant l \leqslant 2(n_F - n)
\end{aligned}
\tag{8.66}
$$

Figure 8.6 shows the real and imaginary parts of the QM corrected relative electric permittivity calculated with Equation (8.54) as a function of both the incident energy E (resonance range) and the particle radius R for a silver nanosphere.

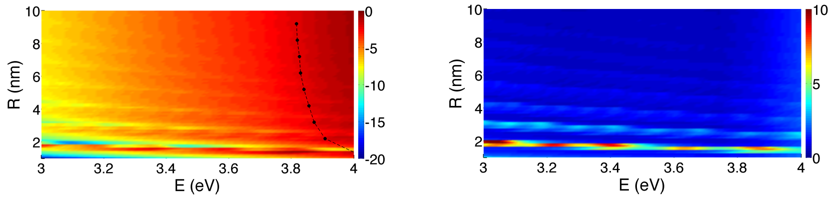

(a) Real part. The black dots represent the resonance position (where $\Re\{\varepsilon\} = -2$).

(b) Imaginary part.

Figure 8.6: QM corrected relative electric permittivity as a function of both the incident energy (resonance range) and the particle radius for silver.

8.4.2 *Convergence to bulk regime*

Figure 8.7 shows the real and imaginary parts of the relative electric permittivity of silver as we increase the particle radius, for three different energies of the incident radiation. The values of the electric permittivity have been calculated following Equation (8.54). A clear convergence to the bulk values (Johnson and Christy [87] and Palik [171]) is observed. The inset of Figure 8.7 clearly shows how at $R = 10\,\text{nm}$ the QM corrected results already converge to bulk results, except for the remain of a small bump belonging to the series of period $\approx 2\,\text{nm}$.

8.4.3 *Main results*

We now focus on single particles as well as dimers of radius $R = 4\,\text{nm}$, made of silver and gold. The dimers are aligned with the incident electric field in all cases. Figure 8.8 shows the spectral extinction efficiency (cross-section normalized by the total geometric section) for these systems, calculated with both bulk and QM corrected optical properties. The most remarkable feature of the spectral dependence of Q_{ext} shown in Figure 8.8 is the fact that, when including QM corrections, resonances shift to smaller wavelengths (blueshift [149]) and also become weaker (lower peaks). The redshift and the peak increment of the dimer resonance with respect to the isolated particle persist in the QM results.

In Figure 8.9 we have plotted the spectral relative electric permittivity ($\varepsilon = \varepsilon_r + i\varepsilon_i$) corresponding to the case of a particle with radius $R = 4\,\text{nm}$, for both silver and gold. As can be seen, in the case of silver, Figure 8.9a, the QM corrected real part of ε intercepts $\varepsilon_r = -2$ at smaller wavelengths than the bulk results, thus producing a blueshift of the resonant condition. In the case of gold, Figure 8.9b, the QM corrected ε does not even intercept $\varepsilon_r = -2$, thus we do not see any resonance peak in Figure 8.8b.

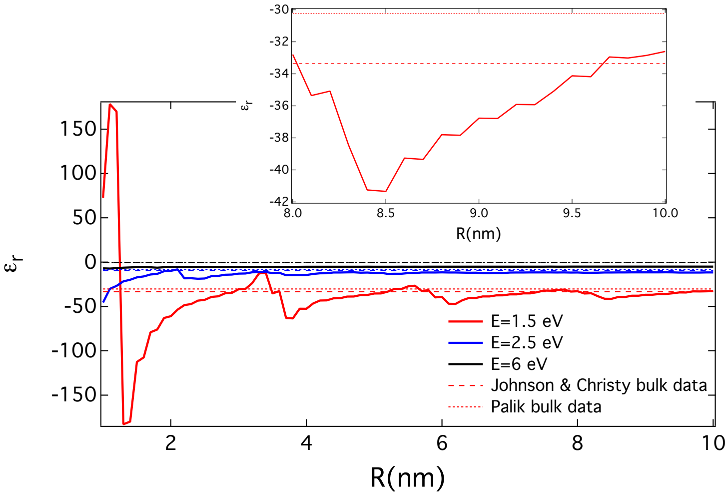

(a) Real part.

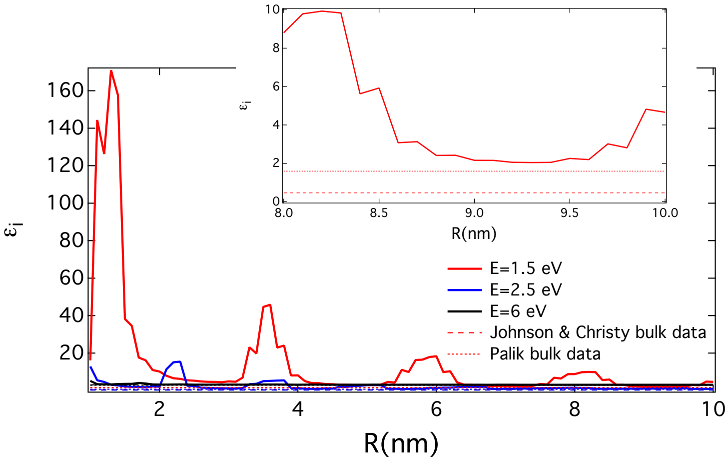

(b) Imaginary part.

Figure 8.7: Relative electric permittivity of silver as a function of the particle radius for three different energies. Bulk values taken from Johnson and Christy [87] as well as Palik [171] are also shown. The insets show zoomed areas between $R = 8\,\text{nm}$ and $R = 10\,\text{nm}$.

On the other hand, the QM corrected imaginary part of ε is greater than the bulk one for all wavelengths, for both silver and gold. For sufficiently small x, the extinction efficiency equals the absorption, as the scattering may be considered zero [8]:

$$Q_{\text{ext}} \equiv Q_{\text{abs}} = 4x\Im\left\{\frac{\varepsilon - 1}{\varepsilon + 2}\right\} \tag{8.67}$$

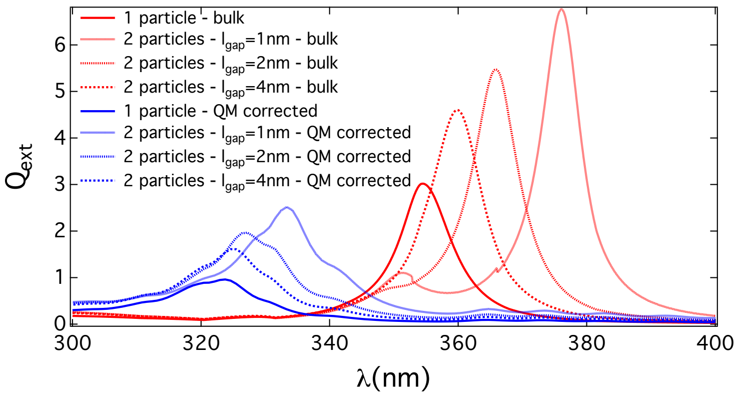

(a) Silver.

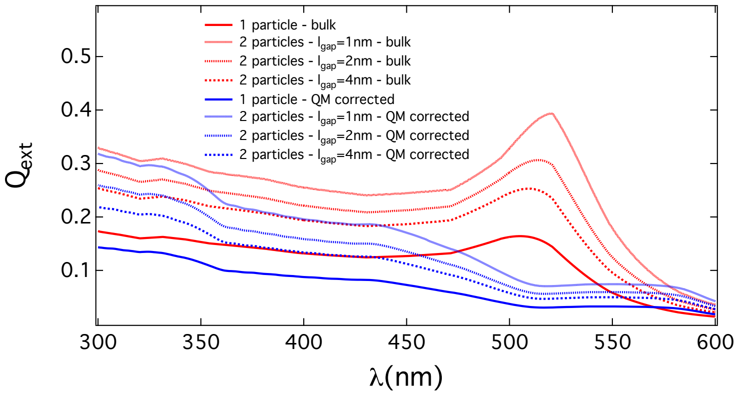

(b) Gold.

Figure 8.8: Spectral extinction efficiency for both single particles and dimers of radius $R = 4\text{nm}$, calculated with both bulk and QM corrected optical properties.

, where $x = 2\pi R/\lambda$ is the size parameter, $\Im$ denotes the imaginary part and $\varepsilon = \varepsilon_r + i\varepsilon_i$ is the relative electric permittivity. In the resonance condition ($\varepsilon_r = -2$), Equation (8.67) becomes:

$$Q_{ext} \equiv Q_{abs} = \frac{12x}{\varepsilon_i} \tag{8.68}$$

According to Equation (8.68), the greater the imaginary part, the lower the extinction. Figure 8.10 shows the extinction efficiency for a resonant ($\varepsilon_r = -2$) isolated sphere, varying both the size parameter x and the imaginary part of the electric permittivity ε_i, calculated with the Mie theory. It can be seen that, for sufficiently small x, the extinction efficiency (and therefore the absorption efficiency as well) decreases as we increase the imaginary part of the electric permittivity. This has been reported in the literature as *anomalous absorption* [172], and accounts for the reduction of the peaks.

As a result, it is reasonable to think that two particles close to each other with quantum corrected optical properties will interact less, so

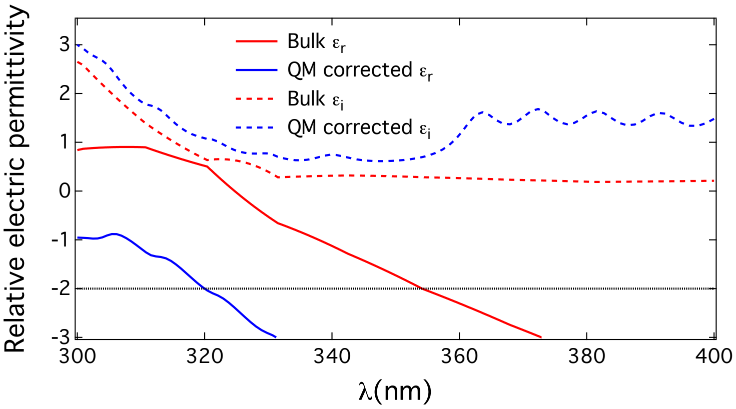

(a) Silver.

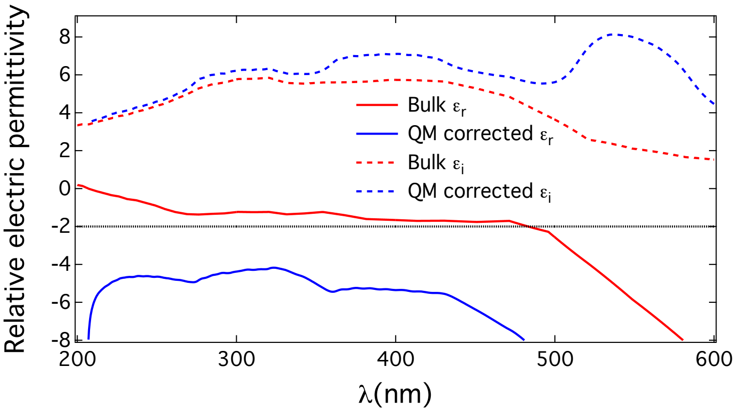

(b) Gold.

Figure 8.9: Spectral real and imaginary parts of the relative electric permittivity for the case $R = 4\,\mathrm{nm}$. Both bulk and QM corrected values are shown.

that the associated redshifts and peak increments with respect to the isolated case will be smaller, as shown in Figure 8.11. Once again, the case of gold (Figure 8.11b) is especially notorious, since the QM correction quenches the plasmonic resonance and no redshift is observed.

As a summary, the introduction of QM corrected optical properties becomes in blueshifted [149] and weaker resonances as shown in Figure 8.8. The shifting arises as a consequence of the interception of the real part of the relative electric permittivity with $\varepsilon_r = -2$ (see Figure 8.9). On the other hand, the weakening of the resonances is due to the greater imaginary part of the relative electric permittivity when considering quantum corrections (see Figure 8.9). According to Equation (8.68), the greater the imaginary part, the lower the extinction. The case of silver allows us to test our calculations, while the case of gold shows how important these quantum considerations may be when treating very small particles close to resonance. As a direct consequence, two particles close to each other with quantum

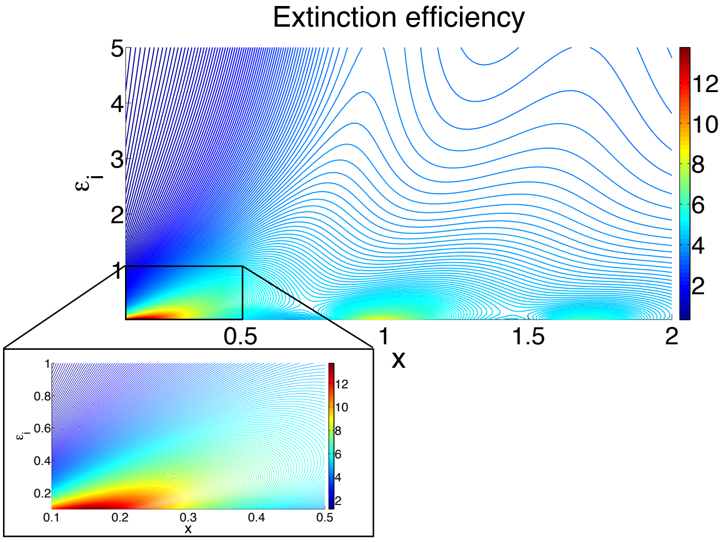

Figure 8.10: Extinction efficiency for a resonant ($\epsilon_r = -2$) isolated sphere, varying both the size parameter x and the imaginary part of the electric permittivity ϵ_i, calculated with the Mie theory.

corrected optical properties interact less, therefore producing smaller shifts and lower peak increments in the far-field cross-sections, as corroborated by Figure 8.11.

8.5 A STUDY OF METAL NANOSHELLS

The manipulation of purpose-built metallic nanoparticles (NPs) has achieved a great level of accuracy in the last years [173]. The special case of nanoshells has been widely studied [174], in part due to its numerous applications in biomedicine, ranging from high-resolution tumor imaging (in the case of scattered light), to cancer therapy (this time the absorbed light causes cell death in tumors). In particular, nanoshells can be designed to interact with some desired light wavelengths, making them very useful for detection and treating of cancerous cells [175]. In addition, the core-shell system is, by itself, a useful description of a particle under the influence of a nearby surrounding medium, an element of great interest in the simulation of many systems.

8.5.1 *Linear polarization degree*

In the scattering plane, defined by the incident and observation directions, the linear polarization degree of the scattered light, $P_L(\theta)$, is defined as:

$$P_L(\theta) = \frac{I_s(\theta) - I_p(\theta)}{I_s(\theta) + I_p(\theta)} \tag{8.69}$$

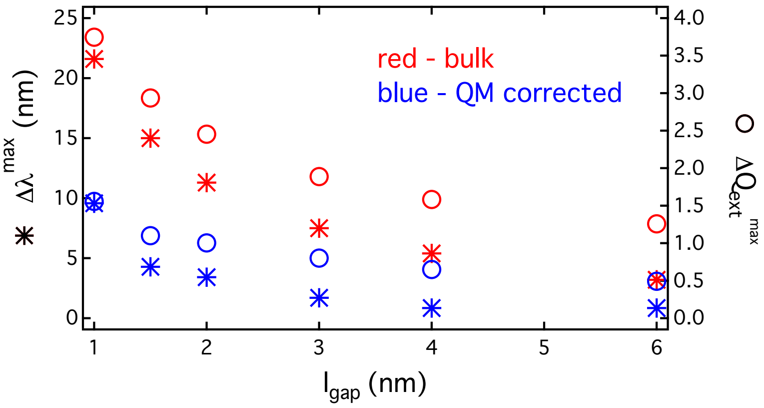

(a) Silver.

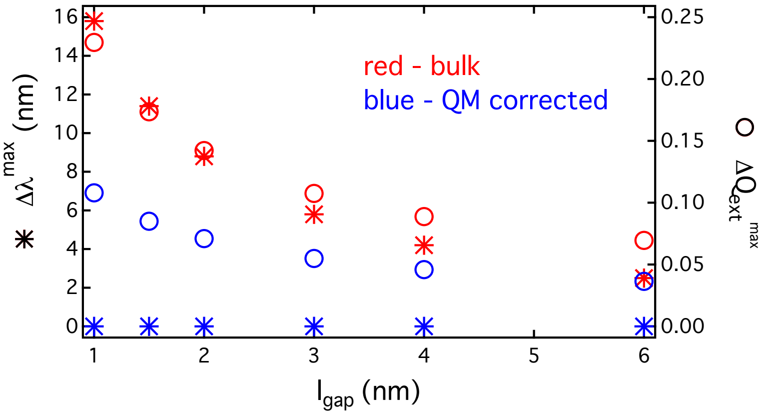

(b) Gold.

Figure 8.11: Spectral shift (left axis, '∗' symbol) and peak increment (right axis, 'o' symbol) of the spectral extinction resonance shown in Figure 8.8 as a function of the dimer gap l_{gap}. $\Delta\lambda^{max}$ and ΔQ_{ext}^{max} represent the difference with respect to the isolated particle case.

, where $I_s(\theta)$ and $I_p(\theta)$ are the scattered intensities with polarization perpendicular or parallel to the scattering plane, respectively, as shown in Figure 8.12. Extreme cases occur when only I_s is present ($P_L = +1$) or when we only have I_p ($P_L = -1$). Because of this definition, these two magnitudes are not distinguishable at $\theta = 0°$ or $\theta = 180°$ (forward and backward scattering, respectively), therefore producing values of $P_L(0°) = P_L(180°) = 0$. However, its value for other observation angles may carry interesting information. For instance, for isotropic dipole-like particles, it can be shown that the scattered intensity at right-angle contains only perpendicular component, i.e. $I_p(90°) = 0$, thus the linear polarization degree equals 1. For larger particles, however, multipolar orders cause the $I_p(90°)$ to be different from zero, and so the linear polarization degree at right-angle no longer equals 1. In general, deviations from 1 in the linear polarization degree at right-angle are caused by non-dipole-like behaviors.

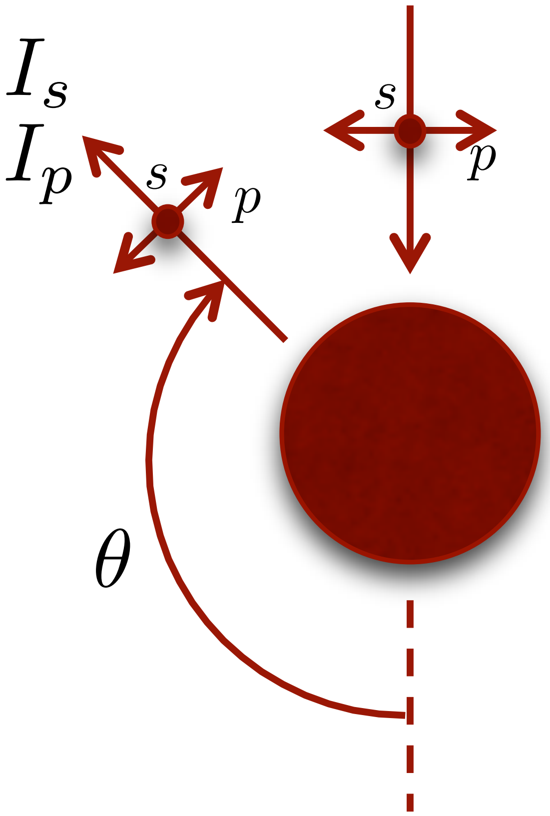

Figure 8.12: Sketch of a typical experimental setup used to measure the scattered light either with polarization perpendicular (s) or parallel (p) to the scattering plane.

In their work, Setién et al. [176] showed how the linear polarization degree measured at right angle, $P_L(90°)$, was very sensitive to changes in the NP size, finding that the spectral position of the dipolar resonance redshifts clearly as the size of the NP is increased. Besides, a quadrupolar peak appears when increasing the NP size (with almost no shift). Interestingly, the P_L minima positions are coincident with the quadrupolar peak positions, as shown in Figure 8.13.

In the same work [176], Setién et al. studied a more complex situation: the case of two interacting NPs (e.g. a dimer). In this case, both the quadrupolar behavior and the interaction of the NPs caused the appearance of more peaks in the $P_L(90°)$, as shown in Figure 8.14.

8.5.2 *Analysis of the core variation*

In the following, it will be shown how this parameter, $P_L(90°)$, is also sensitive to changes in the core (radius and optical properties) of metal nanoshells (such as that shown in Figure 8.15), thus being useful for their setup and characterization.

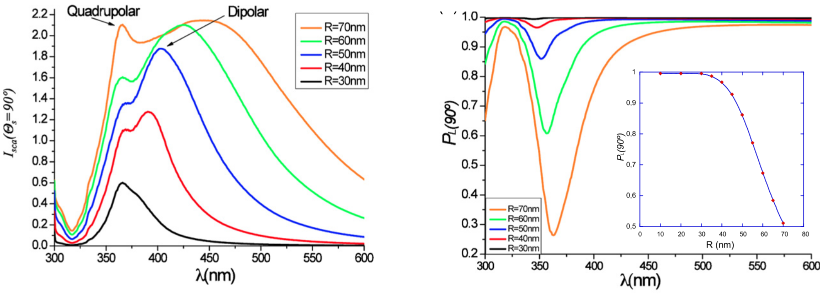

(a) Scattered intensity $I_{\text{sca}}(90^\circ)$.

(b) Linear polarization degree $P_L(90^\circ)$. The inset shows the evolution of the values of the minimum of the linear polarization degree, $P_L(90^\circ)$, as a function of particle size.

Figure 8.13: Spectral behavior of right-angle scattering magnitudes of a spherical silver particle as a function of the incident wavelength for several sizes. Taken from [176].

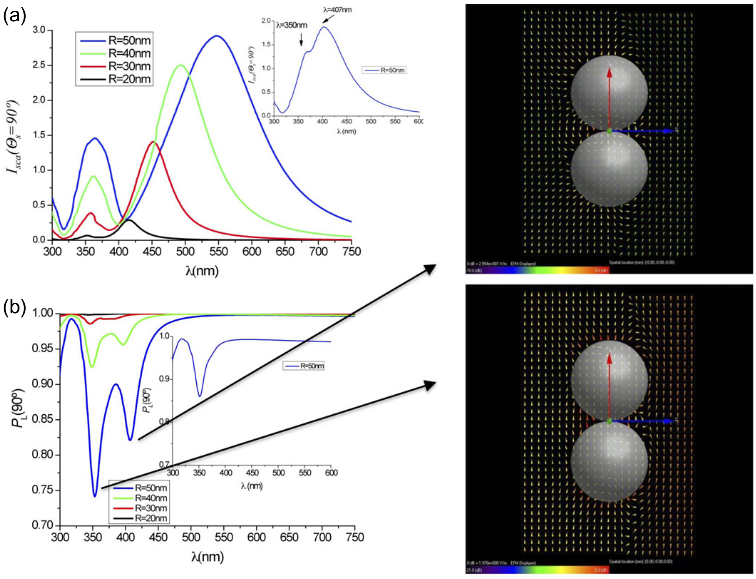

Figure 8.14: (a) Right-angle scattered intensity, $I_{\text{sca}}(90^\circ)$, and (b) right-angle linear polarization degree, $P_L(90^\circ)$, produced by a silver dimer of spherical particles as a function of the incident wavelength for several values of the particle radius. Inset of (a): spectrum of $I_{\text{sca}}(90^\circ)$ for an isolated silver NP of $R = 50\,\text{nm}$. Inset of (b): $P_L(90^\circ)$ for the isolated particle case. The two right figures show the near electric field distributions for $R = 50\,\text{nm}$ corresponding to the first and second minima of P_L in (b), as indicated by the black arrows. The incident beam is a plane wave linearly polarized parallel to the x-axis (in red) and propagating in the $-z$-direction (the z-direction corresponds to the blue axis). Taken from [176].

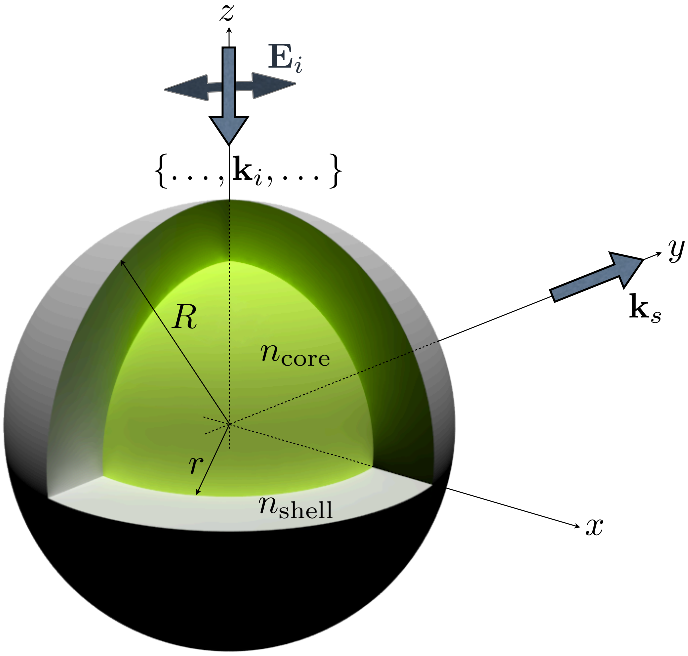

Figure 8.15: Sketch of an illuminated silver nanoshell. Shell: Ag, $R = 50\,\text{nm}$. The nanoshell is illuminated with polychromatic light linearly polarized at 45°. Then the scattered intensities I_s and I_p are calculated at $\theta = 90°$. This is not the unique configuration for a nanoshell. Alternative configurations (with applications in drug delivery) may have no metal at all.

The nanoshell is illuminated with polychromatic light linearly polarized at 45°, which, for our purpose, is equivalent to incidence with unpolarized light. The shell has a fixed outer radius of $R = 50\,\text{nm}$. For each incident wavelength, the scattered intensities with both polarizations are calculated using DDSCAT [82, 85]. The linear polarization degree can then be obtained using Equation (8.69).

We shall present a spectral analysis of silver nanoshells, varying both the radius and the refractive index of the core.

A. Varying the core radius

Figure 8.16a shows the spectral scattered intensity with perpendicular polarization calculated at right-angle, $I_s(90°)$, for several core radii r, with a fixed core refractive index $n_{\text{core}} = 2$, and external radius $R = 50\,\text{nm}$. As can be clearly seen, the main resonance peak reduces its height[3], and redshifts, as r increases. Moreover, a new resonance peak appears at lower wavelengths, almost not shifting at all as we vary the core radius.

The corresponding right-angle scattered intensity with parallel polarization, $I_p(90°)$, is shown in Figure 8.16b. The resonance

---

[3] Remember that in this configuration, increasing the core radius means reducing the metal thickness.

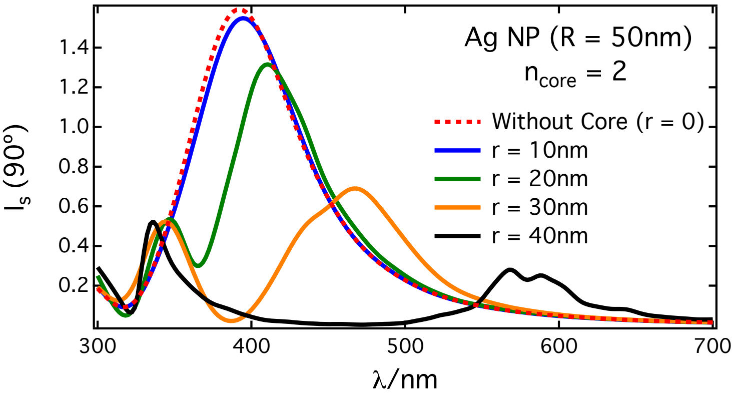

(a) $I_s(90°)$.

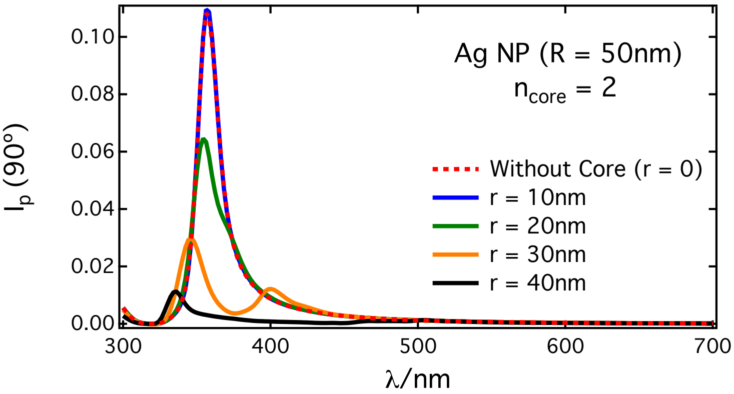

(b) $I_p(90°)$.

Figure 8.16: Spectral dependence of the scattered intensity calculated at right-angle, for several core radii, with a refractive index for the core $n_{core} = 2$.

peaks blueshift as r increases. Furthermore, the spectral position of these peaks almost coincides with the spectral position of the small peaks that appeared in $I_s(90°)$ (Figure 8.16a).

Figure 8.17 shows the spectral dependence of the linear polarization degree calculated at right-angle, $P_L(90°)$, for the conditions just described for Figure 8.16. It is clear that the $P_L(90°)$ minima depend on the core radius, not only their location in the spectrum but also their depth. Two important features are worthy a comment: as we increase the core radius (thinner shells), the minima become deeper and shift towards the red; besides, small core radius nanoshells behave mostly as a single NP (with deeper minima). From $r = 30\,\text{nm}$ on, the depth of the minimum saturates, while its spectral position is further modified. Though the behavior of these curves is directly derived from Figure 8.16, in Section 8.5.2.1 we will try to explain the origin of the minima, showing the scattered intensities in two particular cases.

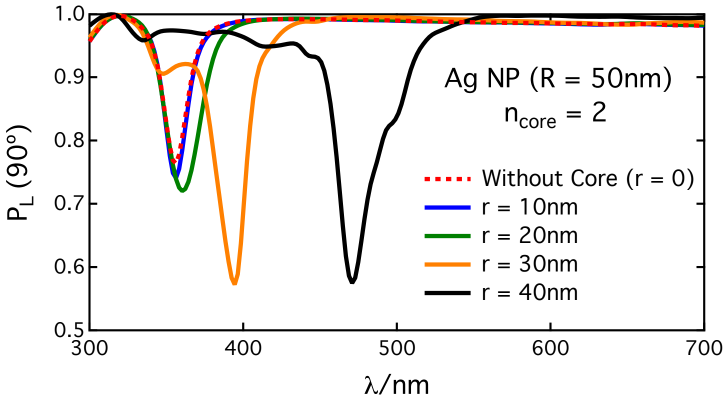

Figure 8.17: Spectral dependence of $P_L(90°)$ for several core radii, with a refractive index for the core $n_{core} = 2$.

B. Varying the core refractive index

Figure 8.18 shows the spectral dependence of $P_L(90°)$ for several core refractive indices, with a core radius $r = 40\,\text{nm}$.

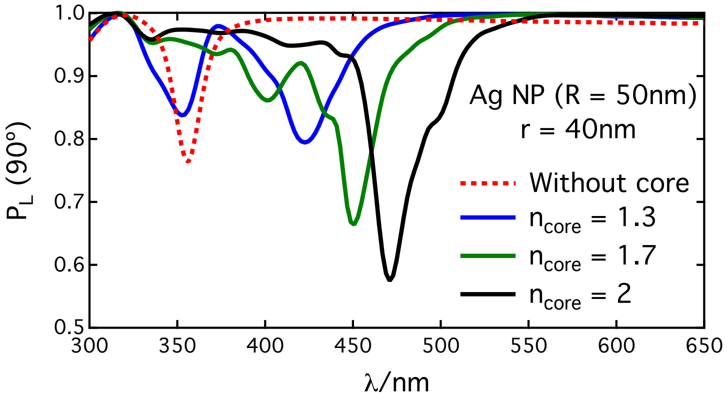

Figure 8.18: Spectral dependence of $P_L(90°)$ for several core refractive indices, with a core radius $r = 40\,\text{nm}$.

The situation here is more complex, with several local maxima and minima appearing. Nevertheless, the absolute minima of $P_L(90°)$ also become deeper and redshift when the core refractive index is increased. Interestingly, the depth of the minima does not saturate even for $n_{core} = 2$, as opposed to the case of varying the core radius (see Figure 8.17). Thus, $P_L(90°)$ gives information about the optical properties of the core as well.

8.5.2.1 *Scattered intensities I_s and I_p: two particular cases*

In order to understand the origin of the minima in the $P_L(90°)$, we show here the spectra of the scattered intensities $I_s(90°)$ and $I_p(90°)$ as well as $P_L(90°)$ for two particular cases. The first one, Figure 8.19, with a core radius $r = 10\,\text{nm}$, clearly shows a single minimum in $P_L(90°)$, due to a maximum in $I_p(90°)$ (quadrupolar behavior).

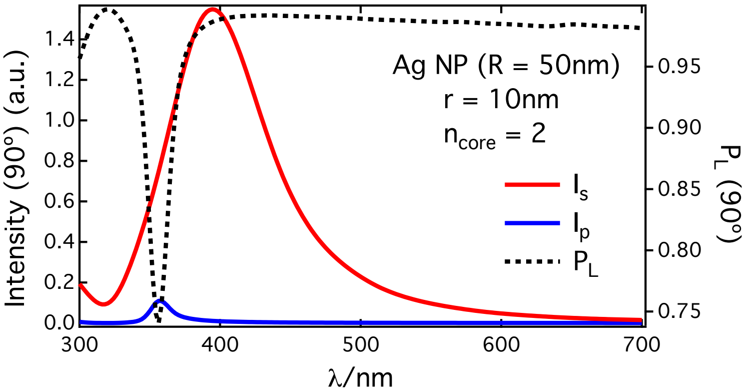

Figure 8.19: Spectral scattered intensities as well as linear polarization degree calculated at right-angle, for a silver nanoshell with $r = 10\,\text{nm}$ and $n_{\text{core}} = 2$.

The second case, Figure 8.20, with a larger core radius $r = 30\,\text{nm}$, shows two minima in $P_L(90°)$: the first one again due to a maximum in $I_p(90°)$ (quadrupolar behavior) and the second due to an inhibition of the dipolar resonance (minimum of $I_s(90°)$ with $I_p(90°)$ different from zero).

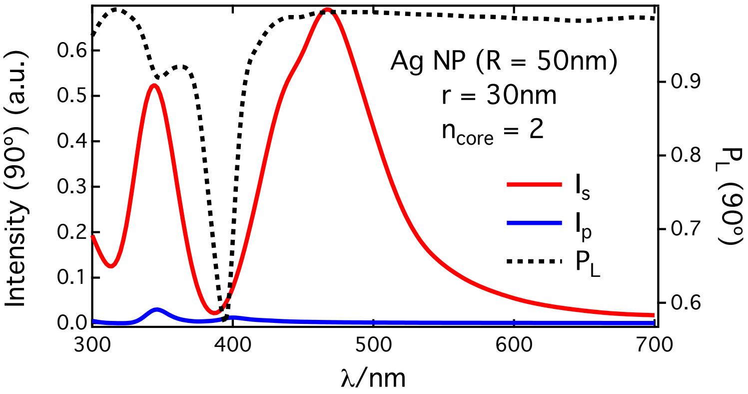

Figure 8.20: Spectral scattered intensities as well as linear polarization degree calculated at right-angle, for a silver nanoshell with $r = 30\,\text{nm}$ and $n_{\text{core}} = 2$.

8.5.3 *Conclusions*

The main conclusions that we can draw from this analysis is that $P_L(90°)$ is a sensitive parameter to characterize nanoshells, as it provides information about their geometric structure and their optical properties. The next step would involve studying more complex systems, such as nanocups, the influence of the surrounding medium, or even anisotropies (with the help of E-DDA [83]).

9

SUMMARY

As a summary, we can say that we have successfully subjected the E-DDA code to a set of tests in the nanometer range, producing self-consistent results that not only prove the reliability of the method but also extend the current domain of applicability of the Discrete Dipole Approximation.

9.1 FORMATIVE/TRAINING TASKS

The development of this work has involved carrying out several computational tasks as well as revising many relevant theories. Some of these tasks are detailed next:

APPROACHING THE PROBLEM As a means to implement a code capable of performing calculations based on DDA from scratch, both the theoretical formalism and numerical details of the Discrete Dipole Approximation needed to be reviewed. This has required a clear understanding of both the processes involved and their modeling conditions.

UNITS With respect to the systems of units, the fact that in electromagnetism there exist several systems of units, each with different expressions, has meant a serious issue when comparing theoretical expressions. This effort has produced the tables detailed in Appendix A.

FORTRAN 90 Without any doubt, the design and implementation of the software tool (E-DDA code), written in Fortran 90, has meant the greatest computational challenge that I have accomplished to date.

RESEARCH COMPETITION The generalization of the DDA to materials with arbitrary optical constants is currently a topic of great interest, with several groups trying to produce the definitive tool. During the development of this dissertation, I could feel this competition when papers related to the subject were published.

9.2 CONCLUSIONS ABOUT THE RESULTS

In this section, the most important conclusions about the results are briefly summarized.

9.2.1 *Validation of the E-DDA*

Both the symmetry and convergence tests allow us to check the self-consistency of our calculation method, proving the deployment of a tool with great potential. The E-DDA code has been tested against the well-proven DDSCAT, probably the most advanced DDA implementation to date, finding a very good agreement for a case where their applicability range overlap, such as a nanoshell system which includes inhomogeneities and presence of metallic and dielectric media.

9.2.2 *Magneto-optical materials*

The main conclusion one can draw from these results is the fact that the experimentally accessible $\Delta I/I$-ratio seems virtually unaffected by the geometric confinement of the disks, despite the remarkable size-induced differences that are found in the dipole moment distributions especially for sub-wavelength disks. We have shown that the insensitivity of the $\Delta I/I$-ratio to lateral confinement is a consequence of the close similarity of the optical and magneto-optical polarization patterns, irrespective of disk size, and of the fact that their contributions to the far-field intensity scale nearly in the same way.

9.2.3 *Composite materials*

We have resorted to our E-DDA code in order to compare several approaches to the analysis of the optical behavior of composite materials, starting with nanoscopic conventional objects in the visible domain. The Combined Approach that we propose clearly gives a better agreement with experimental results. We think that it is an advance in this kind of modeling, as it preserves the individual nature of the constituents and at the same time introduces a variation in the optical properties of a discrete element that is given by the properties of the surrounding medium. This is key in modeling any kind of composite material, admitting that handling macroscopic properties is only an approach to the exact solution of the electronic band structure of each particular discrete element.

9.2.4 *Additional aspects*

From the set of results presented in Chapter 8, probably the most important ones are those related to the analytical quantum mechanical model. We have seen that the introduction of QM corrected optical properties becomes in blueshifted [149] and weaker resonances as shown in Figure 8.8. The shifting arises as a consequence of the interception of the real part of the relative electric permittivity with

$\varepsilon_r = -2$ (see Figure 8.9). On the other hand, the weakening of the resonances is due to the greater imaginary part of the relative electric permittivity when considering quantum corrections (see Figure 8.9). The case of silver allows us to test our calculations, while the case of gold shows how important these quantum considerations may be when treating very small particles close to resonance. As a direct consequence, two particles close to each other with quantum corrected optical properties interact less, therefore producing smaller shifts and lower peak increments in the far-field cross-sections, as corroborated by Figure 8.11.

9.3 FUTURE PRESPECTIVES

Many promising aspects and ideas have arisen during these years' work. For obvious reasons, most of them cannot be properly addressed, but some still deserve future research and development, and are worth mentioning here.

Until very recently, there has been little work on ultraviolet (UV) plasmonics ($\lambda < 400\,\mathrm{nm}$), in part because of the challenge of making appropriately small nanostructures, in part because gold LSPRs do not extend into the ultraviolet. However, in response to an increasing demand to detect and recognize biological toxins [90, 177], to enhance biological imaging, and to characterize semiconductor devices at the nanometer scale, interest in UV plasmonics is growing [178–180]. Although the other popular plasmonic metal, silver, does have an LSPR that extends into the near UV, it cannot span the entire UV region ($200-400\,\mathrm{nm}$, or $3-6\,\mathrm{eV}$) [181]. It has been recognized for some time that aluminum might be a compelling metal for UV plasmonics because its bulk plasma frequency is $13\,\mathrm{eV}$ [178, 179, 182–184]. However, aluminium oxidizes even more rapidly than silver, a problem that introduces scientific and practical difficulties for implementing effective stable nanodevices.

Consequently, there is a need to explore other metals that might be nanostructured for use in UV plasmonics (with biocide or self-cleaning properties for example). The candidate is currently involved in a study to assess the efficacy of various metals for use in ultraviolet plasmonics as well as another study of quantum effects in small plasmonic particles in the UV-VIS range, comparing UV-candidate materials such as aluminum or gallium with silver and gold.

Materials showing electromagnetic properties that are not attainable in naturally occurring media, so-called metamaterials, have been lately, and still are, among the most active topics in optical and materials physics and engineering. Among these properties, one of the most attractive ones is the sub-diffraction resolving capability predicted for media having an index of refraction of -1. It has been recently shown [185] that fully three-dimensional, isotropic metamaterials with strong electric and magnetic responses in the optical regime can be realized, based on spherical metallo-dielectric core-shell nanospheres. The magnetic response stems from the lowest, magnetic-dipole resonance of the dielectric shell with a high refractive index, and can be tuned to coincide with the plasmon resonance of the metal core, responsible for the electric response. Investigating their scattering properties in connection with directionality and invisibility could be a very interesting future research line.

Dielectric nanostructures make a new twist on light scattering phenomena. Subwavelength particles made of high-dielectric materials exhibit very strong magnetic response, which has been recently demonstrated experimentally [186, 187]. Dielectric nanoparticles with strong magnetic response can be used as building blocks to explore new types of interactions at nanoscales. The lower losses, compared to plasmonic counterparts, allow to employ dielectric nanostructures for a variety of applications spanning from optical nanotantennas towards metamaterials. In particular, studying the directionality of light in the infrared (IR) range could boost applications in heating control.

Metallic nanoparticles (NPs) can efficiently release heat under optical excitation. The heat generation process involves not only absorption of incident photons, but also heat transfer from the NP to the surrounding matrix. The mechanism of heat release is very simple - the laser electric field strongly drives mobile carriers inside the NPs, and the energy gained by carriers turns into heat. Then the heat diffuses away from the NP and leads to an elevated temperature of the surrounding medium. Heat generation becomes especially strong in the case of metal NPs in the regime of plasmon resonance. In the case of semiconductor NPs, the heat generation rate is much weaker since heat dissipation occurs through an interband absorption process with the creation of a single mobile electron and hole (exciton). I am currently involved in a project on the heating effects in plasmonic nanoparticles, where the electromagnetic losses from the electromagnetic waves in the NPs are assumed to be the only heat source. These results are being written in manuscript form to be sent for publication to a high impact journal.

Part III

APPENDIX

A

SYSTEMS OF UNITS

It is well-known that, in physics, there exist several systems of units with specific application fields. The different physical relations do not usually depend on the system of units, i.e. the expressions relating the physical magnitudes are the same regardless of the system of units used. This is not the case in electromagnetism.

The two systems of electromagnetic units in most common use today are the SI and the Gaussian system. Table A.1 displays the values of ε_0 and μ_0, the defining equations for **D** and **H**, the macroscopic forms of Maxwell's equations and the Lorentz force equation in the five common systems of units of electromagnetism. For each system of units the continuity equation for charge and current is given by:

$$\nabla \cdot \mathbf{J} + \frac{\partial \rho}{\partial t} = 0 \tag{A.1}$$

, which can be verified from the first pair of Maxwell's equations in the table in each case. Similarly, in all systems the statement of Ohm's law is $\mathbf{J} = \sigma \mathbf{E}$, where σ is the electric conductivity.

During the preparation of this dissertation, the candidate has faced the additional difficulty that the majority of references looked up (even the newest ones) use the Gaussian system of units. In Table A.2 the conversion for symbols and formulas is presented, which allows for the "translation" of expressions from the Gaussian system of units to the SI, the one used in this work. In particular, Table A.2 has been used to translate the expressions of the Lorentz local field (Equation (3.3)), the radiative field (Equation (3.9)) and the extinction (Equation (4.13)), absorption (Equation (4.14)) and scattering (Equation (4.15)) cross sections, these last taken from Chaumet and Rahmani [22].

SYSTEM	ε_0	μ_0	**D, H**	MACROSCOPIC MAXWELL'S EQUATIONS				LORENTZ FORCE PER UNIT CHARGE
Electrostatic (esu)	1	c^{-2} $(t^2 l^{-2})$	$\mathbf{D} = \mathbf{E} + 4\pi\mathbf{P}$ $\mathbf{H} = c^2\mathbf{B} - 4\pi\mathbf{M}$	$\nabla \cdot \mathbf{D} = 4\pi\rho$	$\nabla \times \mathbf{H} = 4\pi\mathbf{J} + \frac{\partial \mathbf{D}}{\partial t}$	$\nabla \times \mathbf{E} + \frac{\partial \mathbf{B}}{\partial t} = 0$	$\nabla \cdot \mathbf{B} = 0$	$\mathbf{E} + \mathbf{v} \times \mathbf{B}$
Electromagnetic emu	c^{-2} $(t^2 l^{-2})$	1	$\mathbf{D} = \frac{1}{c^2}\mathbf{E} + 4\pi\mathbf{P}$ $\mathbf{H} = \mathbf{B} - 4\pi\mathbf{M}$	$\nabla \cdot \mathbf{D} = 4\pi\rho$	$\nabla \times \mathbf{H} = 4\pi\mathbf{J} + \frac{\partial \mathbf{D}}{\partial t}$	$\nabla \times \mathbf{E} + \frac{\partial \mathbf{B}}{\partial t} = 0$	$\nabla \cdot \mathbf{B} = 0$	$\mathbf{E} + \mathbf{v} \times \mathbf{B}$
Gaussian	1	1	$\mathbf{D} = \mathbf{E} + 4\pi\mathbf{P}$ $\mathbf{H} = \mathbf{B} - 4\pi\mathbf{M}$	$\nabla \cdot \mathbf{D} = 4\pi\rho$	$\nabla \times \mathbf{H} = \frac{4\pi}{c}\mathbf{J} + \frac{1}{c}\frac{\partial \mathbf{D}}{\partial t}$	$\nabla \times \mathbf{E} + \frac{1}{c}\frac{\partial \mathbf{B}}{\partial t} = 0$	$\nabla \cdot \mathbf{B} = 0$	$\mathbf{E} + \frac{\mathbf{v}}{c} \times \mathbf{B}$
Heaviside- Lorentz	1	1	$\mathbf{D} = \mathbf{E} + \mathbf{P}$ $\mathbf{H} = \mathbf{B} - \mathbf{M}$	$\nabla \cdot \mathbf{D} = \rho$	$\nabla \times \mathbf{H} = \frac{1}{c}\left(\mathbf{J} + \frac{\partial \mathbf{D}}{\partial t}\right)$	$\nabla \times \mathbf{E} + \frac{1}{c}\frac{\partial \mathbf{B}}{\partial t} = 0$	$\nabla \cdot \mathbf{B} = 0$	$\mathbf{E} + \frac{\mathbf{v}}{c} \times \mathbf{B}$
SI	$\frac{10^7}{4\pi c^2}$ $(q^2 t^2 m^{-1} l^{-3})$	$4\pi \times 10^{-7}$ $(m l q^{-2})$	$\mathbf{D} = \varepsilon_0\mathbf{E} + \mathbf{P}$ $\mathbf{H} = \frac{1}{\mu_0}\mathbf{B} - \mathbf{M}$	$\nabla \cdot \mathbf{D} = \rho$	$\nabla \times \mathbf{H} = \mathbf{J} + \frac{\partial \mathbf{D}}{\partial t}$	$\nabla \times \mathbf{E} + \frac{\partial \mathbf{B}}{\partial t} = 0$	$\nabla \cdot \mathbf{B} = 0$	$\mathbf{E} + \mathbf{v} \times \mathbf{B}$

Table A.1: Definitions of ε_0, μ_0, **D**, **H**, macroscopic Maxwell's equations and Lorentz force equation in various systems of units. Where necessary the dimensions of quantities are given in parenthesis. The symbol c stands for the velocity of light in vacuum with dimensions (lt^{-1}). Taken from Jackson [16].

QUANTITY	GAUSSIAN	SI
Velocity of light	c	$(\mu_0\varepsilon_0)^{-1/2}$
Electric field (potential, voltage)	$\frac{\mathbf{E}(\Phi,V)}{\sqrt{4\pi\varepsilon_0}}$	$\mathbf{E}(\Phi, V)$
Displacement	$\sqrt{\frac{\varepsilon_0}{4\pi}}\mathbf{D}$	$\mathbf{D}$
Charge density (charge, current density, current, polarization)	$\sqrt{4\pi\varepsilon_0}\rho(q,\mathbf{J},I,\mathbf{P})$	$\rho(q,\mathbf{J},I,\mathbf{P})$
Magnetic induction	$\sqrt{\frac{\mu_0}{4\pi}}\mathbf{B}$	$\mathbf{B}$
Magnetic field	$\frac{\mathbf{H}}{\sqrt{4\pi\mu_0}}$	$\mathbf{H}$
Magnetization	$\sqrt{\frac{4\pi}{\mu_0}}\mathbf{M}$	$\mathbf{M}$
Conductivity	$4\pi\varepsilon_0\sigma$	σ
Dielectric constant	$\varepsilon_0\varepsilon$	ε
Magnetic permeability	$\mu_0\mu$	μ
Resistance (impedance)	$\frac{R(Z)}{4\pi\varepsilon_0}$	$R(Z)$
Inductance	$\frac{L}{4\pi\varepsilon_0}$	L
Capacitance	$4\pi\varepsilon_0 C$	C

$$c = 2.99792458 \times 10^8\ {}^{m}\!/_{s}$$
$$\varepsilon_0 = 8.854187817\cdots \times 10^{-12}\ {}^{F}\!/_{m}$$
$$\mu_0 = 1.2566370614\cdots \times 10^{-6}\ {}^{H}\!/_{m}$$
$$\sqrt{\frac{\mu_0}{\varepsilon_0}} = 376.7303\ldots\ \Omega$$

Table A.2: Conversion table for symbols and formulas. The symbols for mass, length, time, force, and other not specifically electromagnetic quantities are unchanged. To convert any equation in SI variables to the corresponding equation in Gaussian quantities, on both sides of the equation replace the relevant symbols listed below under "SI" by the corresponding "Gaussian" symbols listed on the left. The reverse transformation is also allowed. Taken from Jackson [16].

B

FIELDS OF ELECTRIC AND MAGNETIC DIPOLES

This section is partly based on Chapter 14 of Ref. [188]. We derive explicit expressions for the real-valued electric and magnetic fields of an oscillating z-directed electric dipole $\mathbf{p}(t) = p\hat{\mathbf{z}}\cos\omega t$. And also derive and plot the electric and magnetic field lines at several time instants. This problem has an important history, having been considered first by Hertz in 1889 in a paper reprinted in [189].

Restoring the $e^{-i\omega t}$ factor in Equations (2.13) and (2.14) and taking real parts, we obtain the fields:

$$\begin{aligned}\Re\{\mathbf{E}(\mathbf{r})\} = p\cos\omega t\left[k\sin(kr-\omega t) + \frac{\cos(kr-\omega t)}{r}\right]\frac{3\hat{\mathbf{r}}(\hat{\mathbf{r}}\cdot\hat{\mathbf{z}}-\hat{\mathbf{z}})}{4\pi\varepsilon_0 r^2} \\ + \frac{pk^2\hat{\mathbf{r}}\times(\hat{\mathbf{z}}\times\hat{\mathbf{r}})}{4\pi\varepsilon_0 r}\cos\omega t\cos(kr-\omega t)\end{aligned} \quad \text{(B.1)}$$

$$\Re\{\mathbf{H}(\mathbf{r})\} = p\omega\cos\omega t\left[k\cos(kr-\omega t) - \frac{\sin(kr-\omega t)}{r}\right]\left(\frac{\hat{\mathbf{z}}\times\hat{\mathbf{r}}}{4\pi r}\right) \quad \text{(B.2)}$$

In spherical coordinates, we have $\hat{\mathbf{z}} = \hat{\mathbf{r}}\cos\theta - \hat{\boldsymbol{\theta}}\sin\theta$. This gives $3\hat{\mathbf{r}}(\hat{\mathbf{r}}\cdot\hat{\mathbf{z}}) - \hat{\mathbf{z}} = 2\hat{\mathbf{r}}\cos\theta + \hat{\boldsymbol{\theta}}\sin\theta$, $\hat{\mathbf{r}}\times(\hat{\mathbf{z}}\times\hat{\mathbf{r}}) = -\hat{\boldsymbol{\theta}}\sin\theta$, and $\hat{\mathbf{z}}\times\hat{\mathbf{r}} = \hat{\boldsymbol{\phi}}\sin\theta$. Therefore, the non-zero components of $\mathbf{E}$ and $\mathbf{H}$ are E_r, E_θ and H_ϕ:

$$E_r(\mathbf{r}) = p\cos\omega t\left[k\sin(kr-\omega t) + \frac{\cos(kr-\omega t)}{r}\right]\left(\frac{2\cos\theta}{4\pi\varepsilon_0 r^2}\right) \quad \text{(B.3)}$$

$$\begin{aligned}E_\theta(\mathbf{r}) = p\cos\omega t\left[k\sin(kr-\omega t) + \frac{\cos(kr-\omega t)}{r}\right]\left(\frac{\sin\theta}{4\pi\varepsilon_0 r^2}\right) \\ - \frac{pk^2\sin\theta}{4\pi\varepsilon_0 r}\cos\omega t\cos(kr-\omega t)\end{aligned} \quad \text{(B.4)}$$

$$H_\phi(\mathbf{r}) = p\omega\cos\omega t\left[k\cos(kr-\omega t) - \frac{\sin(kr-\omega t)}{r}\right]\left(\frac{\sin\theta}{4\pi r}\right) \quad \text{(B.5)}$$

We rewrite Equations (B.3)-(B.5) in terms of the dimensionless variables $u = kr$ and $\delta = \omega t$, defining $E_0 = pk^3/(4\pi\varepsilon_0)$ and $H_0 = p\omega k^2/(4\pi)$:

$$E_r = E_0 \frac{2\cos\theta}{u^2} \cos\delta \left[\sin(u-\delta) + \frac{\cos(u-\delta)}{u} \right] \tag{B.6}$$

$$E_\theta = -E_0 \frac{\sin\theta}{u} \cos\delta \left[\cos(u-\delta) - \frac{\cos(u-\delta)}{u^2} - \frac{\sin(u-\delta)}{u} \right] \tag{B.7}$$

$$H_\phi = H_0 \frac{\sin\theta}{u} \cos\delta \left[\cos(u-\delta) - \frac{\sin(u-\delta)}{u} \right] \tag{B.8}$$

Please notice that H_0 is related to E_0 by:

$$H_0 = \frac{\omega\varepsilon_0}{k} E_0 = \sqrt{\frac{\varepsilon_0}{\mu_0}} E_0 \tag{B.9}$$

We now introduce the auxiliary functions:

$$Q(u) = \sin(u-\delta) + \frac{\cos(u-\delta)}{u} \tag{B.10}$$

$$R(u) = \cos(u-\delta) - \frac{\sin(u-\delta)}{u} \tag{B.11}$$

, noting that:

$$Q'(u) = \frac{dQ(u)}{du} = \cos(u-\delta) - \frac{\cos(u-\delta)}{u^2} - \frac{\sin(u-\delta)}{u} \tag{B.12}$$

Therefore, the fields are:

$$E_r = E_0 \frac{2\cos\theta}{u^2} \cos\delta Q(u), \quad E_\theta = -E_0 \frac{\sin\theta}{u} \cos\delta Q'(u) \tag{B.13}$$

$$H_\phi = H_0 \frac{\sin\theta}{u} \cos\delta R(u) \tag{B.14}$$

B.1 ELECTRIC AND MAGNETIC FIELDS LINES

B.1.1 *Electric field lines*

By definition, the electric field is tangential to its field lines. A small displacement $d\mathbf{r}$ along the tangent to a line will be parallel to $\mathbf{E}$ at that point. This implies that $d\mathbf{r} \times \mathbf{E} = 0$, which can be used to determine the lines. Because of the azimuthal symmetry in the ϕ variable, we may look at the field lines that lie on the xz-plane (that is, $\phi = 0$). Then, we have:

$$\begin{aligned} \mathbf{dr} \times \mathbf{E} = (\hat{\mathbf{r}}dr + \hat{\boldsymbol{\theta}}rd\theta) \times (\hat{\mathbf{r}}E_r + \hat{\boldsymbol{\theta}}E_\theta) = \hat{\boldsymbol{\phi}}(drE_\theta - rd\theta E_r) = 0 \\ \Rightarrow \frac{dr}{d\theta} = \frac{rE_r}{E_\theta} \end{aligned} \tag{B.15}$$

This determines r as a function of θ, giving the polar representation of the line curve. It follows that the equation for the lines in the variable u will be:

$$\begin{aligned} \frac{du}{d\theta} = \frac{uE_r}{E_\theta} = -2\cot\theta\left[\frac{Q(u)}{Q'(u)}\right] \\ \Rightarrow \frac{d}{d\theta}[\ln Q(u)] = -2\cot\theta = -\frac{d}{d\theta}\left(\ln\sin^2\theta\right) \end{aligned} \tag{B.16}$$

, which gives:

$$\frac{d}{d\theta}\ln\left[Q(u)\sin^2\theta\right] = 0 \Rightarrow Q(u)\sin^2\theta = C_E \tag{B.17}$$

, where C_E is a constant. Thus, the electric field lines are given implicitly by:

$$\begin{aligned} \left[\sin(u-\delta) + \frac{\cos(u-\delta)}{u}\right]\sin^2\theta \\ = \left[\sin(kr-\omega t) + \frac{\cos(kr-\omega t)}{kr}\right]\sin^2\theta = C_E \end{aligned} \tag{B.18}$$

Ideally, one should solve for r in terms of θ. Because this is not possible in closed form, we prefer to think of the lines as a contour plot at different values of the constant C. The resulting graphs are shown in Figure B.2. They were generated at the four time instants $t = 0$, $T/8$, $T/4$ and $3T/8$, where T is the period of oscillation, $T = 2\pi/\omega$. The x,z distances are in units of λ and extend to 1.5λ. We observe how the lines form closed loops originating at the dipole. The loops eventually escape the vicinity of the dipole and move outwards, pushing away the loops that are ahead of them. In this fashion, the field gets radiated away from its source.

B.1.2 *Magnetic field lines*

As we only have ϕ-component for the magnetic field, we may look at the field lines that lie on the xy-plane (that is, $\theta = \pi/2$). The magnetic field lines are given implicitly by:

$$\begin{aligned} H_\phi = H_0\frac{\cos\delta}{u}R(u) = C_H \\ = H_0\frac{\cos\omega t}{kr}\left[\cos(kr-\omega t) - \frac{\sin(kr-\omega t)}{kr}\right] = C_H \end{aligned} \tag{B.19}$$

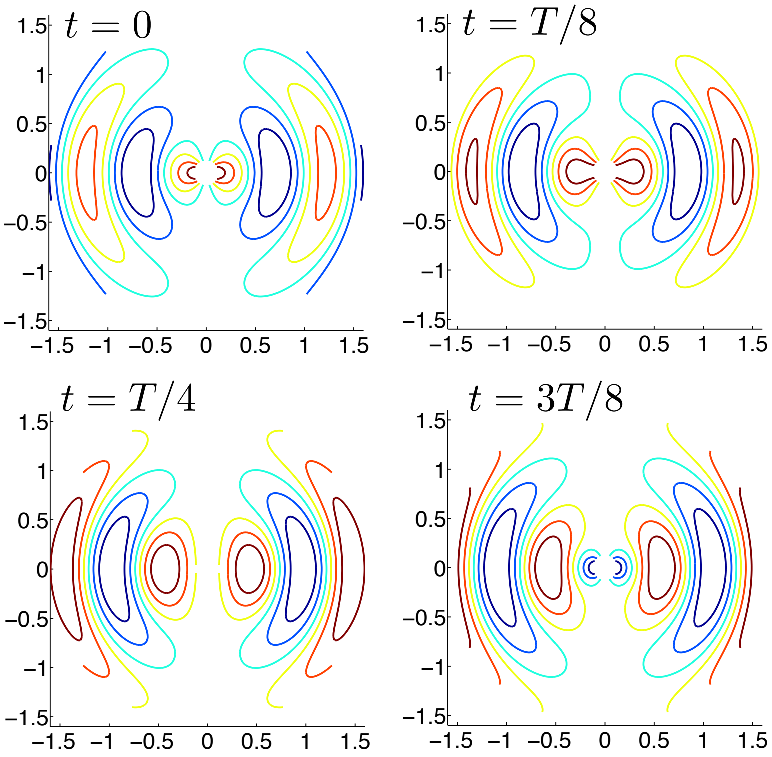

Figure B.1: Electric field lines of an oscillating electric dipole at successive time instants. The field lines lie on the xz-plane.

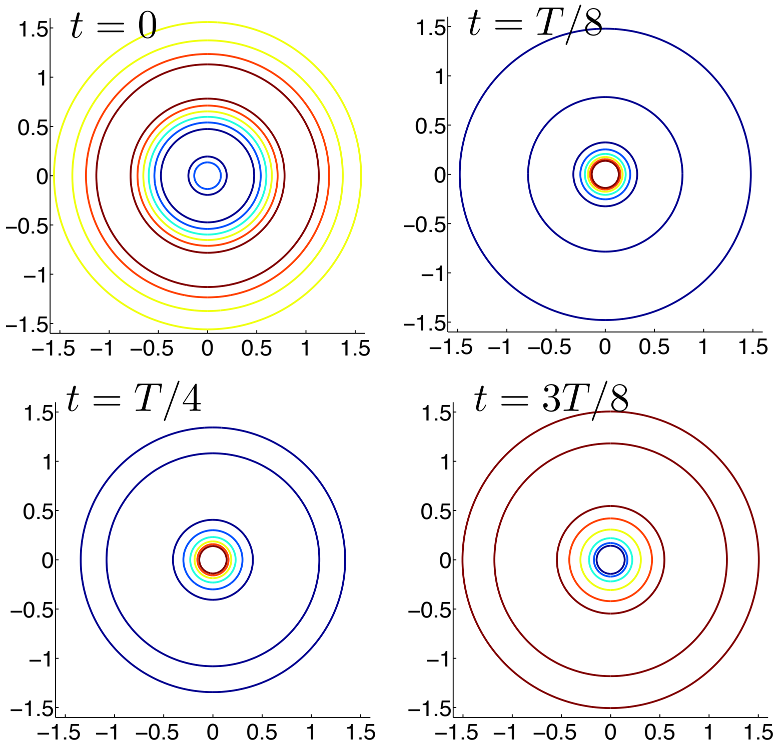

Figure B.2: Magnetic field lines of an oscillating electric dipole at successive time instants. The field lines lie on the xy-plane.

BIBLIOGRAPHY

[1] A. Einstein. Über einen die erzeugung und verwandlung des lichtes betreffenden heuristischen gesichtspunkt. *Annalen der Physik*, **322**(6):132–148, 1905.

[2] J. C. Maxwell. A dynamical theory of the electromagnetic field. *Philosophical Transactions of the Royal Society of London*, **155**:459–512, 1865.

[3] J. C. Maxwell. *A Treatise on Electricity and Magnetism*. Clarendon Press, Oxford, 1873.

[4] Lord Rayleigh. On the transmission of light through an atmosphere containing small particles in suspension, and on the origin of the blue of the sky. *Philosophical Magazine Series 5*, **47**(287): 375–384, 1899.

[5] R. P. Feynman. There's plenty of room at the bottom. *Engineering and Science*, **23**(5):22–36, 1960.

[6] A. M. Fennimore, T. D. Yuzvinsky, W.-Q. Han, M. S. Fuhrer, J. Cumings, and A. Zettl. Rotational actuators based on carbon nanotubes. *Nature*, **424**:408–410, 2003.

[7] U. Kreibig and M. Vollmer. *Optical Properties of Metal Clusters*. Springer-Verlag, Berlin, 1995.

[8] C. F. Bohren and D. R. Huffman. *Absorption and Scattering of Light by Small Particles*. Wiley, New York, 1983.

[9] M. Durach, A. Rusina, M. I. Stockman, and K. Nelson. Toward full spatiotemporal control on the nanoscale. *Nano letters*, **7**(10): 3145–3149, 2007.

[10] M. I. Stockman. Nanoplasmonics: The physics behind the applications. *Physics Today*, **64**(2):39–44, 2011.

[11] J. B. Jackson, S. L. Westcott, L. R. Hirsch, J. L. West, and N. J. Halas. Controlling the surface enhanced raman effect via the nanoshell geometry. *Applied Physics Letters*, **82**(2):257–259, 2003.

[12] H. Wang, D. W. Brandl, F. Le, P. Nordlander, and N. J. Halas. Nanorice: a hybrid plasmonic nanostructure. *Nano Letters*, **6**(4): 827–832, 2006.

[13] H. Liao, C. L Nehl, and J. H. Hafner. Biomedical applications of plasmon resonant metal nanoparticles. *Nanomedicine*, **1**(2): 201–208, 2006.

[14] E. S. Lander, L. M. Linton, B. Birren, C. Nusbaum, M. C. Zody, J. Baldwin, K. Devon, K. Dewar, M. Doyle, W. Fitzhugh, et al. Initial sequencing and analysis of the human genome. *Nature*, **409**(6822):860–921, 2001.

[15] G. W. Mulholland, C. F. Bohren, and K. A. Fuller. Light scattering by agglomerates: Coupled electric and magnetic dipole method. *Langmuir*, **10**(8):2533–2546, 1994.

[16] J. D. Jackson. *Classical Electrodynamics*. Wiley, New York, 2nd edition, 1975.

[17] Y. You, G. W. Kattawar, P.-W. Zhai, and P. Yang. Zero-backscatter cloak for aspherical particles using a generalized dda formalism. *Opt. Express*, **16**(3):2068–2079, 2008.

[18] E. M. Purcell. *Electricity and Magnetism, Berkeley Physics Course*, volume 1. McGraw-Hill, New York, 1st edition, 1965.

[19] C. Kittel. *Introduction to Solid State Physics*. Wiley, New York, 4th edition, 1986.

[20] B. T. Draine. The discrete-dipole approximation and its application to interstellar graphite grains. *Astrophys. J.*, **333**:848–872, 1988.

[21] S. Albaladejo, R. Gómez-Medina, L. S. Froufe-Pérez, H. Marinchio, R. Carminati, J. F. Torrado, G. Armelles, A. García-Martín, and J. J. Sáenz. Radiative corrections to the polarizability tensor of an electrically small anisotropic dielectric particle. *Optics Express*, **18**(4):3556–3567, 2010.

[22] Patrick C. Chaumet and Adel Rahmani. Coupled-dipole method for magnetic and negative-refraction materials. *Journal of Quantitative Spectroscopy and Radiative Transfer*, **110**(1–2): 22–29, 2009.

[23] B García-Cámara, F Moreno, F González, J M Saiz, and G Videen. Light scattering resonances in small particles with electric and magnetic properties. *Journal of the Optical Society of America A*, **25**(2):327–334, 2008.

[24] Q. Wu and W. Park. Negative index materials based on metal nanoclusters. *Applied Physics Letters*, **92**:153114, 2008.

[25] A. N. Grigorenko, A. K. Geim, H. F. Gleeson, Y. Zhang, A. A. Firsov, I. Y. Khrushchev, and J. Petrovic. Nanofabricated media with negative permeability at visible frequencies. *Nature*, **438** (7066):335–338, 2005.

[26] V. M. Shalaev. Optical negative-index metamaterials. *Nature Photonics*, **1**(1):41–48, 2007.

[27] H. Chen, C. T. Chan, and P. Sheng. Transformation optics and metamaterials. *Nature Materials*, **9**(5):387–396, 2010.

[28] Ortwin Hess. Optics: Farewell to Flatland. *Nature*, **455**(7211): 299–300, 2008.

[29] A. Alù and N. Engheta. Cloaking a Sensor. *Physical Review Letters*, **102**:233901, 2009.

[30] A. V. Kabashin, P. Evans, S. Pastkovsky, W. Hendren, G. A. Wurtz, R. Atkinson, R. Pollard, V. A. Podolskiy, and A. V. Zayats. Plasmonic nanorod metamaterials for biosensing. *Nature Materials*, **8**(11):867–871, 2009.

[31] M. Kerker, D.-S. Wang, and C. L. Giles. Electromagnetic scattering by magnetic spheres. *JOSA*, **73**(6):765–767, 1983.

[32] N. Engheta. Circuits with Light at Nanoscales: Optical Nanocircuits Inspired by Metamaterials. *Science*, **317**(5845):1698–1702, 2007.

[33] A. Alù and N. Engheta. How does zero forward-scattering in magnetodielectric nanoparticles comply with the optical theorem? *Journal of Nanophotonics*, **4**(1):041590, 2010.

[34] B. García-Cámara, F. González, F. Moreno, and J. M. Saiz. Exception for the zero-forward-scattering theory. *Journal of the Optical Society of America A*, **25**(11):2875–2878, 2008.

[35] H. C. van de Hulst. *Light scattering by small particles*. Dover Publications, 1957.

[36] N. G. Alexopoulos and N. K. Uzunoglu. Electromagnetic scattering from active objects: invisible scatterers. *Applied Optics*, **17**(2):235–239, 1978.

[37] M. Kerker. Resonances in electromagnetic scattering by objects with negative absorption. *Applied Optics*, **18**(8):1180–1189, 1979.

[38] S. A. Ramakrishna and O. J. Martin. Resolving the wave vector in negative refractive index media. *Optics Letters*, **30**(19):2626–2628, 2005.

[39] K. L. van der Molen, P. Zijlstra, A. Lagendijk, and A. P. Mosk. Laser threshold of Mie resonances. *Optics Letters*, **31**(10):1432–1434, 2006.

[40] B. García-Cámara, J. M. Saiz, F. González, and F. Moreno. Nanoparticles with unconventional scattering properties: Size effects. *Optics Communications*, **283**(3):490–496, 2010.

[41] V. M. Shalaev. *Nonlinear Optics of Random Media: Fractal Composites and Metal-Dielectric Films*, volume 158 of *Springer Tracts in Modern Physics*. Springer, Berlin, 2000.

[42] S. Bosch, J. Ferré-Borrull, N. Leinfellner, and A. Canillas. Effective dielectric function of mixtures of three or more materials: a numerical procedure for computations. *Surface Science*, **453** (1–3):9–17, 2000.

[43] M. W. Knight, Y. Wu, J. B. Lassiter, P. Nordlander, and N. J. Halas. Substrates matter: influence of an adjacent dielectric on an individual plasmonic nanoparticle. *Nano letters*, **9**(5):2188–2192, 2009.

[44] L. J. Sherry, S.-H. Chang, G. C. Schatz, R. P. Van Duyne, B. J. Wiley, and Y. Xia. Localized surface plasmon resonance spectroscopy of single silver nanocubes. *Nano letters*, **5**(10):2034–2038, 2005.

[45] A. J. Haes and R. P. Van Duyne. Nanoscale optical biosensors based on localized surface plasmon resonance spectroscopy. *Proc. SPIE*, **5221**(Plasmonics: Metallic Nanostructures and Their Optical Properties):47–58, 2003.

[46] D. A. Stuart, A. J. Haes, C. R. Yonzon, E. M. Hicks, and R. P. Van Duyne. Biological applications of localised surface plasmonic phenomenae. *IEE proceedings. Nanobiotechnology*, **152**(1): 13–32, 2005.

[47] K. Aslan, J. R. Lakowicz, and C. D. Geddes. Plasmon light scattering in biology and medicine: new sensing approaches, visions and perspectives. *Current Opinion in Chemical Biology*, **9** (5):538–544, 2005.

[48] X. Huang, P. K. Jain, I. H. El-Sayed, and M. A. El-Sayed. Plasmonic photothermal therapy (pptt) using gold nanoparticles. *Lasers in Medical Science*, **23**(3):217–228, 2008.

[49] M. D. Malinsky, K. L. Kelly, G. C. Schatz, and R. P. Van Duyne. Nanosphere lithography: Effect of substrate on the localized surface plasmon resonance spectrum of silver nanoparticles. *The Journal of Physical Chemistry B*, **105**(12):2343–2350, 2001.

[50] T. A. Germer. Light scattering by slightly nonspherical particles on surfaces. *Opt. Lett.*, **27**(13):1159–1161, 2002.

[51] S. Nie and S. R. Emory. Probing single molecules and single nanoparticles by surface-enhanced raman scattering. *Science*, **275**(5303):1102–1106, 1997.

[52] H. Xu, J. Aizpurúa, M. Kall, and P. Apell. Electromagnetic contributions to single-molecule sensitivity in surface-enhanced raman scattering. *Physical Review E*, **62**(3):4318–4324, 2000.

[53] T. A. Germer and G. W. Mulholland. Particle Size Metrology: Comparison Between Aerosol Electrical Mobility and Laser Surface Light Scattering Techniques. In *Characterization and Metrology for ULSI Technology 2005.*, volume 788 of *American Institute of Physics Conference Series*, pages 579–583, 2005.

[54] G. Mie. Beiträge zur optik trüber medien, speziell kolloidaler metallösungen. *Annalen der Physik*, **330**(3):377–445, 1908.

[55] M. I. Mishchenko and D. W. Mackowski. Electromagnetic scattering by randomly oriented bispheres: Comparison of theory and experiment and benchmark calculations. *Journal of Quantitative Spectroscopy and Radiative Transfer*, **55**(5):683–694, 1996.

[56] M. A. Yurkin, V. P. Maltsev, and A. G. Hoekstra. The discrete dipole approximation for simulation of light scattering by particles much larger than the wavelength. *Journal of Quantitative Spectroscopy and Radiative Transfer*, **106**(1–3):546–557, 2007.

[57] T. Wriedt. A review of elastic light scattering theories. *Particle & Particle Systems Characterization*, **15**(2):67–74, 1998.

[58] P. C. Waterman. Matrix formulation of electromagnetic scattering. *Proceedings of the IEEE*, **53**(8):805–812, 1965.

[59] P. Waterman. Symmetry, unitarity, and geometry in electromagnetic scattering. *Physical Review D*, **3**(4):825–839, 1971.

[60] M. I. Mishchenko, G. Videen, V. A. Babenko, N. G. Khlebtsov, and T. Wriedt. T-matrix theory of electromagnetic scattering by partciles and its applications: a comprehensive reference database. *Journal of Quantitative Spectroscopy and Radiative Transfer*, **88**(1–3):357–406, 2004.

[61] R.-J. Zhu, J. Wang, and G.-F. Jin. Mie scattering calculation by fdtd employing a modified debye model for gold material. *Optik - International Journal for Light and Electron Optics*, **116**(9): 419–422, 2005.

[62] Z. Chen, X. Li, A. Taflove, and V. Backman. Backscattering enhancement of light by nanoparticles positioned in localized optical intensity peaks. *Appl. Opt.*, **45**(4):633–638, 2006.

[63] V. E. Ferry, L. A. Sweatlock, D. Pacifici, and H. A. Atwater. Plasmonic nanostructure design for efficient light coupling into solar cells. *Nano Letters*, **8**(12):4391–4397, 2008.

[64] A. Dhawan, S. J. Norton, M. D. Gerhold, and T. Vo-Dinh. Comparison of fdtd numerical computationsand analytical multipole expansion method for plasmonics-active nanosphere dimers. *Opt. Express*, **17**(12):9688–9703, 2009.

[65] K. Yee. Numerical solution of initial boundary value problems involving maxwell's equations in isotropic media. *IEEE Transactions on Antennas and Propagation*, **14**(3):302–307, 1966.

[66] A. Taflove. Review of the formulation and applications of the finite-difference time-domain method for numerical modeling of electromagnetic wave interactions with arbitrary structures. *Wave Motion*, **10**(6):547–582, 1988.

[67] A. Sommerfeld. Über die ausbreitung der wellen in der drahtlosen telegraphie. *Annalen der Physik*, **333**(4):665–736, 1909.

[68] F. González, G. Videen, P. J. Valle, J. M. Saiz, J. L. de la Pena, and F. Moreno. Light scattering computational methods for particles on substrates. *Journal of Quantitative Spectroscopy and Radiative Transfer*, **70**(4–6):383–393, 2001.

[69] D. N. Pattanayak and E. Wolf. General form and a new interpretation of the ewald-oseen extinction theorem. *Optics Communications*, **6**(3):217–220, 1972.

[70] M. Nieto-Vesperinas. *Scattering and Diffraction in Physical Optics*. World Scientific Publishing Co, 2006.

[71] B. R. Johnson. Calculation of light scattering from a spherical particle on a surface by the multipole expansion method. *J. Opt. Soc. Am. A*, **13**(2):326–337, 1996.

[72] G. Videen. Light scattering from a sphere on or near a surface. *J. Opt. Soc. Am. A*, **8**(3):483–489, 1991.

[73] G. Videen. Light scattering from a particle on or near a perfectly conducting surface. *Optics Communications*, **115**(1–2):1–7, 1995.

[74] G. Videen. Polarized light scattering from surface contaminants. *Optics Communications*, **143**(4–6):173–178, 1997.

[75] D. Ngo and G. Videen. Light scattering from spheres. *Optical Engineering*, **36**(1):150–156, 1997.

[76] G. Videen and D. Ngo. Light scattering from a cylinder near a plane interface: theory and comparison with experimental data. *J. Opt. Soc. Am. A*, **14**(1):70–78, 1997.

[77] K. B. Nahm and W. L. Wolfe. Light-scattering models for spheres on a conducting plane: comparison with experiment. *Appl. Opt.*, **26**(15):2995–2999, 1987.

[78] P. W. Barber and S. C. Hill. *Light scattering by particles: computational methods*. World Scientific Publishing Co, 1990.

[79] J. L. de la Peña, F. González, J. M. Saiz, F. Moreno, and P. J. Valle. Sizing particles on substrates. a general method for oblique incidence. *Journal of Applied Physics*, **85**(1):432–438, 1999.

[80] B. R. Johnson. Light scattering from a spherical particle on a conducting plane: I. normal incidence. *J. Opt. Soc. Am. A*, **9**(8): 1341–1351, 1992.

[81] R. Schmehl, B. M. Nebeker, and E. D. Hirleman. Discrete-dipole approximation for scattering by features on surfaces by means of a two-dimensional fast fourier transform technique. *J. Opt. Soc. Am. A*, **14**(11):3026–3036, 1997.

[82] B. T. Draine and P. J. Flatau. Discrete-dipole approximation for scattering calculations. *J. Opt. Soc. Am. A*, **11**(4):1491–1499, 1994.

[83] R. Alcaraz de la Osa, P. Albella, J. M. Saiz, F. González, and F. Moreno. Extended discrete dipole approximation and its application to bianisotropic media. *Opt. Express*, **18**(23):23865–23871, 2010.

[84] E. M. Purcell and C. R. Pennypacker. Scattering and Absorption of Light by Nonspherical Dielectric Grains. *Astrophys. J.*, **186**: 705–714, 1973.

[85] B. T. Draine and P. J. Flatau. User guide for the discrete dipole approximation code ddscat 7.1. arXiv:1002.1505v1, 2010.

[86] M. Botchev. `http://www.math.uu.nl/people/vorst/zbcg2.f90`, 2001.

[87] P. B. Johnson and R. W. Christy. Optical constants of the noble metals. *Phys. Rev. B*, **6**:4370–4379, 1972.

[88] L. Novotny and N. van Hulst. Antennas for light. *Nature Photonics*, **5**:83–90, 2011.

[89] V. Giannini, A. I. Fernández-Domínguez, S. C. Heck, and S. A. Maier. Plasmonic nanoantennas: Fundamentals and their use in controlling the radiative properties of nanoemitters. *Chemical Reviews*, **111**(6):3888–3912, 2011.

[90] J. N. Anker, W. P. Hall, O. Lyandres, N. C. Shah, J. Zhao, and R. P. Van Duyne. Biosensing with plasmonic nanosensors. *Nature materials*, **7**(6):442–453, 2008.

[91] K. C. Weng, C. O. Noble, B. Papahadjopoulos-Sternberg, F. F. Chen, D. C. Drummond, D. B. Kirpotin, D. Wang, Y. K. Hom, B. Hann, and J. W. Park. Targeted tumor cell internalization and

imaging of multifunctional quantum dot-conjugated immunoliposomes in vitro and in vivo. *Nano Letters*, **8**(9):2851–2857, 2008.

[92] R. Quidant and M. Kreuzer. Biosensing: Plasmons offer a helping hand. *Nature Nanotechnology*, **5**:762–763, 2010.

[93] M. Sandtke and L. Kuipers. Slow guided surface plasmons at telecom frequencies. *Nature Photonics*, **1**:573–576, 2007.

[94] B. C. Stipe, T. C. Strand, C. C. Poon, H. Balamane, T. D. Boone, J. A. Katine, J.-L. Li, V. Rawat, H. Nemoto, A. Hirotsune, O. Hellwig, R. Ruiz, E. Dobisz, D. S. Kercher, N. Robertson, T. R. Albrecht, and B. D. Terris. Magnetic recording at 1.5 Pb m^{-2} using an integrated plasmonic antenna. *Nature Photonics*, **4**:484–488, 2010.

[95] P. N. Prasad. *Nanophotonics*. John Wiley & Sons, Inc., 2004.

[96] J. M. Steele, N. K. Grady, P. Nordlander, and N. J. Halas. Plasmon hybridization in complex nanostructures. In Mark Brongersma and Pieter Kik, editors, *Surface Plasmon Nanophotonics*, volume 131 of *Springer Series in Optical Sciences*, pages 183–196. Springer Berlin / Heidelberg, 2007.

[97] M. Pelton, J. Aizpurúa, and G. Bryant. Metal-nanoparticle plasmonics. *Laser and Photonics Reviews*, **2**(3):136–159, 2008.

[98] N. Insin, J. B. Tracy, H. Lee, J. P. Zimmer, R. M. Westervelt, and M. G. Bawendi. Incorporation of iron oxide nanoparticles and quantum dots into silica microspheres. *ACS Nano*, **2**(2):197–202, 2008.

[99] M. Schnell, A. Garcia-Etxarri, A. J. Huber, K. B. Crozier, A. Borisov, J. Aizpurúa, and R. Hillenbrand. Amplitude- and phase-resolved near-field mapping of infrared antenna modes by transmission-mode scattering-type near-field microscopy. *The Journal of Physical Chemistry C*, **114**(16):7341–7345, 2010.

[100] V. Myroshnychenko, J. Rodríguez-Fernández, I. Pastoriza-Santos, A. M. Funston, C. Novo, P. Mulvaney, L. M. Liz-Marzán, and F. J. García de Abajo. Modelling the optical response of gold nanoparticles. *Chem. Soc. Rev.*, **37**:1792–1805, 2008.

[101] R. T. Hill, J. J. Mock, Y. Urzhumov, D. S. Sebba, S. J. Oldenburg, S.-Y. Chen, A. A. Lazarides, A. Chilkoti, and D. R. Smith. Leveraging nanoscale plasmonic modes to achieve reproducible enhancement of light. *Nano Letters*, **10**(10):4150–4154, 2010.

[102] P. Albella, B. García-Cueto, F. González, F. Moreno, P. C. Wu, T.-H. Kim, A. Brown, Y. Yang, H. O. Everitt, and G. Videen.

Shape matters: Plasmonic nanoparticle shape enhances interaction with dielectric substrate. *Nano Letters*, **11**(9):3531–3537, 2011.

[103] M. Grimsditch and P. Vavassori. The diffracted magneto-optic kerr effect: what does it tell you? *J. Phys.: Condens. Matter*, **16**: R275–R294, 2004.

[104] J. B. González-Díaz, A. García-Martín, J. M. García-Martín, A. Cebollada, G. Armelles, B. Sepúlveda, Y. Alaverdyan, and M. Käll. Plasmonic au/co/au nanosandwiches with enhanced magneto-optical activity. *Small*, **4**(2):202–205, 2008.

[105] P. K. Jain, Y. Xiao, R. Walsworth, and A. E. Cohen. Surface plasmon resonance enhanced magneto-optics (supremo): Faraday rotation enhancement in gold-coated iron oxide nanocrystals. *Nano Letters*, **9**(4):1644–1650, 2009.

[106] J. B. González-Díaz, J. M. García-Martín, A. García-Martín, D. Navas, A. Asenjo, M. Vázquez, M. Hernández-Vélez, and G. Armelles. Plasmon-enhanced magneto-optical activity in ferromagnetic membranes. *Applied Physics Letters*, **94**:263101, 2009.

[107] V. V. Temnov, G. Armelles, U. Woggon, D. Guzatov, A. Cebollada, A. Garcia-Martin, J.-M. Garcia-Martin, T. Thomay, A. Leitenstorfer, and R. Bratschitsch. Active magneto-plasmonics in hybrid metal-ferromagnet structures. *Nature Photonics*, **4**:107–111, 2010.

[108] V. I. Belotelov, I. A. Akimov, M. Pohl, V. A. Kotov, S. Kasture, A. S. Vengurlekar, A. V. Gopal, D. R. Yakovlev, A. K. Zvezdin, and M. Bayer. Enhanced magneto-optical effects in magnetoplasmonic crystals. *Nature Nanotechnology*, **6**:370–376, 2011.

[109] V. Bonanni, S. Bonetti, T. Pakizeh, Z. Pirzadeh, J. Chen, J. Nogués, P. Vavassori, R. Hillenbrand, J. Åkerman, and A. Dmitriev. Designer magnetoplasmonics with nickel nanoferromagnets. *Nano Letters*, **11**(12):5333–5338, 2011.

[110] J. B. González-Díaz, A. García-Martín, G. Armelles, D. Navas, M. Vázquez, K. Nielsch, R. B. Wehrspohn, and U. Gösele. Enhanced magneto-optics and size effects in ferromagnetic nanowire arrays. *Advanced Materials*, **19**(18):2643–2647, 2007.

[111] J. B. González-Díaz, B. Sepúlveda, A. García-Martín, and G. Armelles. Cobalt dependence of the magneto-optical response in magnetoplasmonic nanodisks. *Applied Physics Letters*, **97**(4):043114, 2010.

[112] G. X. Du, T. Mori, S. Saito, and M. Takahashi. Shape-enhanced magneto-optical activity: Degree of freedom for active plasmonics. *Phys. Rev. B*, **82**:161403(R), 2010.

[113] L. Wang, C. Clavero, Z. Huba, K. J. Carroll, E. E. Carpenter, D. Gu, and R. A. Lukaszew. Plasmonics and enhanced magneto-optics in core-shell co-ag nanoparticles. *Nano Letters*, **11**(3):1237–1240, 2011.

[114] J. Chen, P. Albella, Z. Pirzadeh, P. Alonso-González, F. Huth, S. Bonetti, V. Bonanni, J. Åkerman, J. Nogués, P. Vavassori, A. Dmitriev, J. Aizpurúa, , and R. Hillenbrand. Plasmonic nickel nanoantennas. *Small*, **7**(16):2341–2347, 2011.

[115] D. A. Smith and K. L. Stokes. Discrete dipole approximation for magneto-optical scattering calculations. *Optics Express*, **14**: 5746–5754, 2006.

[116] G. Ctistis, E. Papaioannou, P. Patoka, J. Gutek, P. Fumagalli, and M. Giersig. Optical and magnetic properties of hexagonal arrays of subwavelength holes in optically thin cobalt films. *Nano Letters*, **9**(1):1–6, 2009.

[117] M. Freiser. A survey of magnetooptic effects. *IEEE Transactions on Magnetics*, **4**(2):152–161, 1968.

[118] A. Berger and M. R. Pufall. Quantitative vector magnetometry using generalized magneto-optical ellipsometry. *Journal of Applied Physics*, **85**:4583–4585, 1999.

[119] D. Meneses-Rodríguez, E. Ferreiro-Vila, P. Prieto, J. Anguita, M. U. González, J. M. García-Martín, A. Cebollada, A. García-Martín, and G. Armelles. Probing the electromagnetic field distribution within a metallic nanodisk. *Small*, **7**(23):3317–3323, 2011.

[120] W. Cai and V. M. Shalaev. *Optical Metamaterials: Fundamentals and Applications*. Springer, New York, 2010.

[121] S. P. Burgos, R. de Waele, A. Polman, and H. A. Atwater. A single-layer wide-angle negative-index metamaterial at visible frequencies. *Nat Mater*, **9**(5):407–412, 2010.

[122] A. Boltasseva and V. M. Shalaev. Fabrication of optical negative-index metamaterials: Recent advances and outlook. *Metamaterials*, **2**(1):1–17, 2008.

[123] J. C. Maxwell Garnett. Colours in metal glasses and in metallic films. *Philosophical Transactions of the Royal Society of London. Series A, Containing Papers of a Mathematical or Physical Character*, **203**(359–371):385–420, 1904.

[124] S. Link, Z. L. Wang, and M. A. El-Sayed. Alloy formation of gold-silver nanoparticles and the dependence of the plasmon absorption on their composition. *The Journal of Physical Chemistry B*, **103**(18):3529–3533, 1999.

[125] A. Syed. Permalloy Magnetic Domain Control For Radio Frequency Applications. In A. Ghoshray, B. Bandyopadhyay, and C. Mazumdar, editors, *American Institute of Physics Conference Series*, volume 1347, pages 79–82, 2011.

[126] G. S. Krinchik and V. A. Artem'ev. Magneto-optical Properties of Ni, Co, and Fe in the Ultraviolet Visible and Infrared Parts of the Spectrum. *Soviet Journal of Experimental and Theoretical Physics*, **26**:1080, 1968.

[127] R. Liu, A. Degiron, J. J. Mock, and D. R. Smith. Negative index material composed of electric and magnetic resonators. *Applied Physics Letters*, **90**:263504, 2007.

[128] R. Ferrando, J. Jellinek, and R. L. Johnston. Nanoalloys: From theory to applications of alloy clusters and nanoparticles. *Chemical Reviews*, **108**(3):845–910, 2008.

[129] L. M. Liz-Marzán. Tailoring surface plasmons through the morphology and assembly of metal nanoparticles. *Langmuir*, **22**(1): 32–41, 2006.

[130] G. H. Goedecke and S. G. O'Brien. Scattering by irregular inhomogeneous particles via the digitized green's function algorithm. *Appl. Opt.*, **27**(12):2431–2438, 1988.

[131] M. F. Iskander, H. Y. Chen, and J. E. Penner. Optical scattering and absorption by branched chains of aerosols. *Appl. Opt.*, **28** (15):3083–3091, 1989.

[132] J. I. Hage and J. M. Greenberg. A model for the optical properties of porous grains. *Astrophys. J.*, **361**:251–259, 1990.

[133] B. T. Draine and J. Goodman. Beyond Clausius-Mossotti - Wave propagation on a polarizable point lattice and the discrete dipole approximation. *Astrophys. J.*, **405**:685–697, 1993.

[134] D. Gutkowicz-Krusin and B. T. Draine. Propagation of Electromagnetic Waves on a Rectangular Lattice of Polarizable Points. *ArXiv Astrophysics e-prints*, 2004.

[135] C. E. Dungey and C. F. Bohren. Light scattering by nonspherical particles: a refinement to the coupled-dipole method. *J. Opt. Soc. Am. A*, **8**(1):81–87, 1991.

[136] W. T. Doyle. Optical properties of a suspension of metal spheres. *Phys. Rev. B*, **39**:9852–9858, 1989.

[137] H. Okamoto. Light scattering by clusters: the al-term method. *Optical Review*, **2**:407–412, 1995.

[138] A. Rahmani, P. C. Chaumet, and G. W. Bryant. Coupled dipole method with an exact long-wavelength limit and improved accuracy at finite frequencies. *Opt. Lett.*, **27**(23):2118–2120, 2002.

[139] A. Rahmani, P. C. Chaumet, and G. W. Bryant. On the importance of local-field corrections for polarizable particles on a finite lattice: Application to the discrete dipole approximation. *The Astrophysical Journal*, **607**(2):873, 2004.

[140] M. J. Collinge and B. T. Draine. Discrete-dipole approximation with polarizabilities that account for both finite wavelength and target geometry. *J. Opt. Soc. Am. A*, **21**(10):2023–2028, 2004.

[141] P. C. Chaumet, A. Sentenac, and A. Rahmani. Coupled dipole method for scatterers with large permittivity. *Phys. Rev. E*, **70**: 036606, 2004.

[142] N. B. Piller. Influence of the edge meshes on the accuracy of the coupled-dipole approximation. *Opt. Lett.*, **22**(22):1674–1676, 1997.

[143] M. A. Yurkin, V. P. Maltsev, and A. G. Hoekstra. Convergence of the discrete dipole approximation. i. theoretical analysis. *J. Opt. Soc. Am. A*, **23**(10):2578–2591, 2006.

[144] D. R. Smith. Analytic expressions for the constitutive parameters of magnetoelectric metamaterials. *Phys. Rev. E*, **81**:036605, 2010.

[145] P. A. Belov and C. R. Simovski. Homogenization of electromagnetic crystals formed by uniaxial resonant scatterers. *Phys. Rev. E*, **72**:026615, 2005.

[146] S. Tretyakov. *Analytical Modeling in Applied Electromagnetics*. Artech House Electromagnetic Analysis Series. Artech House, 2003.

[147] J. E. Sipe. New green-function formalism for surface optics. *J. Opt. Soc. Am. B*, **4**(4):481–489, 1987.

[148] J. Zenneck. Über die Fortpflanzung ebener elektromagnetischer Wellen längs einer ebenen Leiterfläche und ihre Beziehung zur drahtlosen Telegraphie. *Annalen der Physik*, **328**:846–866, 1907.

[149] J. A. Scholl, A. L. Koh, and J. A. Dionne. Quantum plasmon resonances of individual metallic nanoparticles. *Nature*, **483**(7390): 421–427, 2012.

[150] C. J. Cheng and W. M. Saltzman. Nanomedicine: Downsizing tumour therapeutics. *Nat Nano*, **7**(6):346–347, 2012.

[151] K. Kneipp, Y. Wang, H. Kneipp, L. T. Perelman, I. Itzkan, R. R. Dasari, and M. S. Feld. Single molecule detection using surface-enhanced raman scattering (sers). *Phys. Rev. Lett.*, **78**:1667–1670, 1997.

[152] H. A. Atwater and A. Polman. Plasmonics for improved photovoltaic devices. *Nat Mater*, **9**(3):205–213, 2010.

[153] S. Kim, J. Jin, Y.-J. Kim, I.-Y. Park, Y. Kim, and S.-W. Kim. High-harmonic generation by resonant plasmon field enhancement. *Nature*, **453**(7196):757–760, 2008.

[154] P. Nordlander, C. Oubre, E. Prodan, K. Li, and M. I. Stockman. Plasmon hybridization in nanoparticle dimers. *Nano Letters*, **4** (5):899–903, 2004.

[155] R. Esteban, A. G. Borisov, P. Nordlander, and J. Aizpurúa. Bridging quantum and classical plasmonics with a quantum-corrected model. *Nat Commun*, **3**:825, 2012.

[156] K. J. Savage, M. M. Hawkeye, R. Esteban, A. G. Borisov, J. Aizpurúa, and J. J. Baumberg. Revealing the quantum regime in tunnelling plasmonics. *Nature*, **491**(7425):574–577, 2012.

[157] D. Mackowski. Scsmfo.for: Calculation of the scattering properties for a cluster of spheres. *User guide accompanying the SCSMFO.FOR code*, 1999.

[158] D. W. Mackowski and M. I. Mishchenko. Calculation of the t matrix and the scattering matrix for ensembles of spheres. *J. Opt. Soc. Am. A*, **13**(11):2266–2278, 1996.

[159] A. D. Rakic, A. B. Djurišic, J. M. Elazar, and M. L. Majewski. Optical properties of metallic films for vertical-cavity optoelectronic devices. *Appl. Opt.*, **37**(22):5271–5283, 1998.

[160] F. Hao and P. Nordlander. Efficient dielectric function for fdtd simulation of the optical properties of silver and gold nanoparticles. *Chemical Physics Letters*, **446**(1–3):115–118, 2007.

[161] A. Vial, T. Laroche, M. Dridi, and L. Le Cunff. A new model of dispersion for metals leading to a more accurate modeling of plasmonic structures using the fdtd method. *Applied Physics A*, **103**:849–853, 2011.

[162] L. Genzel, T. P. Martin, and U. Kreibig. Dielectric function and plasma resonances of small metal particles. *Zeitschrift für Physik B Condensed Matter*, **21**:339–346, 1975.

[163] W. A. Kraus and G. C. Schatz. Plasmon resonance broadening in small metal particles. *J. Chem. Phys.*, **79**:6130–6139, 1983.

[164] Y. He and T. Zeng. First-principles study and model of dielectric functions of silver nanoparticles. *The Journal of Physical Chemistry C*, **114**(42):18023–18030, 2010.

[165] S. Berciaud, L. Cognet, P. Tamarat, and B. Lounis. Observation of intrinsic size effects in the optical response of individual gold nanoparticles. *Nano Letters*, **5**(3):515–518, 2005.

[166] U. Kreibig and C. V. Fragstein. The limitation of electron mean free path in small silver particles. *Zeitschrift für Physik*, **224**:307–323, 1969.

[167] U. Kreibig and L. Genzel. Optical absorption of small metallic particles. *Surface Science*, **156, Part 2**:678–700, 1985.

[168] V. Amendola and M. Meneghetti. Size evaluation of gold nanoparticles by uv-vis spectroscopy. *The Journal of Physical Chemistry C*, **113**(11):4277–4285, 2009.

[169] M. M. Alvarez, J. T. Khoury, T. G. Schaaff, M. N. Shafigullin, I. Vezmar, and R. L. Whetten. Optical absorption spectra of nanocrystal gold molecules. *The Journal of Physical Chemistry B*, **101**(19):3706–3712, 1997.

[170] H. Hövel, S. Fritz, A. Hilger, U. Kreibig, and M. Vollmer. Width of cluster plasmon resonances: Bulk dielectric functions and chemical interface damping. *Phys. Rev. B*, **48**:18178–18188, 1993.

[171] E. D. Palik. *Handbook of Optical Constants of Solids*. Handbook of Optical Constants of Solids Series. Acad. Press, 1991.

[172] M. I. Tribelsky. Anomalous light absorption by small particles. *EPL (Europhysics Letters)*, **94**(1):14004, 2011.

[173] P. K. Jain, X. Huang, I. H. El-Sayed, and M. A. El-Sayed. Noble metals on the nanoscale: Optical and photothermal properties and some applications in imaging, sensing, biology, and medicine. *Accounts of Chemical Research*, **41**(12):1578–1586, 2008.

[174] J. B. Lassiter, M. W. Knight, N. A. Mirin, and N. J. Halas. Reshaping the plasmonic properties of an individual nanoparticle. *Nano Letters*, **9**(12):4326–4332, 2009.

[175] C. Loo, L. Hirsch, M.-H. Lee, E. Chang, J. West, N. Halas, and R. Drezek. Gold nanoshell bioconjugates for molecular imaging in living cells. *Opt. Lett.*, **30**(9):1012–1014, 2005.

[176] B. Setién, P. Albella, J. M. Saiz, F. González, and F. Moreno. Spectral behavior of the linear polarization degree at right-angle scattering configuration for nanoparticle systems. *New Journal of Physics*, **12**(10):103031, 2010.

[177] I. Lieberman, G. Shemer, T. Fried, E. M. Kosower, and G. Markovich. Plasmon-resonance-enhanced absorption and circular dichroism. *Angewandte Chemie International Edition*, **47** (26):4855–4857, 2008.

[178] Krishanu Ray, Mustafa H Chowdhury, and Joseph R Lakowicz. Aluminum nanostructured films as substrates for enhanced fluorescence in the ultraviolet-blue spectral region. *Analytical chemistry*, **79**(17):6480–6487, 2007.

[179] M. H. Chowdhury, K. Ray, S. K. Gray, J. Pond, and J. R. Lakowicz. Aluminum nanoparticles as substrates for metal-enhanced fluorescence in the ultraviolet for the label-free detection of biomolecules. *Analytical chemistry*, **81**(4):1397, 2009.

[180] A. Taguchi, N. Hayazawa, K. Furusawa, H. Ishitobi, and S. Kawata. Deep-uv tip-enhanced raman scattering. *Journal of Raman Spectroscopy*, **40**(9):1324–1330, 2009.

[181] K. A. Willets and R. P. Van Duyne. Localized surface plasmon resonance spectroscopy and sensing. *Annu. Rev. Phys. Chem.*, **58**: 267–297, 2007.

[182] G. H. Chan, J. Zhao, G. C. Schatz, and R. P. Van Duyne. Localized surface plasmon resonance spectroscopy of triangular aluminum nanoparticles. *The Journal of Physical Chemistry C*, **112**(36):13958–13963, 2008.

[183] M. W. Knight, L. Liu, Y. Wang, L. Brown, S. Mukherjee, N. S. King, H. O. Everitt, P. Nordlander, and N. J. Halas. Aluminum plasmonic nanoantennas. *Nano letters*, **12**(11):6000–6004, 2012.

[184] X. Jiao, S. Blair, L. Shi, L. Tian, X. Chen, H.-R. Kim, E. Jang, J. Kim, K.-I. Joo, S.-D. Lee, et al. Optical antenna design for fluorescence enhancement in the ultraviolet. *Optics express*, **20** (28):29909–29922, 2012.

[185] R. Paniagua-Domínguez, F. López-Tejeira, R. Marqués, and J. A. Sánchez-Gil. Metallo-dielectric core–shell nanospheres as building blocks for optical three-dimensional isotropic negative-index metamaterials. *New Journal of Physics*, **13**(12):123017, 2011.

[186] J. M. Geffrin, B. García-Cámara, R. Gómez-Medina, P. Albella, L. S. Froufe-Pérez, C. Eyraud, A. Litman, R. Vaillon, F. González, M. Nieto-Vesperinas, et al. Magnetic and electric coherence in forward-and back-scattered electromagnetic

waves by a single dielectric subwavelength sphere. *Nature communications*, **3**:1171, 2012.

[187] Y. H. Fu, A. I. Kuznetsov, A. E. Miroshnichenko, Y. F. Yu, and B. Lukyanchuk. Directional visible light scattering by silicon nanoparticles. *Nature Communications*, **4**:1527, 2013.

[188] S. J. Orfanidis. *Electromagnetic Waves and Antennas*. Rutgers University, 2010. URL `http://www.ece.rutgers.edu/~orfanidi/ewa/`.

[189] H. Hertz. *Electric waves: being researches on the propagation of electric action with finite velocity through space*. Dover books on History of Science and Classics of Science. Dover Publications, 1962.

COLOPHON

This document was typeset using the typographical look-and-feel `classicthesis` developed by André Miede. The style was inspired by Robert Bringhurst's seminal book on typography "*The Elements of Typographic Style*". `classicthesis` is available for both LaTeX and LyX:

`http://code.google.com/p/classicthesis/`

Final Version as of April 15, 2013.

DECLARATION

Dr. José María Saiz Vega, Profesor Titular de la Universidad de Cantabria y Dr. Fernando Moreno Gracia, Catedrático de Óptica de la Universidad de Cantabria, certifican:

Que la presente Memoria, titulada "Sistemas nanoestructurados con propiedades eléctricas y magnéticas arbitrarias: Desarrollo y Aplicación de una Extensión de la Aproximación de Dipolo Discreto (E-DDA)", ha sido realizada, bajo nuestra dirección, por Rodrigo Alcaraz de la Osa, y constituye su Tesis para optar al grado de Doctor por la Universidad de Cantabria. Asimismo emitimos nuestra conformidad para que dicha memoria sea presentada y tenga lugar, posteriormente, la correspondiente lectura.

Santander, Abril 2013

Fdo.: Dr. José María Saiz Vega

Fdo.: Dr. Fernando Moreno Gracia